学位論文

Distribution behaviors of molybdenum and tungsten in marine sediment-water system under various redox conditions

（異なる酸化還元環境におけるモリブデンとタングステン
の海洋堆積物への分配挙動）

平成 28 年 12 月博士（理学）申請

東京大学大学院理学系研究科
地球惑星科学専攻
渡辺　勇輔

Abstract

Molybdenum (Mo) and tungsten (W) belong to the same group in the periodic table and possess similar chemical properties. In the modern oxic seawater, aqueous species of the two elements are the same, tetrahedral oxyanions for both elements (MoO_4^{2-} and WO_4^{2-}). The molar ratio of dissolved Mo and W (Mo/W) in modern seawater is 1800, whereas the ratio in crustal rock is only 3, which shows that solubility of Mo in the oxic ocean is much higher than that of W. The difference in the water solubilities of Mo and W can be explained by their distributions between seawater and ferromanganese oxides under the oxic condition.

Under anoxic or euxinic condition, on the other hand, organic carbon and sulfide minerals, such as pyrite (FeS_2), should be considered in understanding the geochemical behaviors of Mo and W. Therefore, the water solubilities of Mo and W in euxinic ocean can differ from those in oxic ocean. However, the factors controlling their behaviors in palaeocean are not well known, because few studies have been conducted about speciation of Mo and in particular for W in anoxic and euxinic sediments.

In Chapter II in this thesis, geochemistry of Mo and W in sediment–porewater system were investigated using a core sample collected in sediment with hydrothermal minerals (Izena Hole, Okinawa, Japan). Molybdenum contents in the sediment and the porewater were quantified to calculate the partition coefficient K_d (concentration ratio of the solid phase to the aqueous phase). However, W concentration in the porewater was too low to be detected. Thus, we also conducted laboratory experiments simulating the sediment–porewater system to clarify the partition behaviors of Mo and W under redox conditions. X-ray absorption fine structure (XAFS) spectra were obtained to determine the chemical species of Mo and W in sediment at

different depths to understand the chemical processes of Mo and W. In particular, high-sensitive XAFS spectroscopy in wavelength-dispersive fluorescence mode was applied to measurements of W L_3 edge X-ray absorption near edge structure (XANES) spectra to reduce the interference signals from coexistent elements (Zn and Ni), thereby facilitating the identification of oxygen and sulfur-coordinated species for W in the sediments.

The collected core sample covered a broad range of redox conditions having various concentrations of hydrogen sulfide (H_2S) depending on the depth. Iron oxides in the upper layer suggested the formation of oxic condition above 4 cm depth below the seafloor (cmbsf). Iron and Zn sulfide minerals were found in the deeper layer (16–24 cmbsf), indicating that reducing condition was formed in that layer. Hydrogen sulfide was also observed in the porewater in the deeper layer. Analyses for Mo revealed that K_d of Mo was larger in the deeper layer with high contents of pyrite and H_2S, indicating that Mo enrichment occurred under reducing and/or sulfidic conditions. In addition, chemical species of Mo was oxygen-coordinated species in the upper layer (0–8 cmbsf). Meanwhile, Mo sulfide species were detected in the deeper layer, which suggested that the sulfidation of Mo is an important reaction for Mo enrichment in the sediments.

On the other hand, the solid-water distribution of W between sediment and water was not dependent on the sediment depth. Oxygen-coordinated species were observed at any depths studied here where the H_2S concentration ([H_2S]) was below 20 μM. This result suggests that the Mo/W ratio in the sediments increases depending on the progress of the reducing condition, and vice versa in the coexistent porewater. Speciation analysis revealed that the high stability of oxygen-coordinated species of W, rather than that of Mo, was responsible for the variations of the Mo/W ratio under various redox conditions.

In Chapter III, I also determined chemical species of Mo and W in Early Cambrian black shale where highly sulfidic condition was presumably formed. Early Cambrian black shale widely distributed in the Yangtze Platform in South China was studied here. Mineralogical information was examined by observation with optical microscope and major element compositions. Chemical species of Mo and W were determined by XAFS. For highly-sensitive measurement of W, Bent Crystal Laue Analyzer (BCLA) were introduced to apply wavelength-dispersive mode to the fluorescence X-ray detection.

Concentration of Mo in the black shale was high (>60000 ppm), and its main chemical species was mainly Mo(IV)S_2. Linear combination fitting of obtained spectra indicated the presence of Mo adsorbed on pyrite, which suggests that Mo was adsorbed on sulfide minerals such as pyrite and subsequently transformed to reduced Mo(IV)-S species. On the other hand, concentration of W in the black shale was much lower (30 ppm). Here, the introduction of BCLA successfully reduced interference X-rays of scattered X-rays, and Ni Kβ and Zn Kα fluorescence X-ray, which finally allowed us to measure W L_3 edge XAFS spectra. The spectra showed that W formed both sulfur-coordinated and oxygen-coordinated species in euxinic sediment. These species were formed by different distribution mechanisms such as (i) adsorption to sulfide minerals as sulfur-coordinated species, and (ii) coprecipitation of WS_4^{2-} into carbonates as oxygen-coordinated species.

The presence of carbonate mineral in the sediment makes it possible to estimate the dissolved concentrations of W and Mo at the time of the deposition. In this study, we measured the signal intensity of Mo and W at the carbonate phase to estimate the Mo/W ratio in the palaeocean. The result showed that the molar Mo/W ratio in sulfidic palaeocean was about 1, which was very different from that of Mo/W in modern oxic seawater (=1800). This estimation

supports the partition behavior of Mo and W under sulfidic condition: Mo should be mostly removed from sulfidic seawater, while W would not adsorb to sediment greatly compared with Mo.

Our approach with molecular scale investigation of Mo and W species to clarify the partition behavior of these elements under sulfidic condition will lead to more accurate understanding of the processes. In particular, speciation results of W in natural samples cannot be obtained without using the high sensitive XAFS analysis developed in this study. I believe that the present study can be a basis to clarify the enrichment process and possibly isotope fractionation of Mo and W in their solid-water partitions in ocean.

要旨

　モリブデン(Mo)とタングステン(W)は同族元素であり、現在の海水中では主にオキソアニオン(MoO_4^{2-}、WO_4^{2-})として存在するなど、化学的性質が類似した元素である。これらの元素は地殻中での存在度がほぼ等しい一方で、海洋における溶存モル濃度は Mo の方が 1800 倍高い (Sohrin et al., 1987)。これは鉄マンガン酸化物への吸着メカニズムの違いが大きな要因であると考えられている(Kashiwabara et al., 2011; 2013)。

　一方、酸素が存在せず現在より還元的な環境であった海洋では、硫化物などの還元的な堆積物との相互作用が固液分配において重要な役割を持つと考えられ、酸化的な海洋とは固液分配挙動が大きく異なると考えられる(Erickson and Helz, 2000; Mohajerin et al., 2014)。

　本研究では X 線吸収微細構造(XAFS)解析を用いた Mo と W の還元的な堆積物中での化学状態解析に基づいて還元的な環境での Mo と W の分配挙動の解明を行い、これらの元素の溶解性が酸化的環境とはどのように異なるのかを調べた。

[熱水噴出物起源堆積物における Mo と W の分配挙動]

　中部沖縄トラフに位置する伊是名海穴で採取された熱水噴出物が堆積した堆積物コア試料(全長 24 cm)の化学分析及び室内実験を実施し、水―堆積物系の酸化還元状態が Mo と W の分配挙動に与える影響について調べた。コア試料は 4 cm 毎に分割し、各深さの間隙水及び堆積物中の Mo の濃度を ICP-MS を用いて定量し、分配係数 K_d(=[固相中濃度]/[液相中濃度])を算出した。堆積物中の Mo、W、Fe、S の XAFS 解析から堆積物中の各元素の化学種を決定した。また堆積物試料を嫌気チャンバー内で乾燥させ、Mo と W の吸着実験を行い分配挙動を比較した。

　堆積物及び間隙水は深層ほど還元的な環境となっており、上層の試料では酸化物が多く含まれていたのに対し、下層試料では間隙水中に硫化水素 (H_2S)が含まれていた。試料中の Mo 濃度から求めた K_d は H_2S 濃度及び Mo 硫化物化学種の割合の増加に伴って大きくなっており、還元的環境が Mo の固相への分配を促進することが確認された。W の堆積物中での化学形は深さによって変わらず、酸素配位化学種のままであった。

　一方、吸着実験による K_d の比較の結果、堆積物の連続的な酸化還元状態の変化に応じて、Mo と W の相対的な分配挙動が変化し、還元的な環境では Mo の固相への分配がより大きくなることが示された(図 1)。この結果は還元的な海洋では Mo と W の溶解性が現在とは異なることを示唆する。

[初期カンブリア紀黒色頁岩中の Mo と W の化学状態分析]

　中国南部 Niutitang 層の揚子江上流に幅広く分布する初期カンブリア紀（約 5 億 4 千万年前）の貧酸素環境時に堆積したと考えられる黒色頁岩中の Mo と W の化学状態を調べ、H_2S 濃度が高く非常に還元的な環境における Mo と W の分配挙動を調べた。薄片試料を作成し、マイクロ-XRF-XAFS 法を用いて Mo と W の試料中での濃集相と化学状態を調べた（図 2）。本試料は鉄、亜鉛、ニッケル等の硫化鉱物を高濃度に含んでおり、通常の蛍光 XAFS 測定では W Lα 線(8.398 keV)の検出に対して Ni Kβ(8.265 keV)や Zn Kα 線(8.632 keV)が干渉し、良質なスペクトルが得られない。そこで本研究では、蛍光 X 線測定に用いる半導体検出器の前にラウエ型分光結晶(BCLA)を導入し、干渉する X 線を低減させて測定した（蛍光分光 μ-XRF-XAFS 法（世界初））。

　Mo は試料中で硫化に高濃度に濃集しており(>60000 ppm)、複数の鉱物相においてモリブデナイト(MoS_2)と類似したスペクトルが得られた。黒色頁岩中では硫化鉱物への吸着による濃集、その後のモリブデナイトへの変質が起きたことが示唆された（図 2）。

W の試料中での濃度は、Ni や Zn と比較すると 1000 分の 1 程度(約 30 ppm)であったが、BCLA を用いたエネルギー差マッピングを行うことで W の分布と W L3 端 XAFS スペクトルを得ることができた（図 2）。W は硫黄配位と酸素配位の 2 種類の形態で存在していることがわかった。硫黄配位で存在している相は Mo の濃集と相関しており硫化鉱物への吸着によって濃集したと考えられる。一方、酸素配位化学種として存在している相は炭酸塩鉱物が含まれており、還元的な環境において炭酸塩への取り込みが起きていることが示唆された。このような H_2S が非常に高い環境において W の溶存化学種である WS_4^{2-} が異なる鉱物相へ取り込まれる際の挙動の違いが室内実験から示された。

　炭酸塩相と硫化物相に含まれる Mo と W の存在度から推定した本試料における Mo と W の固液分配は、H_2S 濃度が比較的低かった沖縄堆積物試料よりも、Mo の固相への分配が大きいことが示唆された。

[酸化還元状態の指標としての炭酸塩中の Mo/W 比]

　上記の成果に基づくと、海水中の Mo/W 比は、酸化的な環境から還元的な環境になるにつれて、大きく減少することが示唆された。Mo と W は、炭酸イオンを置換して炭酸塩に取り込まれ、その比は海水中の Mo/W 比を反映すると期待されるため、Mo/W 比は古酸化還元状態の指標として有効となる可能性がある。

[まとめと今後の展望]

　Mo は還元的な環境で堆積物への濃集が数多く報告されており、酸化還元状態の指標としてしばしば利用されてきたが、W に関する知見は少なく、ここ数年でいくつかの研究が報告され始まっている。そのような中で本研究は、天然試料中の Mo と W の化学種を調べた上で、固液分配挙動を分子地球化学的に理解することに成功している。こうしたアプローチは、異なる酸化還元環境や H_2S 濃度における Mo と W の水溶解性と生体必須元素の関係、古酸化還元状態の推定への Mo と W の利用、Mo と W の同位体地球化学、レアメタルとしての Mo や W の濃集現象などの発展に大きく貢献すると期待される。今後さらに同族である Mo と W の固液分配挙動の違いを分子軌道の安定性から理解することで、これらの元素の地球化学のより本質的な理解を進め、様々な環境での Mo と W の地球化学的ふるまいを理解することに貢献したい。

CONTENTS

Abstract

CONTENTS

Chapter I.   GENERAL INTRODUCTION

I.1. Evaluation of Earth's environment and chemical composition of ocean based on reactivities of trace elements

Atmospheric and oceanic environments have been changing during the evolution of the earth, more typically reflected in the increase of atmospheric oxygen. The evidence of early life is found in Isua sediments in Greenland formed at 3.8 Ga. These early lives were considered as anaerobic organisms which did not need oxygen for their metabolisms (Rosing et al., 1999). The oldest cyanobacteria were found in 3.6 Ga Australian sedimentary rocks (Schopf, 1993), and Earth's oxygenation has continued after the period. Numerous studies about the increasing rate of atmospheric oxygen through the earth's history has been conducted by isotopic and lithological approaches (Holland, 2006; Scott et al., 2008). Through the oxygenation of earth's environment, oxidation-reduction (redox) condition has been changed in the aqueous environment such as in paleocean. Chemical composition of the ocean should be affected strongly by the redox condition, which causes variation of oxidation states and dissolved species of various elements that finally control their geochemical behaviors (Saito et al., 2003). Thus, concentrations of various elements in anoxic and/or sulfidic ocean are different from those in oxic ocean. Williams and da Silva (2003) estimated chemical compositions of various elements in sulfidic ocean and compared them with those in oxic ocean (Fig. I-1), suggesting that concentrations of some bioessential elements such as cupper (Cu) and zinc (Zn) were considered to be very low in sulfidic ocean. Therefore, it is possible that these elements were not available to the primitive organisms. These estimations indicate that bioavailabilities of

1

elements have been changing with the variation of redox condition, which in turn controlled solubilities of various elements.

The change of concentration of bioavailable elements with redox condition is very complex. For the trace elements such as molybdenum (Mo) and tungsten (W) which are potential bioavailable elements, it is important to clarify their geochemical behavior under various redox condition to understand their bioavailabilities (Anbar, 2008).
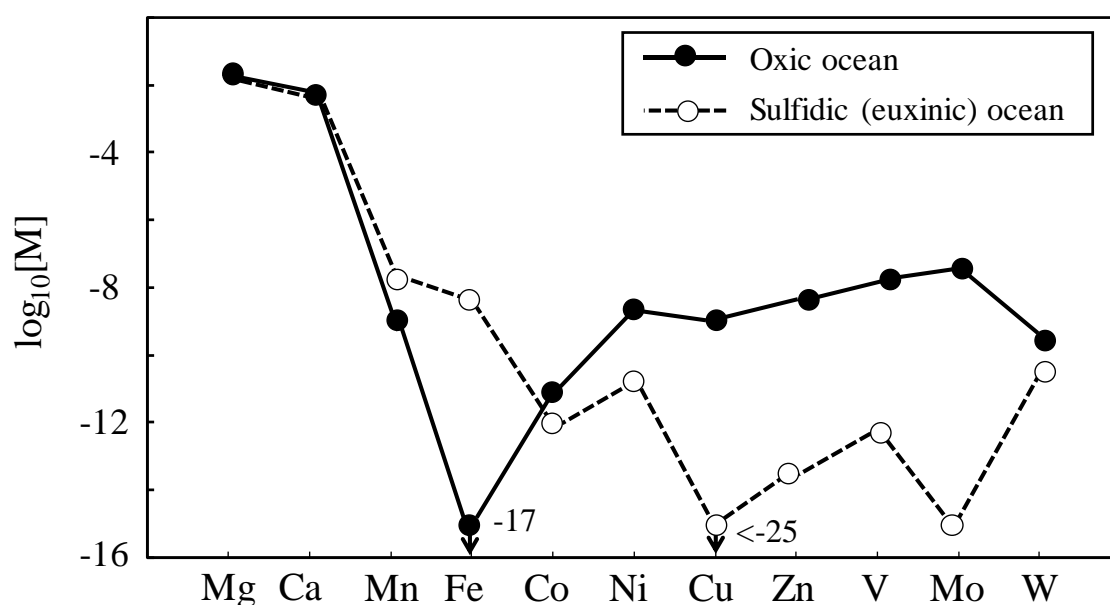

Fig. I-1 Comparison of concentration of elements in euxinic ocean with that in oxic ocean (Williams and da Silva, 2003).

I.2. Geochemistry of Mo and W

Molybdenum (Mo) and tungsten (W) belong to the same group in the periodic table and possess similar chemical properties. The changes of their concentrations in the ocean under various redox conditions are very complex. For trace elements such as Mo and W, the sediment–seawater partition behavior is a key factor in understanding their geochemical behaviors such as their solubilities in seawater, because their concentrations in seawater are very low to form their own minerals such as molybdenite (MoS_2) and scheelite ($CaWO_4$). Their geochemical behaviors are considered to be redox-sensitive and are strongly dependent on the redox and sulfide concentrations in the oceanic environment. In the modern oxic seawater, aqueous species of the two elements are the same, tetrahedral oxyanions for both elements (MoO_4^{2-} and WO_4^{2-}; Turner et al., 1981). Oxyanions have generally long residence times, and their concentrations display conservative depth profiles in the water column (Sohrin et al., 1987; 1999). The oxyanions have some stable chemical species dependent on pH and Eh conditions. Figure I-2 shows Eh-pH diagrams of Mo and W. In the diagrams, both Mo and W form sulfide minerals such as MoS_2 and WS_2 under low Eh condition.
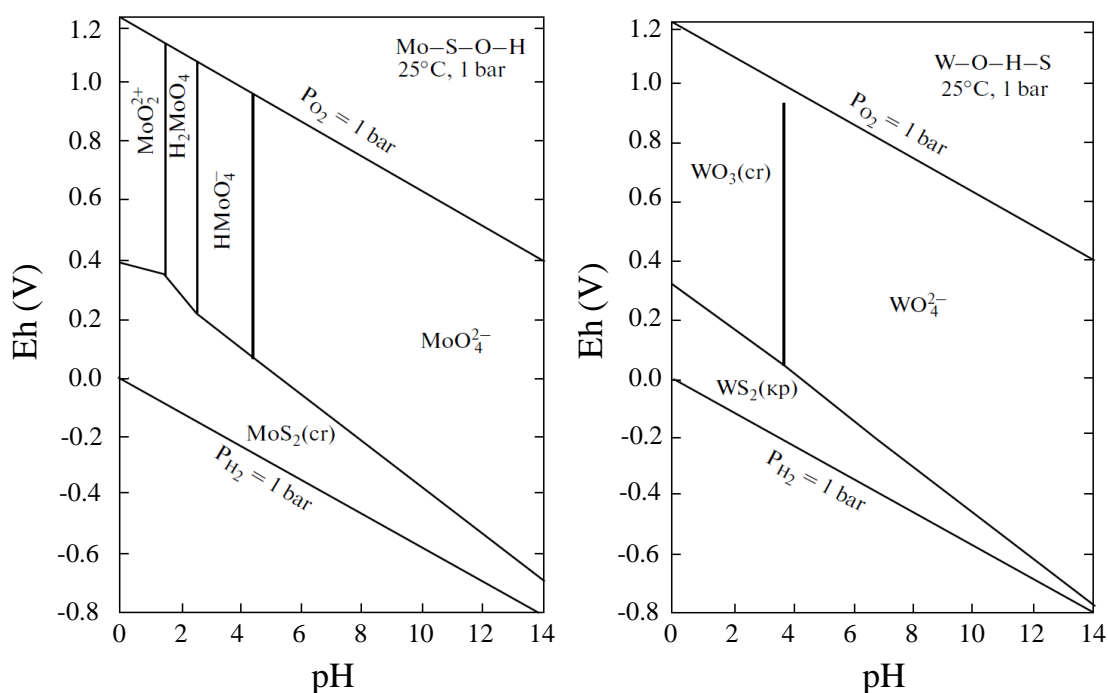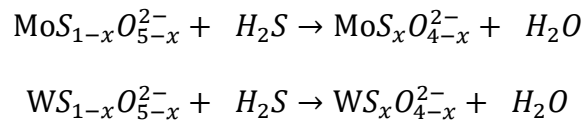
Fig. I-2 Eh-pH diagrams of Mo and W in the presence of 10^{-3} M of H_2S. Thermodynamic data was applied in Ryzhenko, 2010.

Although Mo and W show similar chemical properties, the concentrations of Mo and W in seawater are 106 nM and 60 pM, respectively (Sohrin et al., 1987). The molar ratio of the dissolved Mo and W (Mo/W) in seawater is 1800, whereas that in crustal rock is only 3 (Bowen, 1979; Sohrin et al., 1987), which shows that solubility of Mo in the oxic ocean is much higher than that of W. The difference in the water solubilities of Mo and W can be explained by the interaction between seawater and ferromanganese oxides (Kashiwabara et al., 2011; 2013). However, under anoxic or euxinic conditions, organic carbon and sulfide minerals, such as pyrite (FeS_2), should be considered in understanding the geochemical behaviors of Mo and W. Molybdenum is regarded as an effective paleo-redox tracer because of its contrasting geochemical behaviors between oxic and euxinic environments (Helz et al., 1996; Adelson et al., 2001; Dahl et al., 2013; Takahashi et al., 2014). Under sulfidic conditions, Mo forms

thiomolybdate species ($MoO_nS_{4-n}^{2-}$) which strongly interacts with organic matters and sulfide particles (Brucker et al., 2009). Several burial processes of Mo to euxinic sediments have been proposed, such as coprecipitation with Fe to form $Fe_5Mo_3S_{14}$, reduction to Mo(V), and interactions with dissolved organic matters and polysulfides. However, the chemical processes controlling the behaviors in natural euxinic environments remain unclear (Chappaz et al., 2014).

Similar to Mo, thiotungstate species ($WO_nS_{4-n}^{2-}$) can form in the presence of sulfide. However, their formation constants reveal that the complete transformation from WO_4^{2-} to WS_4^{2-} occurs only at high sulfide concentrations in the aqueous phase, unlike the case for Mo (Erickson and Helz, 2000; Mohajerin et al., 2014).

The sulfidation reactions of MoO_4^{2-} and WO_4^{2-} to $MoO_nS_{4-n}^{2-}$ and $WO_nS_{4-n}^{2-}$, respectively, are as follows:

$$MoS_{1-x}O_{5-x}^{2-} + H_2S \rightarrow MoS_xO_{4-x}^{2-} + H_2O$$

$$WS_{1-x}O_{5-x}^{2-} + H_2S \rightarrow WS_xO_{4-x}^{2-} + H_2O$$

In the equations, x ranges from 1 to 4. Equilibrium constants between each species can be written as:

$$K_x = \frac{MoS_xO_{4-x}^{2-}}{[MoS_{1-x}O_{5-x}^{2-}][H_2S]}$$

$$K_x = \frac{WS_xO_{4-x}^{2-}}{[WS_{1-x}O_{5-x}^{2-}][H_2S]}$$

The calculated K values were summarized in Table I-1. From these values, dominant dissolved species of Mo change from MoO_4^{2-} to MoS_4^{2-} when [H_2S] increases over 11 μM (Erickson and Helz, 2000). This threshold is called as "geochemical action point switch (APS)". On the other hand, dominant W species becomes WS_4^{2-} only at [H_2S] > 100 μM (Mohajerin et al., 2014),

indicating that Mo is much more reactive with H_2S which readily form MoS_4^{2-} in the aqueous phase (Table I-1).

Table I-1 Equilibrium constants of sulfidation reaction of Mo and W anions. The constants were reported in a) Erickson and Helz, 2000, and b) Mohajerin et al., 2014, respectively.

Reaction	X	Mo log K,[a]	W log K,[b]
$MO_4^{2-} \rightarrow MSO_3^{2-}$	0	5.19±0.03	3.08±0.11
$MSO_3^{2-} \rightarrow MS_2O_2^{2-}$	1	4.80±0.12	3.22±0.22
$MS_2O_2^{2-} \rightarrow MS_3O^{2-}$	2	5.00±0.13	2.76±0.10
$MS_3O^{2-} \rightarrow MS_4^{2-}$	3	4.88±0.28	<2.36 (extrapolated)

In addition, the positive correlation between dissolved W and H_2S concentrations indicates that formation of WS_4^{2-} leads to an increased solubility of W. This phenomenon is directly opposite to that for Mo, that is Mo becomes less soluble by the formation of MoS_4^{2-} (Fig. I-3; Mohajerin et al., 2014; 2016). These results suggest that the water solubilities of Mo and W in euxinic ocean can differ from those in oxic ocean.
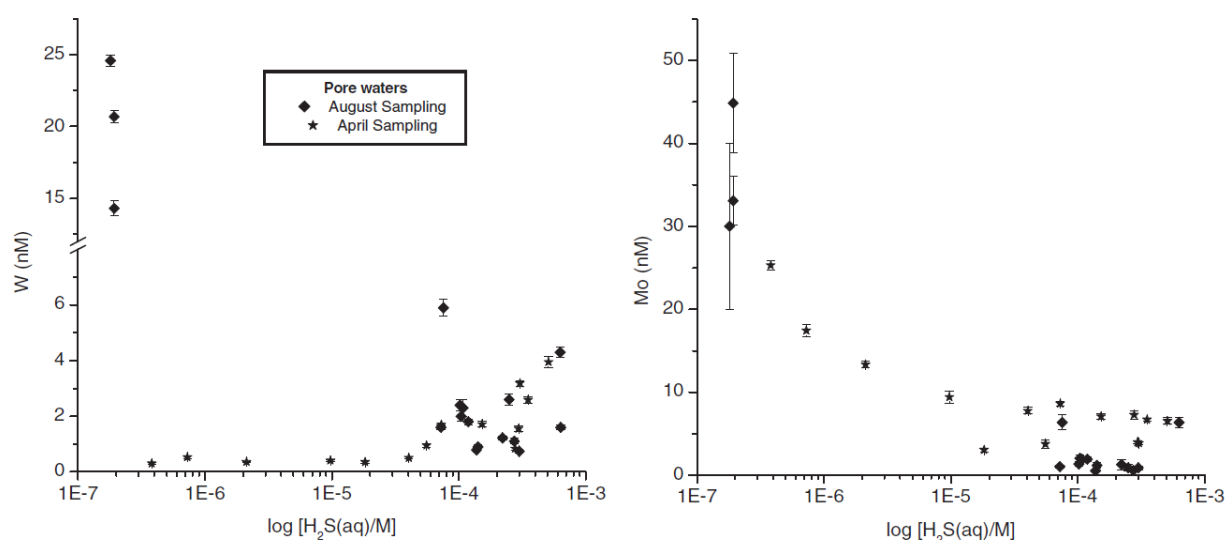

Fig. I-3 Dissolved W and Mo concentration vs. H_2S(aq) in sediment pore waters of Terrebonne Bay (Mohajerin et al., 2016).

I.3. Application of X-ray absorption fine structure analysis for the molecular scale understanding of trace elements in the environmental samples

Speciation of elements in environmental samples gives us the information about geochemical process of the elements in the environment (Turner, 1995). Solid/water interaction such as adsorption behavior of the elements is the key process controlling the geochemistry of the elements. Chemical species of elements preserved in sediment and rocks show the adsorption mechanisms of elements under the depositing condition. From these information, we can understand the geochemical behaviors including solubility and isotope fractionation of various elements under various redox conditions.

X-ray absorption fine structure (XAFS) is one of the useful tools for the speciation of elements in environmental samples. XAFS is variation of normalized absorption coefficient of X-ray around X-ray absorption edge of a target element in the sample. X-ray absorption spectra show chemical species of the target element with high selectivity to the element. In addition, XAFS analysis is a non-destructive analysis with high sensitivity when using synchrotron radiation (SR) as X-ray source. Based on these reasons, XAFS analysis has been for the purpose of speciation of trace elements in natural samples. The use of SR allowed us to obtain over 10^4 times stronger brightness of X-ray compared with laboratory X-ray source. Consequently, XAFS analysis has been frequently employed in the field of local structure analysis of various elements in 1970s (Ohta, 2007).

The first SR facility in Japan was built in 1950s, but with only 170 MeV acceleration energy. After that, SR technology has been developed based on the use of storage ring and development of light source. Currently, SPring-8, a third generation SR facility has 8.0 GeV of acceleration energy, so that we can obtain intense X-ray at high energy region over 100 keV.

7

The development of detectors for X-ray is also important for XAFS analysis for natural samples. Generally, XAFS is measured in transmission mode using ionization chambers monitoring the incident (I_0) and transmitted (I) X-rays measured in front of and behind the samples. The transmission mode needs high concentration of the target element in the sample sufficient to absorb incident X-ray to some degree. The absorption coefficient μt is defined as $\mu t = \ln(I_0/I)$. As for the analysis of trace elements at 10-100 ppm order in the samples, solid state detector (SSD) is often used to measure XAFS spectra, which measures fluorescence X-ray (XRF) intensity (I_F) from the target element. In this case, μt is defined as $\mu t = I_F/ I_0$ when we can ignore the variation of penetration depth of incident X-ray in the energy range of the spectra. By combining the high brightness X-ray source and high sensitivity detector such as SSD, various molecular scale mechanisms related to their chemical processes in environment can be obtained for the trace elements using XAFS analysis (Manceau et al., 2002).

In this thesis, we applied advanced XAFS measurement having high energy resolution, or high selectivity of the target element in the sample. However, even employing the fluorescence mode, which is generally a high sensitive method, there are some problems for the XAFS measurement of trace elements caused by the interferences of fluorescence X-rays from other major elements contained in the sample. In Chapters II and III in this thesis, I employed wavelength-dispersive (WD) technique using bent crystal Laue analyzer (BCLA) for the speciation analysis of W in natural sediment samples (Kropf et al., 2003; Kashiwabara et al., 2009). The bent crystal can eliminate the interferences of X-ray from major elements in the samples and scattered X-ray from the samples by the diffraction using the bent crystal (Fig. I-4). For this purpose, I placed the BCLA in front of SSD for the W L_3 edge XAFS measurement in BL37XU at SPring-8. In addition, focused beam (0.8×0.8 μm^2) made by a Kirkpatrick-Baez

(K-B) mirror system was applied to acquisition of micro scale XRF images of trace elements in the sample (Fig. I-5). By combining the WD-XAFS technique and micro scale XRF imaging, I for the first time succeeded in obtaining the W species in local area in natural sediments formed under euxinic condition ocean in Chapter III.
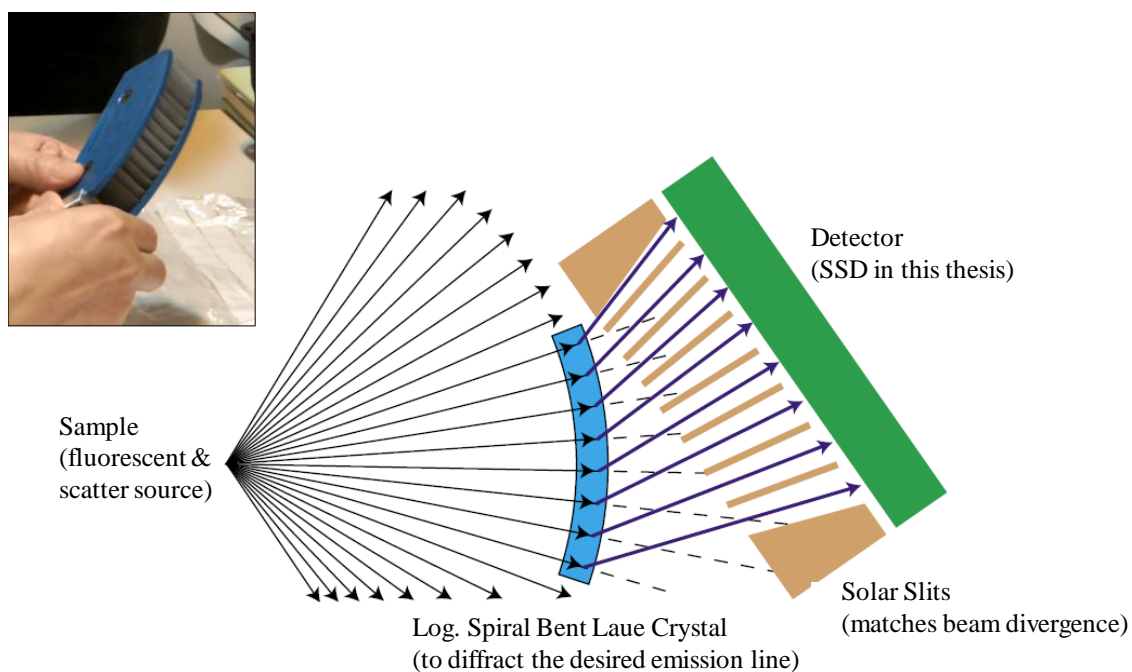
Detector
(SSD in this thesis)

Sample
(fluorescent &
scatter source)

Solar Slits
(matches beam divergence)

Log. Spiral Bent Laue Crystal
(to diffract the desired emission line)

Fig. I-4 A structural image and photograph of bent crystal Laue analyzer (BCLA; DCA-0950, Oxford Danfysik).

In-vacumm undulator

XY slit

Si 111 monochromator

XY slit

K-B optics

Sampl

23 m

57 m

Si (Li)
SSD
10 deg

BCLA
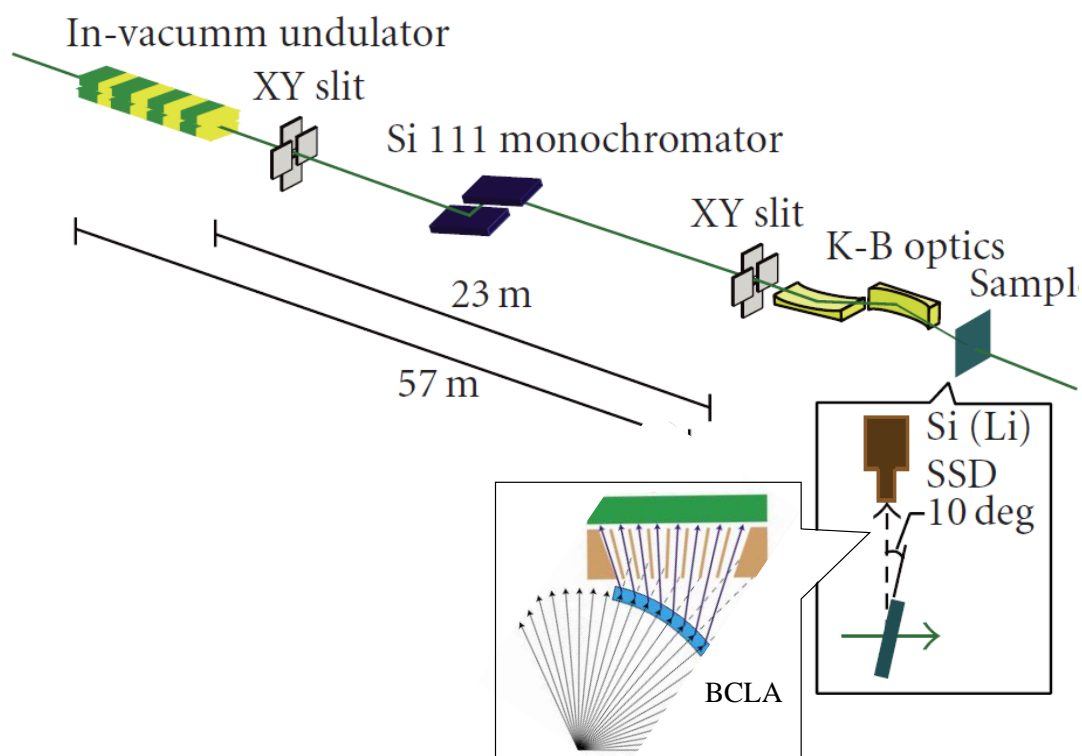
Fig. I-5 Experimental set up of µ-XRF-WD-XAFS technique in BL37XU at SPring-8 performed in Chapter III.

I.4. Purpose of this study

Previous studies suggested that the key mechanism of change of geochemical behavior and water solubility of Mo and W is the formation of thioanions such $MoO_nS_{4-n}^{2-}$ and $WO_nS_{4-n}^{2-}$ in the presence of H_2S. The degree of formation of thioanions depends on the concentration of H_2S (Erickson and Helz, 2000; Mohajerin et al., 2014). Molybdenum prefers to form thiomolybdate in water under lower sulfidic condition than that of W. Geochemical action point switch (APS), which was defined as the minimum concentration of H_2S to form MoS_4^{2-} in natural water, was estimated as $[H_2S] = 11$ μM from the equilibrium constants of Mo species. In the case of W, on the other hand, APS was estimated over 100 μM due to the lower formation constant of thiotungstate. The formation of thioanions of Mo and W was examined in experimental and theoretical approaches. However, there are few studies about the aquatic geochemical behaviors of the two elements based on the analysis of natural samples, in particular for W.

In this study, the geochemical behavior, or in particular partition behavior, were examined for Mo and W under different redox conditions and H_2S concentrations using their concentration and speciation analyses for natural samples. To understand the relationship between chemical species of Mo and W and their geochemical behaviors, we chose various natural sediment and sedimentary rocks which were formed under various redox conditions. At first, I showed the results of chemical and speciation analyses of hydrothermal sediment and its porewater deposited in Okinawa Trough in Chapter II. The sediment core sample exhibited gradual change of redox condition from upper to lower layer. In the Chapter II, I found the change of partition behaviors of Mo and W according to redox condition and the concentration of H_2S, which revealed different water-solid distribution behaviors between Mo and W. This

11

result would be related to the relatively lower concentration of H_2S to form thioanions in which Mo could form MoS_4^{2-} while W could not form WS_4^{2-}.

In Chapter III, we performed micro-scale speciation analysis of Mo and W in Early Cambrian black shale which deposited under highly sulfidic condition sufficient to form WS_4^{2-}. In the sample, the concentration of W in the sample was very low with high abundances of Ni and Zn which potentially prevent measurement of XRF of W for the XAFS analysis. To obtain speciation data of W in the sample, WD technique with X-ray microbeam was applied using BCLA for XAFS analysis. The advanced XAFS analysis with high sensitivity allowed us to understand the geochemical behavior of trace level of W in sulfidic sedimentary rocks. In addition, we compared the speciation data of W with Mo to understand the difference of their solid-water distributions under highly sulfidic condition.

From these chemical analyses, we could understand the difference of geochemical behaviors of Mo and W under sulfidic condition which have been unknown because of lack of speciation data for natural samples. This study revealed that the new speciation technique for trace elements in natural samples using XAFS analysis combined with WD method is effective for the elements whose concentrations are less than 10 ppm in sedimentary rocks.

In summary, a schematic that illustrates the sulfide concentration ranges assumed in each chapter was shown in Fig. I-6. The sulfidic condition in the modern hydrothermal system described in Chapter II ranges from $[H_2S]$ = 0.0 to 20 μM, while that in the Cambrian black shales in Chapter III was presumably higher than that in the modern sediments. It is expected that systematic difference of the concentration of H_2S in the aqueous phase can cause different solid-water distributions of Mo and W in the two systems.
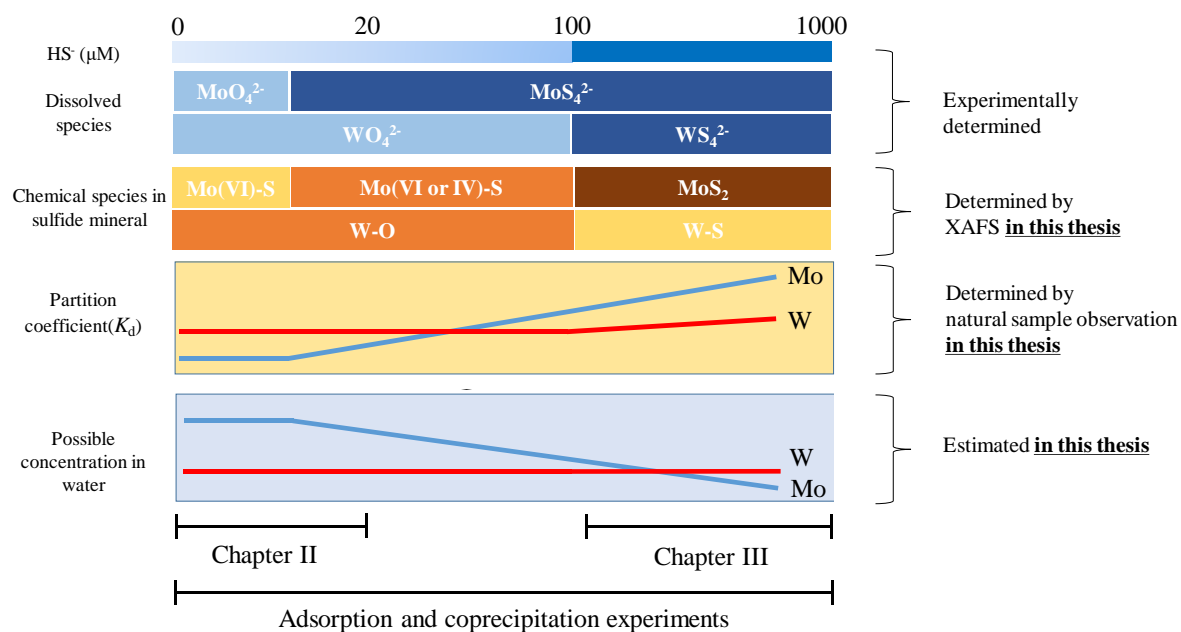
Fig. I-6 Possible changes of geochemical behaviors of Mo and W under various sulfidic condition assumed in this thesis.

Chapter II.   DIFFERENT PARTITION BEHAVIOR OF MOLYBDENUM AND TUNGSTEN IN A SEDIMENT-WATER SYSTEM UNDER VARIOUS REDOX CONDITIONS

II.1. Introduction

To understand the solubilities of Mo and W under sulfidic conditions and to compare with those under oxic condition, I studied the sediment–porewater partition behaviors of Mo and W deposited near hydrothermal environments which includes hydrothermal derived materials such as sulfide and sulfate minerals. In addition, the sediment showed various redox conditions depending on the depth. The variation of redox condition would be formed by recharging of ambient seawater and early diagenesis in burial environment. Using the sediment core sample, I performed various chemical analyses including both quantitative and speciation analyses, by which I determined natural partition behavior of Mo between sediment and porewater.

In the laboratory experiments, the addition of W into the sediment–porewater system was necessary to obtain the partition data of W. Nonetheless, the results seem reasonable because Mo was also added into the system, and the results coincided with the Mo data obtained in a natural system.

Speciation analyses were conducted on trace level Mo and W in natural sediments by XAFS analysis, particularly X-ray absorption near edge structure (XANES), to clarify the partition mechanisms of Mo and W. Although the XAFS analysis is a powerful tool for understanding

the chemical species of trace elements in natural samples, the fluorescence XAFS analysis of W using the W Lα line in natural sediments presents analytical problems caused by the interferences of fluorescence X-rays from other major elements in sediments, such as the Ni Kα and Zn Kβ lines. Previous studies attempted to reduce these interferences by applying the wavelength-dispersive XAFS method, which introduces a BCLA in front of the Ge-SSD (Takahashi et al., 2006; Kashiwabara et al., 2013). In the present study, wavelength-dispersive XAFS method was employed to determine the chemical species of W in natural marine sediments near the hydrothermal vent.

Basing on the partition and speciation of Mo and W under various redox conditions, I identified the chemical processes that control the partition behaviors of Mo and W in the sediment–porewater (seawater) system. These chemical processes cause the differences in their responses to the redox condition in the sediment–porewater system.

II.2. Samples and Analytical Methods

II.2.1. Sample collection and chemical analyses

Sediment and porewater samples were collected from the 1187MB core, which is located 30 m south of the Dragon Chimney in the Hakurei field (27°14.928′N, 127°4.148′E) at a water depth of 1,603 m in the Izena Hole during the NT10-17 cruise of the *R/V Natsushima* in September 2010 (Fig. II-1; Kawagucci et al., 2011; Ishibashi et al., 2014; Miyoshi et al., 2015). Hydrothermal activities were found near the sampling point. The sediment core was collected by an acrylic push corer (MBARI-type corer; Nakaseama, 2008) for short coring that was attached to a remotely operated vehicle (ROV) Hyper-Dolphin. The length of the sediment core was 24 cm showing the different color with the depth which would be caused by the variation

15

of redox condition through the depth which affects element and mineral compositions (Fig. II-2). The core sample was cut horizontally at 4 cm intervals. Each layer was sealed in an airtight polyethylene bag purged with N_2 gas and stored at 4 °C to avoid chemical oxidation of the sediments. Prior to the sealing, each sediment was pressed with a clamp to extract the porewater. The extracted porewater samples were filtered through a 0.45 μm membrane filter (Advantech, polycarbonate). These porewaters were separated for on-board and on-shore analyses, respectively. Immediately following the porewater extraction, pH, hydrogen sulfide (H_2S) concentrations, and alkalinity were measured by a pH meter (glass electrode, Horiba, Kyoto, Japan), methylene blue colorimetric analysis (Cline, 1969), and pH titration by 0.1 M HCl (Gran method; Drever, 1997), respectively as on-board analysis. Redox potential to hydrogen electrode (Eh) was measured by a Pt electrode (Fujiwara Sci., PRN-41) right after the recovery of the sediment. In the laboratory, the concentrations of sulfate (SO_4^{2-}) and magnesium (Mg) in the porewater were measured by ion chromatography (ICS1100, Thermo Scientific, USA). The porewater samples used for inductively coupled plasma mass spectrometry (ICP-MS: Agilent Technology 7700x, Tokyo, Japan) to measure the trace elements were acidified by adding 2 wt.% HNO_3 solution to prevent the incidental precipitation of various minerals.
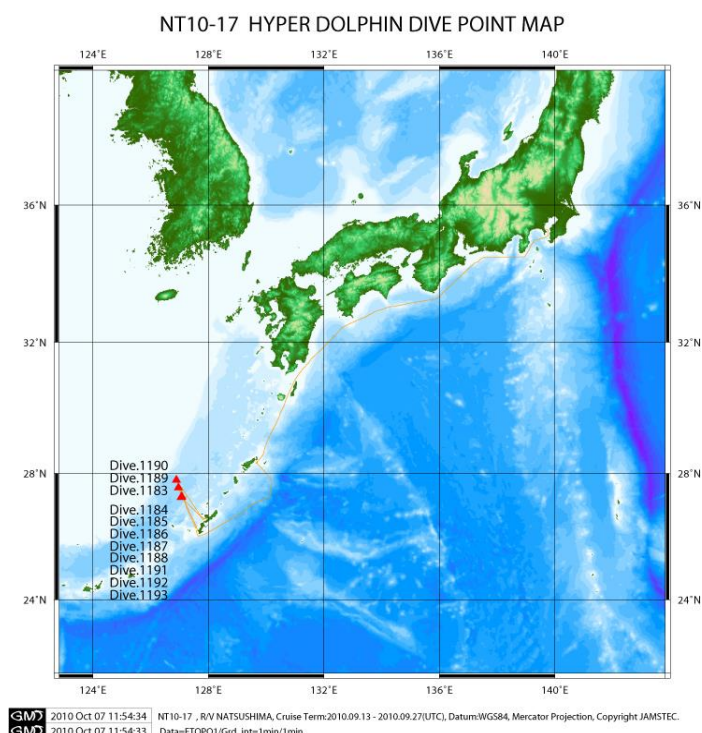
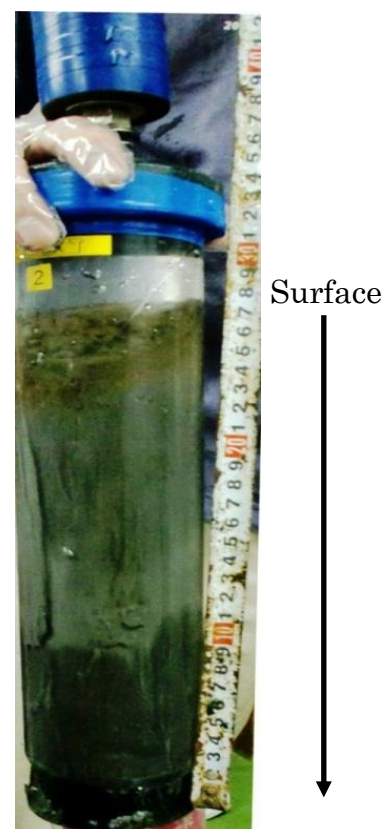Fig. II-1 A map with study areas indicated by red triangles.

Surface

Fig. II-2 A photograph of 1187MB core
collected near the Dragon chimney.

In the laboratory, packed sediments were opened in an anaerobic chamber (Ar: 95%; H_2:

5%) (Coy Laboratory Products, USA) in which the oxygen concentration was maintained below

1 ppm. The sediments were dried and homogenized with agate mortar in the anaerobic chamber.

After the homogenization, the major chemical composition of the sediments was measured by

X-ray fluorescence analysis (XRF; ZSX-101, Rigaku, Japan) using glass bead method (Kawano,

2010). Mineralogical compositions were analyzed by X-ray diffraction (XRD) measured by

Multi Flex (Rigaku, Japan). The concentrations of Mo and W in the sediments were measured

by ICP-MS after digestion by concentrated HF, $HClO_4$, and HCl solutions. The concentrations

of Mo and W in the porewater were also measured by ICP-MS. The degrees of partition of Mo

or W for the sediments at various depths were evaluated by the partition coefficient (K_d), which is defined as

$$K_d = \frac{C_s}{C_w}$$

where C_s and C_w are the molar concentrations of Mo or W in the sediment and the porewater, respectively. Total S content in the sediments was determined by barite sulfate gravimetric method (Shirakami, 1993). Approximately 1.0 mL of 5 wt.% of barium chloride dihydrate (Wako, Japan) solution was added to 5 mL of the digested sediments. The weight of the deposited barite was measured (range of measured weight: 10–30 mg). Total S content was defined by the weight of the barite precipitates.

II.2.2. XAFS measurement

Speciation of Mo and W in the sediments was performed by XAFS analyses to elucidate the partition mechanisms of Mo and W to the sediments. XANES spectra for S and Fe were also obtained to estimate the redox condition and the reactive phase in the sediments. Homogenized sediments were packed in airtight polyethylene bags with N_2 gas and stored at 4 °C prior to XANES measurements. Molybdenum K edge and W L_3 edge XANES and extended XAFS (EXAFS) spectra were obtained at BL01B1 and BL37XU in the SPring-8 (Hyogo, Japan), whereas S and Fe K edge XANES spectra were obtained at BL9A and BL12C, respectively, in the KEK Photon Factory (PF; Tsukuba, Japan). White X-ray generated from the bending magnet was monochromatized by a double crystal monochromator with a Si(111) plane for W, Fe, and S and a Si(311) plane for Mo. The reference materials for Mo, W, and Fe were measured in transmission mode by monitoring the incident intensity (I_0) and intensity after

transmission (I) of the samples in the ionization chamber; by contrast, the reference materials for S were measured in conversion electron yield mode (Schroeder, 1996; Takahashi et al., 2009). The spectra for sediment samples for the four elements were obtained in fluorescence mode with the 19-element Ge-SSD.

The W L_3 edge XANES of natural samples was measured by wavelength-dispersive XAFS method using a BCLA (DCA-0950, Oxford Danfysik; Takahashi et al., 2006; Kashiwabara et al., 2010; 2013). The spectra were collected by detecting the W Lα line in fluorescence mode with the a four-element silicon drift detector (SDD). The BCLA was placed in front of the detector to reduce the interferences of the Ni Kβ (8.265 keV) and Zn Kα (8.632 keV) lines, as well as the scattering X-ray from the incident X-ray on the W Lα line (8.398 keV).

Radiation damage and alteration with oxidation by ambient condition were not observed during the data acquisition, because multiple scans provided identical spectra. The XANES was analyzed by using the REX2000 software (Rigaku, Tokyo, Japan). The chemical species of the elements in the samples were simulated by linear combination fitting (LCF) of the XANES spectra to the reference materials. To assess the accuracy of the XANES fitting results, the R factor, which is calculated by the sum of squares of the difference between the observed and fitted data at each point, was defined as follows:

$$R = \frac{\sum (I_s(E) - I_{cal}(E))^2}{\sum I_s(E)^2}$$

where I_s and I_{cal} are the normalized absorption spectra of the solid samples and calculated values, respectively. All fitting results were obtained when the R factor was minimal in the fitting

19

procedure. For the fitting, at most five species were selected as end-members on the basis of the principle component analysis (PCA, Beauchemin et al., 2002) results to avoid underestimation of the R values, because an increase in the number of reference materials could make the R value become too low.

For EXAFS analysis, the $x(k)$ function was extracted from each raw spectrum by a spline smoothing method. E_0 (threshold energy of photoelectron) was determined as the edge inflection point for all the samples studied. The E_0 was finally optimized during the curve fitting by the theoretical EXAFS function.

II.2.3. Micro-XRF analysis of sediments

The distribution of Mo to specific phases in the sediments was investigated using μ-XRF imaging. A thin section of each sample was prepared for this analysis. Sediments air-dried in an anaerobic chamber were embedded in a high-purity epoxy resin (Eposet, Maruto Co., Ltd., Japan), which was polished with silicon carbide and subsequently with diamond abrasives. The samples were first observed using an optical microscope. Then, an electron microprobe (EMP) (JXA-8200, JEOL, Japan) was utilized to capture backscattered electron (BSE) images and determine the quantitative elemental compositions of the samples. Micro-XRF images of Mo and Fe were acquired at BL37XU in the SPring-8. Monochromatized X-ray by a Si(111) double crystal monochromator was focused to 1.5 μm × 1.5 μm (beam size at sample position) by a Kirkpatrick-Baez (K-B) mirror system (Terada et al., 2010). A two-dimensional (2D position) analysis was conducted by measuring the XRF images by Si(Li)-SSD with X-Y axis stepping-motor-driven stage.

II.2.4. Partition experiments for Mo and W

The adsorption of Mo and W onto sediment samples and pure pyrite particle were also evaluated to compare the changes in their partition behaviors depending on the redox and mineral composition of the sediments. Each air-dried sediment (20 mg) at different depths was mixed with a 10 mL solution containing both MoO_4^{2-} and WO_4^{2-} at concentrations of 0.0, 0.10, and 1.0 μM; the mixture was shaken for 24 h by a shaking bath (CM-100, EYELA, Japan) at 25 °C. The MoO_4^{2-} and WO_4^{2-} solutions were prepared by dissolving $Na_2MoO_4 \cdot 2H_2O$ (Wako, Japan) and $Na_2WO_4 \cdot 2H_2O$ (Wako, Japan), respectively, in Milli-Q water (Millipore, >18.2 MΩ·cm). Ionic strength was adjusted to 0.70 by adding NaCl, and pH was adjusted to 8.0 by adding a HCl or NaOH solution.

Adsorption experiment onto pyrite was conducted by following the procedures described in Bostick et al. (2003) to compare the partition behaviors of Mo and W between water and sulfide mineral. XANES spectra of Mo and W adsorbed on the pyrite were also compared with those of the natural sediment samples. Pyrite was purchased from Strem Chemical (>99% purity). Pyrite grains were refined by an agate mortar. The surface of the pyrite grains was washed by 0.1 M of HCl, 0.01 M of Na_2S, and subsequently Milli-Q water to remove oxidized phases. Initial concentrations of MoO_4^{2-}, MoS_4^{2-}, WO_4^{2-}, and WS_4^{2-} in the aqueous phase were adjusted to 1, 5, 10, 50, 100, or 300 μM. Thiomolybdate ion and WS_4^{2-} were prepared by dissolving $(NH_4)_2MoS_4$ (Wako, Japan) and $(NH_4)_2WS_4$ (Wako, Japan) in Milli-Q water, respectively. Each solution was mixed with the pyrite grains at pH 7.0 in the presence of 5.0 mM of Na_2S at a solid-to-water ratio of 2.0 g/L. Ionic strength was adjusted to 0.70. In addition, ionic strength and pH dependences of the distribution in the adsorption system were conducted. Ionic strength and pH were varied at constant initial Mo and W concentrations (= 50 μM).

After shaken for 24 h, each liquid phase was collected by filtration using 0.20 μm membrane filter (mixed-cellulose membrane). The filtrates were diluted by 2 wt.% of HNO_3, and the concentrations of Mo and W were measured by ICP-MS. All the sample treatment and measurements were repeated three times to ensure the precisions of the experiments.

II.3. Results and Discussion

II.3.1. Chemical analysis and redox state of sediments

Major and some trace element compositions of the sediment samples at various depths are summarized in Table II-1 with those of upper continental crust (UCC) for reference. Sediments at all depths mainly consist of Si, Al, and Fe. In addition, I observed high concentrations of S, Cu, Zn, and Pb compared with UCC (Condie, 1993; Rudnick and Gao, 2004). The enrichment of these elements could be caused by the presence of hydrothermal precipitates containing larger amounts of sulfate and sulfide minerals. In 12-16 cmbsf sample, lower concentrations of Ba, Cu, Zn, and Pb were observed, whereas Si, Na, and K showed the highest values within the core sample studied here. This result is presumably caused by the increase of contributions of these elements in continental materials such as clay minerals and other silicates during the deposition of the layer. As a result, the chemical compositions of 12-16 cmbsf sample are more similar to those of UCC compared with other depths.

Molybdenum concentration in sediments was also high relative to UCC, which was also found for other chalcophile elements indicating that the hydrothermal-derived materials includes certain amount of Mo as sulfide. On the other hand, W concentration was low compared to UCC in 12-16 cmbsf layer, suggesting that W supplied as continental materials was higher than that from hydrothermal materials. The results of the elemental compositions

were consistent with the XRD patterns (Fig. II-3), indicating the presence of quartz, plagioclase,

illite, chlorite, and pyrite as observed in the other sites in this area (Yokoyama et al., 2015;

Miyoshi et al., 2015).

Table II-1 Major and trace element compositions of the studied sediment with those of upper continental crust (UCC) for reference.

Composition (wt%)	Sample depth (cmbsf)						UCC[d]
	0-4	4-8	8-12	12-16	16-20	20-24	
SiO_2	39.5	43.3	57.4	65.9	44.6	45.1	66.6
TiO_2	0.88	0.70	0.61	0.62	0.72	0.74	0.64
Al_2O_3	11.4	11.8	13.9	15.7	13.1	13.3	15.4
Fe_2O_3[a]	6.85	12.0	11.2	8.37	17.5	18.8	5.6
MnO	0.08	0.03	0.06	0.07	0.10	0.16	0.10
MgO	1.69	1.54	1.58	1.86	1.76	1.87	2.48
CaO	0.72	0.70	1.10	1.19	0.75	0.79	3.59
Na_2O	1.46	0.87	2.38	3.23	1.66	1.90	3.27
K_2O	2.00	2.20	2.68	3.13	2.51	2.62	2.80
P_2O_5	0.39	0.12	0.12	0.14	0.14	0.14	0.15
Ba	5.09	2.73	1.04	0.16	1.91	1.91	0.06
S[b]	4.67	7.02	4.89	3.12	6.78	7.70	0.06
Cu (mg/kg)	2270	2010	1160	180	2260	1800	28
Zn (mg/kg)	7070	13000	4640	751	5290	3660	67
Pb (mg/kg)	5150	4220	2120	466	3860	3490	17
Mo (mg/kg)[c]	11.9	49.0	21.6	5.92	23.5	15.0	1.10
W (mg/kg)[c]	0.49	0.17	0.22	0.61	0.32	0.37	1.9

a. Total iron as Fe_2O_3.
b. Measured by barite sulfate gravimetric method.
c. Measured by ICP-MS.
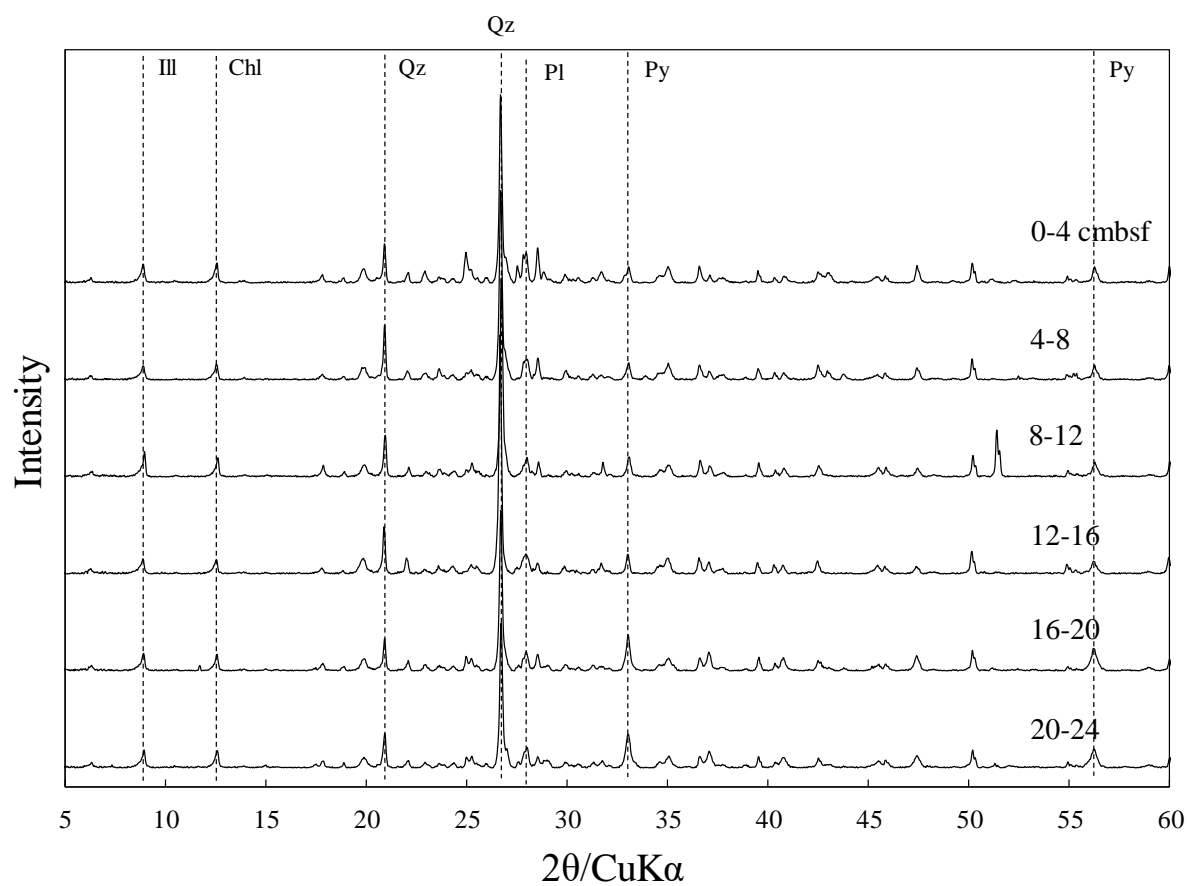d. Reported by Rudnick and Gao (2004).

Fig. II-3 XRD patterns of studied sediments. Abbreviations for minerals are as follows; Qz: quartz; Pl: plagioclase; Py: pyrite; Chl: chlorite; Ill: illite.

The 1187MB core showed redox variation with the depth below the sea floor. Figure II-4 shows the chemical composition of the porewater and the ambient seawater. In the figure, depth at 0 cmbsf means the results of ambient seawater. Although the hydrothermal fluid was expected to significantly influence the porewater chemistry particularly in deeper parts, the input of hydrothermal fluid in the 1187MB sediment core can be disregarded because of the marginal variations of Mg^{2+} and SO_4^{2-} which are essentially absent in hydrothermal fluids compared to concentrations of ambient seawater (50 mM and 28 mM, respectively) with the depth. This observation indicates that most of the ions in the porewater in the sediment were from ambient seawater, although a small amount of hydrothermal fluid could be mixed in deeper parts. The redox condition at 0–8 cm below the seafloor (cmbsf) layer was oxic, as indicated by the higher Eh value than that in the deeper sediments at 8–24 cmbsf (Fig. II-4). Although the Eh values calculated by equilibrium thermodynamics (Brookins, 1987) suggested that sulfate (SO_4^{2-}) was the primary sulfur species in the aqueous phase, H_2S was observed at 8–24 cmbsf. The simultaneous increase in H_2S with alkalinity was interpreted as the effect of the decomposition of organic matters as a result of oxidation by sulfate ions (Gamo et al., 1991).

From the chemical analyses of sediment and porewater samples, I concluded that the 1187MB sediment core sample consists of hydrothermal minerals from Dragon chimney including pyrite, pyrrhotite, sphalerite, and other sulfide minerals. After deposition at the sea floor, it is expected that oxic and reductive conditions were created in the upper and deeper layer in the sediment by diagenesis, respectively.
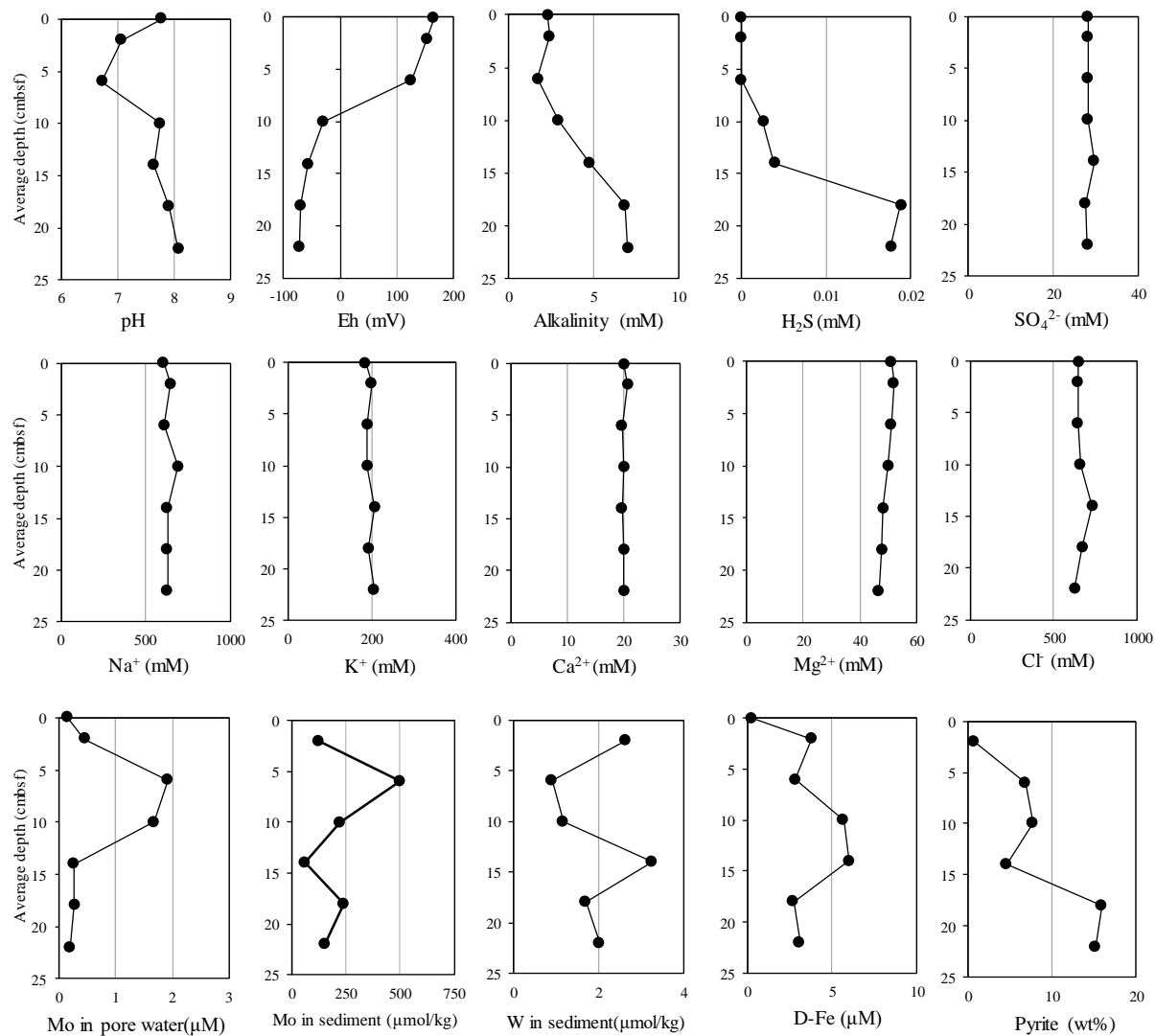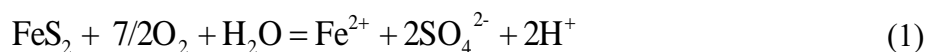
Fig. II-4 Vertical profiles of pH, Eh, alkalinity, H_2S, SO_4^{2-}, Na^+, K^+, Ca^{2+}, Mg^{2+}, Cl^-, dissolved Mo, Mo in sediment, W in sediment, dissolved Fe, and pyrite content.

Figure II-5 shows the S K edge XANES spectra in the 1187MB core and the LCF results. The sulfur species were identified by the peak energy reflecting the oxidation state. Although the fitting of the S XANES spectra by the linear combination fitting is relatively difficult evaluated from R factor because S species in natural sediments would be very complex including many organic and inorganic species, I confirmed the S species in the sediments with depths. In the upper layer (0–4 cmbsf), approximately 50% of the S species were composed of sulfates, such as barite and anhydrite, which can precipitate when seawater is mixed with hydrothermal fluid. In the deeper layer (4–24 cmbsf), several sulfide species, such as pyrite, pyrrhotite, and sphalerite, were observed. Pyrite fraction varied with depth and was not observed at the surface layer. This result suggests that sulfide minerals were oxidized and dissolved by being mixed with oxic seawater. Pyrite and sphalerite can be dissolved by following equations:

$$FeS_2 + 7/2O_2 + H_2O = Fe^{2+} + 2SO_4^{2-} + 2H^+ \qquad (1)$$

$$ZnS + 2O_2 = Zn^{2+} + SO_4^{2-} \qquad (2)$$

Although pyrite is experimentally more soluble than sphalerite, the solubility of sphalerite increased because of the catalytic effect in the presence of pyrite (Abraitis et al., 2004). In the surface layer, both pyrite and sphalerite were dissolved by ambient seawater, resulting in the formation of sulfate species in the sediment. In the intermediate layer (4–12 cmbsf), it is suggested that pyrite and pyrrhotite were gradually dissolved, resulting in the decreased pH level of the porewater, as indicated by Eqn. (1). The sphalerite fraction in the intermediate layer is higher than that in the other layers. The sulfur species demonstrated the various redox conditions generated by the depth as a result of the reaction between the oxic seawater and various minerals (Miyoshi et al., 2015; Yoshizumi et al., 2015).
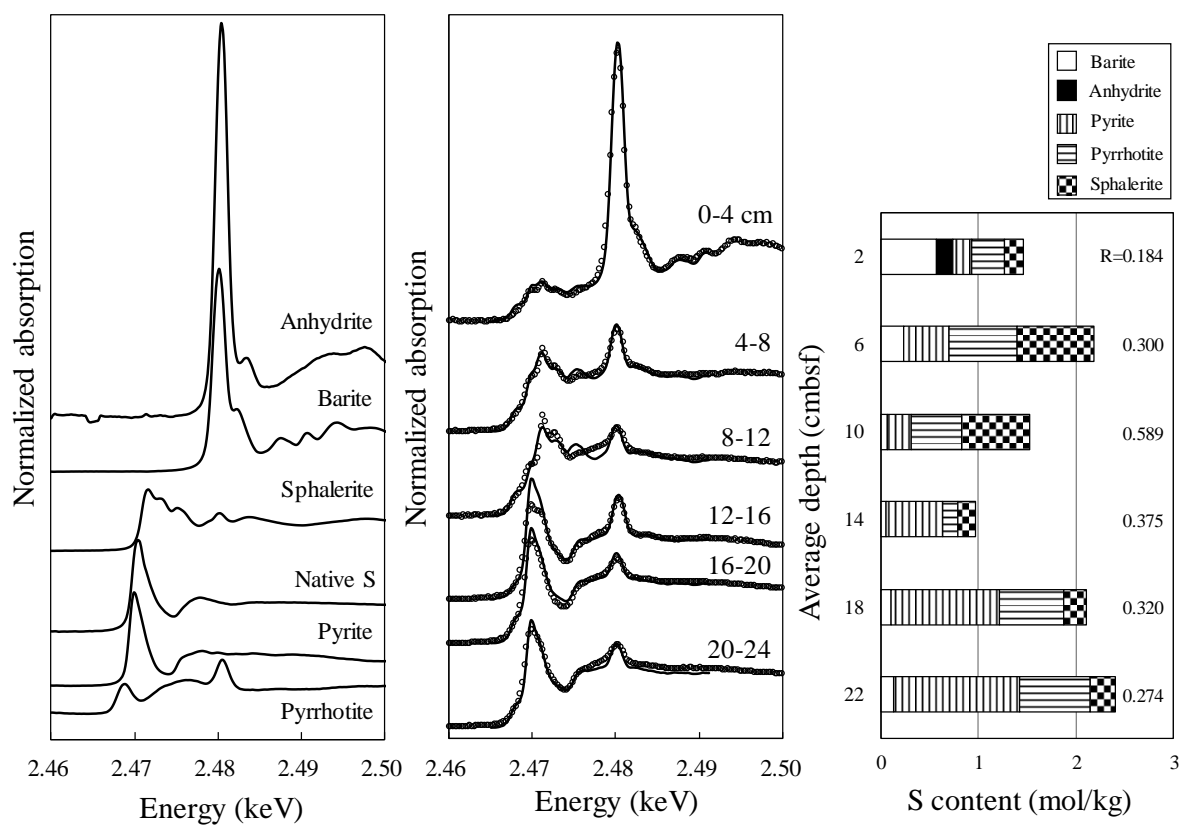
27

Fig. II-5 Normalized XANES spectra of sulfur *K* edge and linear combination fitting results calculated from XANES spectra. White circle dotted line shows the sample spectra and black line shows simulated curve by the linear combination.

The iron species identified by Fe K edge XANES analysis in the sediments were altered by the redox conditions (Fig. II-6). Pyrite fraction increased with depth and was particularly high in the deeper layer (16–24 cmbsf), suggesting the dissolution of authigenic pyrite in the middle layer as described above. Pyrite was considered to have two origins: hydrothermal activity and diagenetic effects. In the hydrothermal field, various sulfide minerals were deposited around the hydrothermal vent (Miyoshi et al., 2015). Most of the pyrite found in the core sample was euhedral, and thus derived from the hydrothermal fluid. However, the deeper layer also contained pyrite framboids (Fig. II-11), which may deposit during diagenesis because of the reaction of Fe^{2+} and H_2S under sulfidic conditions (Wilkin and Barnes, 1996). Ferrihydrite (i.e., amorphous Fe hydroxide) was observed in the surface layer (0–4 cmbsf). Pyrrhotite was observed in all depths except for the surface layer, suggesting that the oxic seawater recharged to the surface sediment oxidized the Fe sulfide minerals to Fe oxide minerals such as ferrihydrite in the surface layer.
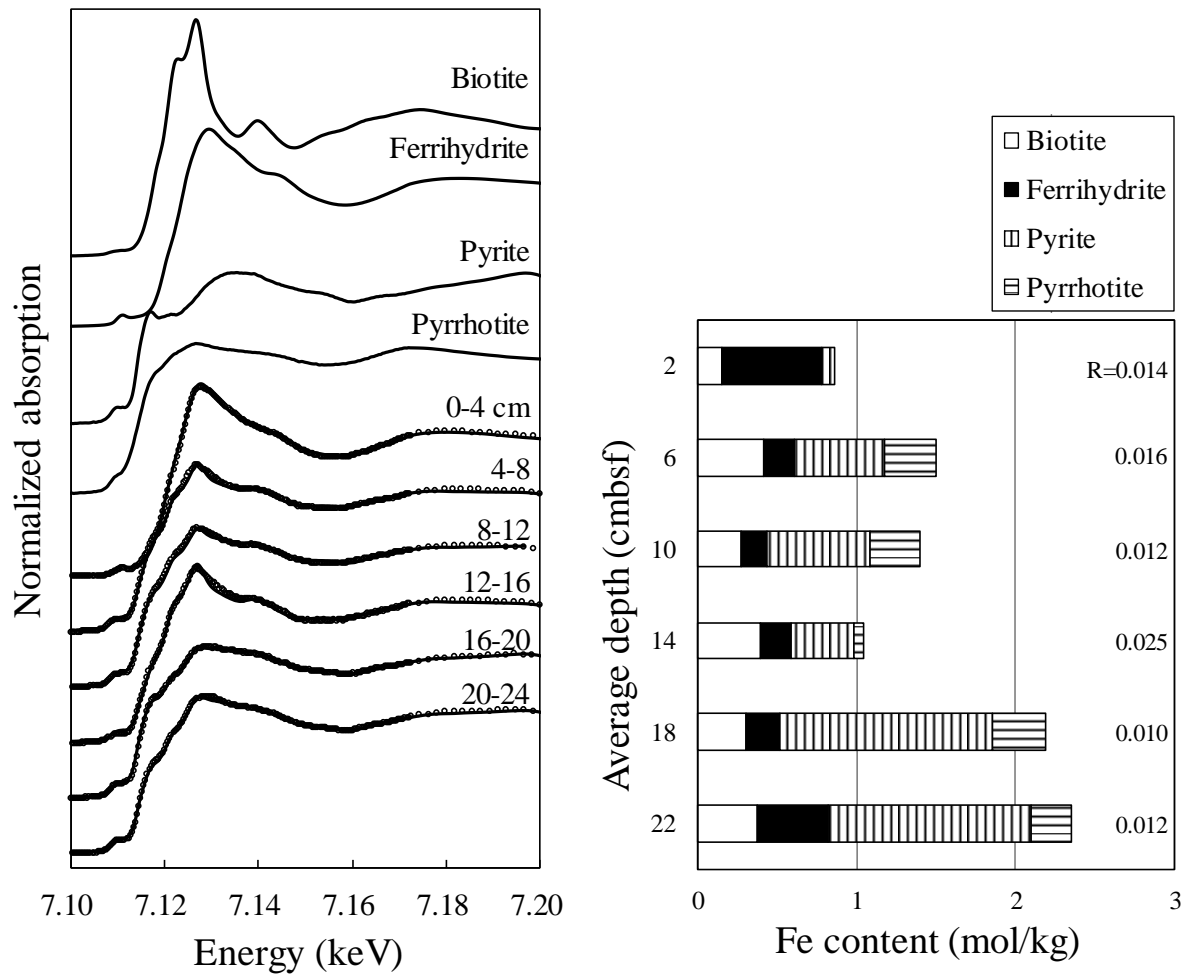
29

Fig. II-6 Normalized XANES spectra of iron *K* edge and linear combination fitting results calculated from XANES spectra and XRF measurement. White circle dotted line shows the sample spectra and black line shows fitting curve simulated by the linear combination fitting.

II.3.2. Molybdenum species in the sediments

Molybdenum species in the sediments affect the partition of Mo during the sediment–porewater interaction. For example, under reducing condition, when the concentration of H_2S reach a specific threshold, MoO_4^{2-} undergoes a reaction to form thiomolybdates and finally forms MoS_4^{2-}. The differences of the dissolved Mo species affect the partition behavior of Mo. Similar to S and Fe, Mo species varied with the depth. Figure II-7 shows the Mo K edge XANES spectra in the sediments. In the XANES analysis, I used tetravalent (MoO_2, MoS_2) and hexavalent (Na_2MoO_4, MoO_3, $(NH_4)_2MoS_4$, MoS_3) Mo species as reference materials. It has been suggested that $(NH_4)_2MoS_4$ can be subject to alteration during storage (Dahl et al., 2013). Thus, EXAFS analysis was conducted for the $(NH_4)_2MoS_4$ reagent to confirm the purity (Appendix 1). This analysis in the Appendix is also effective to show the photoredox during the XAFS measurement by the incident X-ray is also minimal for the reference materials. The hexavalent oxygen-coordinated species (MoO_4^{2-}) was dominant in the upper layer (0–8 cmbsf), whereas sulfur-coordinated species were dominant in the deeper layer (8–24 cmbsf). The increase in oxygen-coordinated species between 0–8 cmbsf was due to the adsorption of MoO_4^{2-} in seawater onto sediments, whereas the proportion of sulfide species (Mo(VI)S_3 and Mo(IV)S_2) increased with the depth. Mo species fitted by MoS_2 are considered to be molybdenite, which generally occurs in hydrothermal environments (Selby et al., 2000; Pašava et al., 2016). Tetravalent Mo sulfide was observed at all depths, with content ranging from 22.9 µmol/kg to 117 µmol/kg (Fig. II-7). The fraction of hexavalent Mo-S species in the deeper layer was higher than that in the upper phase, and Mo content was almost constant except for the 4–8 cmbsf layer. In the deeper layer, aqueous Mo species can be MoS_4^{2-}, possibly because H_2S content exceeded the sulfide-controlled geochemical action point switch (APS) for Mo (11 µM

H$_2$S), at which MoO$_4^{2-}$ sharply transforms to MoS$_4^{2-}$ (Erickson and Helz, 2000). Under this condition, the sediment–porewater partition of Mo is controlled by the adsorption of MoS$_4^{2-}$ onto sediments, and MoS$_4^{2-}$ which may have a stronger affinity than MoO$_4^{2-}$ for the sediment under sulfidic condition. The hexavalent Mo-S species fraction observed in the sediments, which was possibly the results of the adsorption of MoS$_4^{2-}$ onto the sediment, increased in the deeper layer. The presence of tetravalent Mo-S species might have two origins. One is the hydrothermal derived Mo sulfide species mainly consisting of molybdenite, and the other is the post reduction of MoS$_4^{2-}$ adsorbed on the sediments. The adsorption of MoS$_4^{2-}$ onto sulfide minerals and anoxic sediments has already been suggested using XAFS analysis (Bostick et al., 2003; Dahl et al., 2013). These studies stated that (i) the tetravalent Mo-S species was dominant when Mo was adsorbed under sulfidic conditions which was not molybdenite; and (ii) the formation of MoS$_4^{2-}$ is important in the enrichment process of Mo onto the sediment. Our speciation data are consistent with their findings based on the direct detection of Mo species in the sediment.
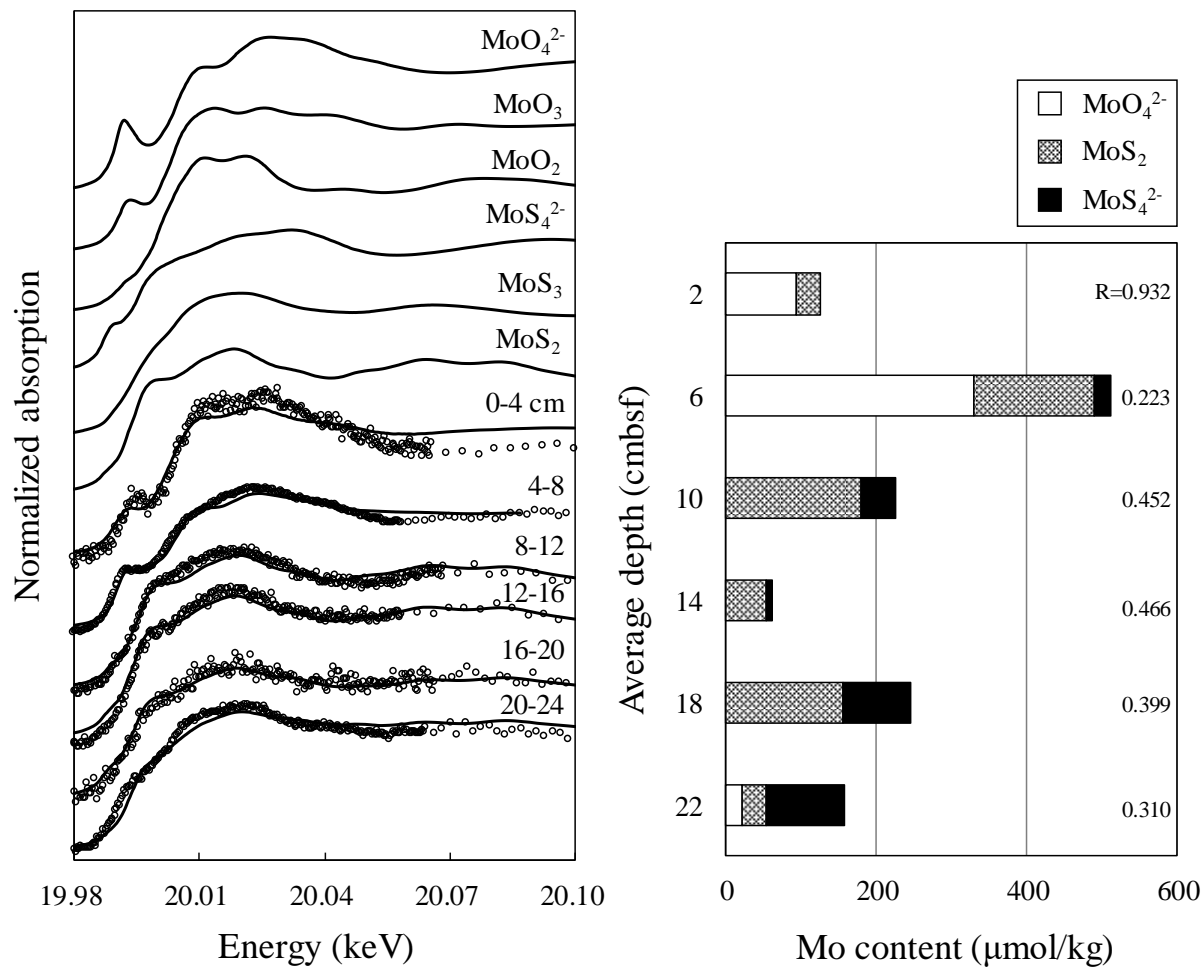
Fig. II-7 Normalized XANES spectra of molybdenum K edge and linear combination fitting results calculated from XANES spectra and ICP-MS measurement. White circle dotted line shows the sample spectra and black line shows fitting curve simulated by the linear combination fitting.

Depth profile of apparent K_d of Mo determined by the core samples and its comparison with the concentration of H_2S and pyrite contents were summarized in Figs. II-4 and II-8. Each apparent K_d value was calculated by the results of the concentrations of Mo in porewater and sediment. In the depth profile, concentration of Mo in porewater exceeded that in the ambient seawater, which indicates that Mo is dissolved from the sediments. In fact, Mo content was

highest in the 4-8 cmbsf. I concluded that the dissolution of Mo from sediment by oxic seawater occurred. On the other hand, K_d increased with depth, which was correlated with H_2S concentration. When the $[H_2S]$ exceeded the APS, K_d value increased sharply, suggesting that the formation of MoS_4^{2-} facilitated the adsorption of Mo to sediment. On the other hand, K_d did not correlate with the amount of pyrite compared with the correlation with $[H_2S]$. The correlation coefficient (r^2) for K_d and H_2S was 0.91 that is better correlation than that for K_d and pyrite as 0.74. Although pyrite is considered to have an important role on the geochemical behavior of Mo under sulfidic conditions, our results showed that sulfidation of MoO_4^{2-} to MoS_4^{2-} in the water is a decisive factor for the partition of Mo in the sediment-porewater system under reducing conditions.
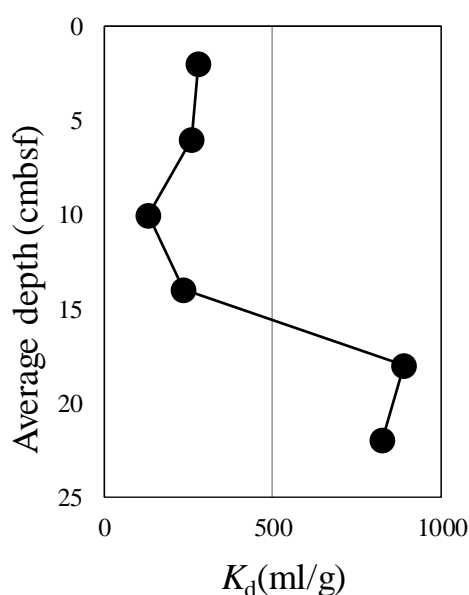

Fig. II-8 Partition coefficient (K_d) of Mo in sediment-porewater system calculated from their actual concentrations in the samples as shown in Fig. II-4.

II.3.3. μ-XRF observation for Mo

To examine the micro-scale distribution of Mo in the sediment and to identify its host phase, a BSE image obtained by scanning electron microcopy (Figs. II-9) and μ-XRF images of Mo and Fe using their Kα lines (Fig. II-10 and II-11) were obtained. The samples consist of many particles including sulfides, silicates, and aluminosilicates which were shown in XRD and XRF analyses described above (Table II-1 and Fig. II-3). In the BSE image, large size particles were identified, ranging from 100 to 300 μm (Figs. II-9a and -9b). Chemical compositions of these particles were determined using energy dispersive X-ray spectroscopy (EDS). After identification of each particle, representative Fe particles in the samples were chosen for the following micro-XRF analyses (Figs. II-10 and II-11). In the figures, the correlation between the Fe and Mo signals in the 0–4 cmbsf and 20–24 cmbsf layers were shown. The chemical composition of Fe-containing particles was measured by energy dispersive spectroscopy (EDS). In the surface layer (0–4 cmbsf), both Fe oxide and sulfide minerals were found (Figs. II-10a and II-10b). The speciation of Fe determined by XANES spectra suggested that the sediment was oxidized by ambient seawater. In that layer, H_2S was not observed, and the aqueous species of Mo is expected to be MoO_4^{2-}. Euhedral pyrite particles which were possibly precipitated in hydrothermal vent were also found in the μ-XRF analysis (Fig. II-10a). Although the Mo partition in the sediment was not large, the XRF intensity of Mo relative to Fe in the pyrite particle, $(Mo)_{cps}/(Fe)_{cps}$ (i.e., (Mo intensity)/(Fe intensity) in the area where Fe intensity is above 1000 counts), was 0.018 ±0.005 (Fig. II-10a). This ratio was higher than that for iron hydroxide (0.0058±0.0024; Fig. II-10b), showing that Mo preferentially adsorbed onto pyrite within the same sediment sample. These ratios showed that the partitioning of MoO_4^{2-} to pyrite was larger than that of Fe hydroxide.
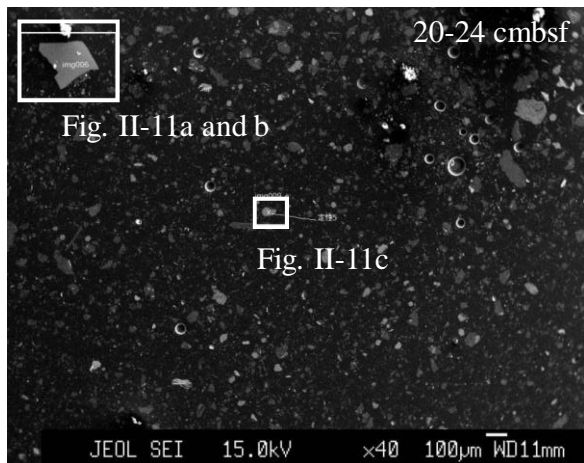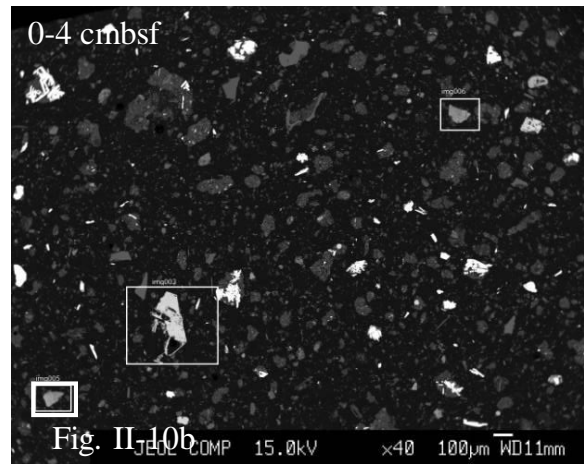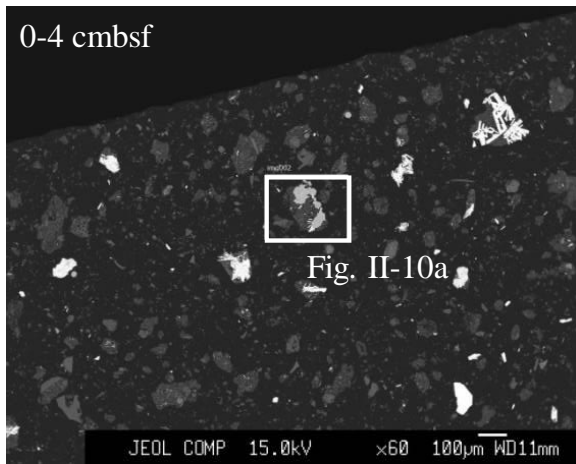
35

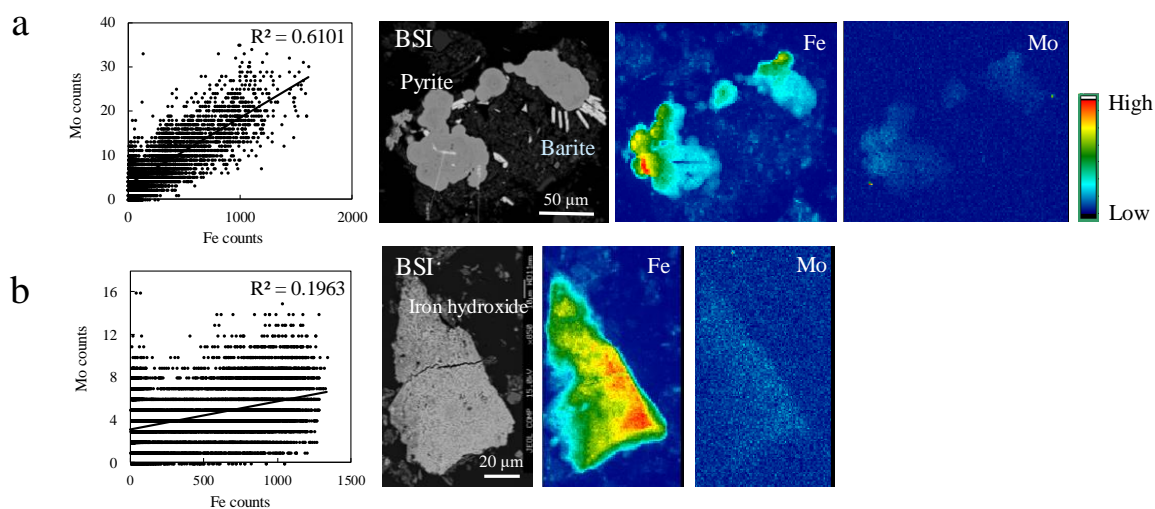Fig. II-9 Backscattered electron images of studied sediments collected at 0-4 cmbsf and 20-24 cmbsf depths

Fig. II-10 Backscattered electron images of sediments (0-4 cmbsf) and µ-XRF images of Fe Kα and Mo Kα. a) Observed pyrite and barite particles; b) Fe hydroxide. Correlation plot between Mo and Fe counts measured for 0.2 sec at each point is also shown.
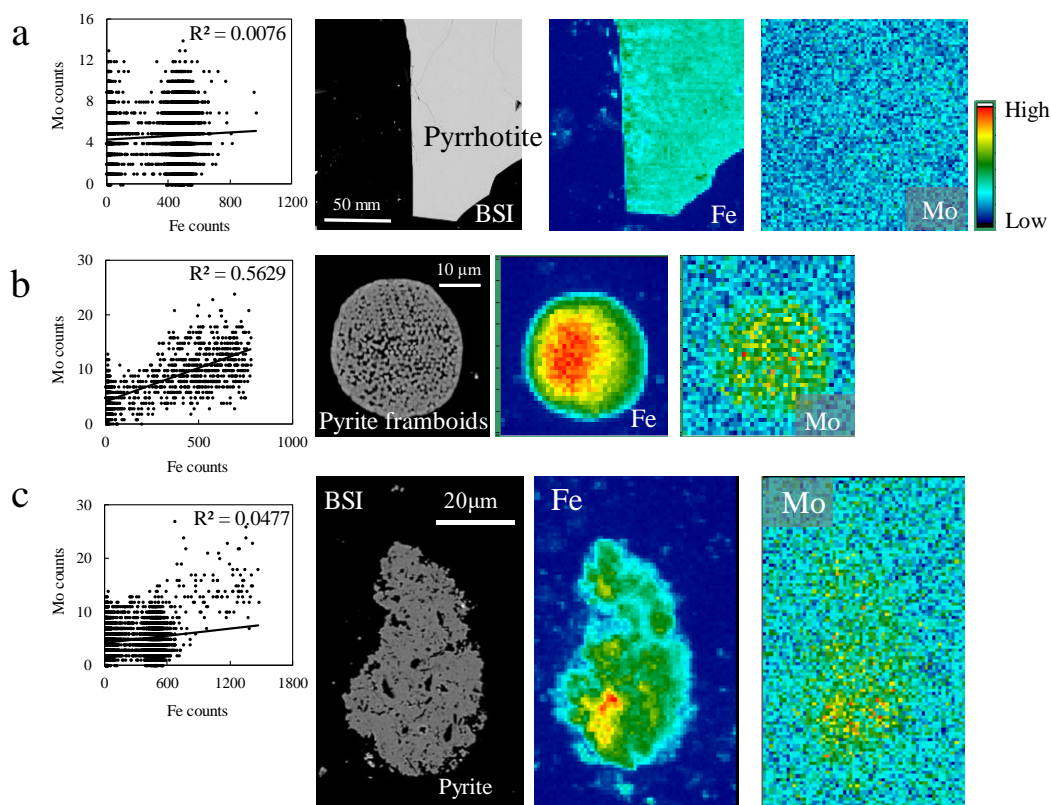

Fig. II-11 Backscattered electron images of sediments (20-24 cmbsf) and µ-XRF images of Fe Kα and Mo Kα. a) Observed pyrrhotite particle; b) pyrite framboids; c) euhedral pyrite. Correlation plot between Mo and Fe counts measured for 0.2 sec at each point is also shown.

37

By contrast, in the deeper layer, various Fe sulfide minerals, such as $Fe_{(1-x)}S$ (pyrrhotite), euhedral pyrite, and pyrite framboids, were observed (Fig. II-11). Pyrrhotite and euhedral pyrite particles were large crystals, which were presumably precipitated in the hydrothermal vent. Pyrite framboids were spherical aggregates of nanoparticles of pyrite precipitated in sulfidic water (Wilkin et al., 1996). The pyrite framboids observed in the 20–24 cmbsf layer suggest that pyrite was formed during early diagenesis in the sediment with sulfidic porewater. Molybdenum signal in pyrite framboids is larger than the background signal in Fig. II-11b, whereas the Mo signal in pyrrhotite cannot be distinguished from the background (Fig. II-11a), which suggests that Mo was distributed to a greater extent to pyrite framboids than pyrrhotite. Molybdenum sulfide species were also observed by bulk XANES analysis (Fig. II-7). The findings suggest that the adsorption of MoS_4^{2-} to pyrite nanoparticles, such as pyrite framboids, is one of the key processes of Mo enrichment under euxinic conditions. Compared to other euhedral pyrite crystals in the sediments, pyrite framboids have a larger surface area, which facilitates the adsorption of Mo.

Larger distribution of Mo onto pyrite particles compared with other minerals such as pyrrhotite and ferrihydrite was observed in the samples. The different adsorption behavior should be affected by the difference of the adsorption mechanism of MoO_4^{2-} and MoS_4^{2-} onto each mineral. Molybdate forms outer-sphere complex when it adsorbs on ferrihydrite (Kashiwabara et al., 2011). In the case of adsorption to pyrite, Bostic et al. (2003) showed that Mo forms inner-sphere complex to pyrite with keeping similar coordination structure to MoO_4^{2-}. Thus, it is possible that sediments at 0-4 and 4-8 cmbsf depths contain MoO_4^{2-} adsorbed on pyrite particles (Bostic et al., 2003). On the other hand, MoS_4^{2-} also forms inner sphere complex on pyrite by forming Fe-Mo-S cubane structure (Bostic et al., 2003). Furthermore, the

adsorption experiment to pyrite in this study showed that partitioning of Mo increased with increase in H_2S concentration which would affect aqueous species of Mo, MoO_4^{2-} or MoS_4^{2-} (Fig. II-12). This result suggests that larger partition of Mo to sediments in the deeper layer was caused by the formation of MoS_4^{2-} in porewater. Although our XANES analysis could determine the oxidation state and neighboring coordinated species such as oxygen- or sulfur-coordinated species, I could not confirm the cubane-type Fe-Mo-S structure in the sediments. However, μ-XRF analysis showed the high correlation of distributions of Mo and pyrite particle, which suggests that Mo is preferentially distributed to the pyrite by forming stable Fe-Mo-S structure in the deeper layer where MoS_4^{2-} was formed. It is important to confirm the XANES and EXAFS spectra of Fe-Mo-S phase by the analysis of the reference material to determine the Mo species in natural sediments in future.
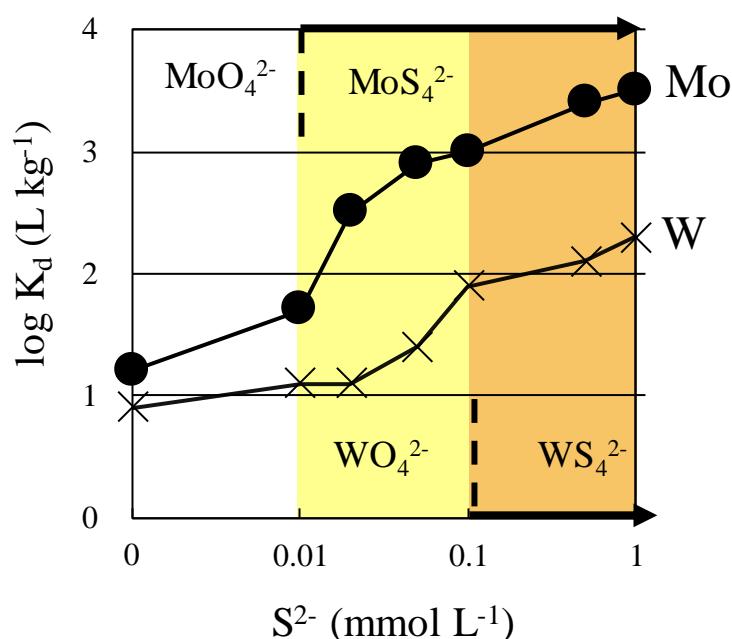

Fig. II-12 Partition coefficient (K_d) of Mo and W adsorbed onto pyrite at various H_2S concentrations. White area shows the region where dominant dissolved species of both Mo and W are oxyanions. Yellow area shows the region where only Mo forms MoS_4^{2-}. Orange area shows the region where both Mo and W form tetrathioanions in solution.

39

II.3.4. Laboratory experiments on the sediment–water partition of Mo and W

Tungsten concentration in the porewater cannot be determined because of the very low concentration in the natural sediment–porewater system in our samples (<0.005 nM in the porewater). Thus, K_d between the porewater and the sediment cannot be directly calculated from the natural sample analyses. To compare K_d between W and Mo in the same system, the adsorption of Mo and W onto the sediment was analyzed at each depth. For this purpose, a certain amount of W was added to the sediment to detect the dissolved W in the aqueous phase. The aqueous concentration of W added to the sediment was adjusted to the average concentration of Mo in the seawater (Sohrin et al., 1987) or to 10 times of the concentration of that. To compare the K_d, an equivalent amount (molar value) of Mo was also added to the sediments. As mentioned, the sulfidation of Mo is considered important for its adsorption behavior onto the sediments. I adjusted the concentration of H_2S in the water phase to be identical to the measured value in the natural porewater at each depth. To calculate the K_d in the adsorption experiment, the dissolution of Mo and W originally contained in the sediment was examined using the same procedure as that of the adsorption experiment without the addition of Mo and W. I assumed that the sum of the added and leached W and Mo from the sediments is the aqueous concentrations of these elements before the adsorption; in this way, the apparent K_d of W and Mo in the system were estimated. The results of the adsorption experiment revealed that the K_d of W did not significantly change with the depth, whereas the K_d of Mo increased with the depth (Fig. II-13). The K_d values for Mo determined by the adsorption experiment displayed a trend (Fig. II-13) similar to that observed for the natural samples (Fig. II-8). Figure II-13 was depicted by using the adsorption data in the systems of our sediment samples and synthetic seawater where concentrations of Mo and W were adjusted to those in natural seawater.

These trends of adsorption behavior were observed under both two experimental conditions with different W and Mo concentrations adjusted in the system. Figure II-14 shows the correlation of Mo or W concentration between water and sediments after the experiments under various experimental conditions. The adsorbed concentration of Mo and W increased linearly with the increase in the water concentration at any depth. This finding suggests that K_d values obtained in this experiment can be estimated in the concentration range in Fig. II-14, which includes the Mo concentration in the porewater observed in the natural system (as mentioned above, H_2S concentration was adjusted to the value observed in the natural system). The K_d of Mo calculated in the adsorption experiment ranged from 2.5 to 3600, whereas the apparent K_d calculated from the natural sample ranged from 132 to 890. The difference in the range of K_d values suggests that the natural samples could contain Mo inside the solid phase precipitated during hydrothermal activities, which cannot be leached and then be involved in the adsorption–desorption and/or precipitation–dissolution reactions. Nonetheless, the similar overall trends found in the laboratory and natural K_d (Figs. II-8 and II-13) imply that the laboratory data are useful in elucidating the sediment–porewater partitions for Mo and, more importantly, for W, given that natural data were unavailable for the latter element.
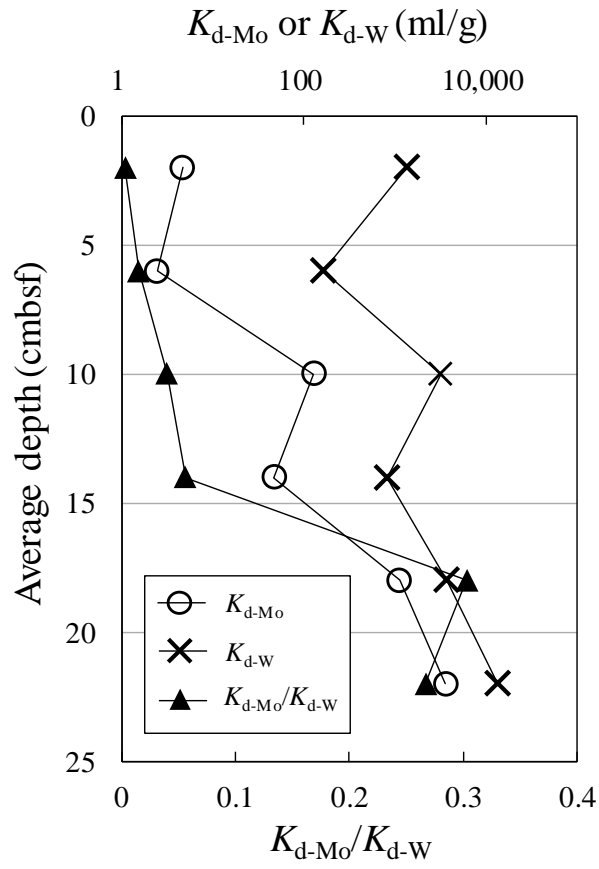
Fig. II-13 Partition coefficient (K_d) of Mo and W determined by adsorption experiment when initial concentrations of aqueous Mo and W were 100 nM, and the ratio of K_{d-Mo}/K_{d-W}. The upper horizontal axis shows the each K_d values of Mo and W in the adsorption experiments as logarithmic scale. The lower horizontal axis shows the ratio for K_{d-Mo}/K_{d-W}.
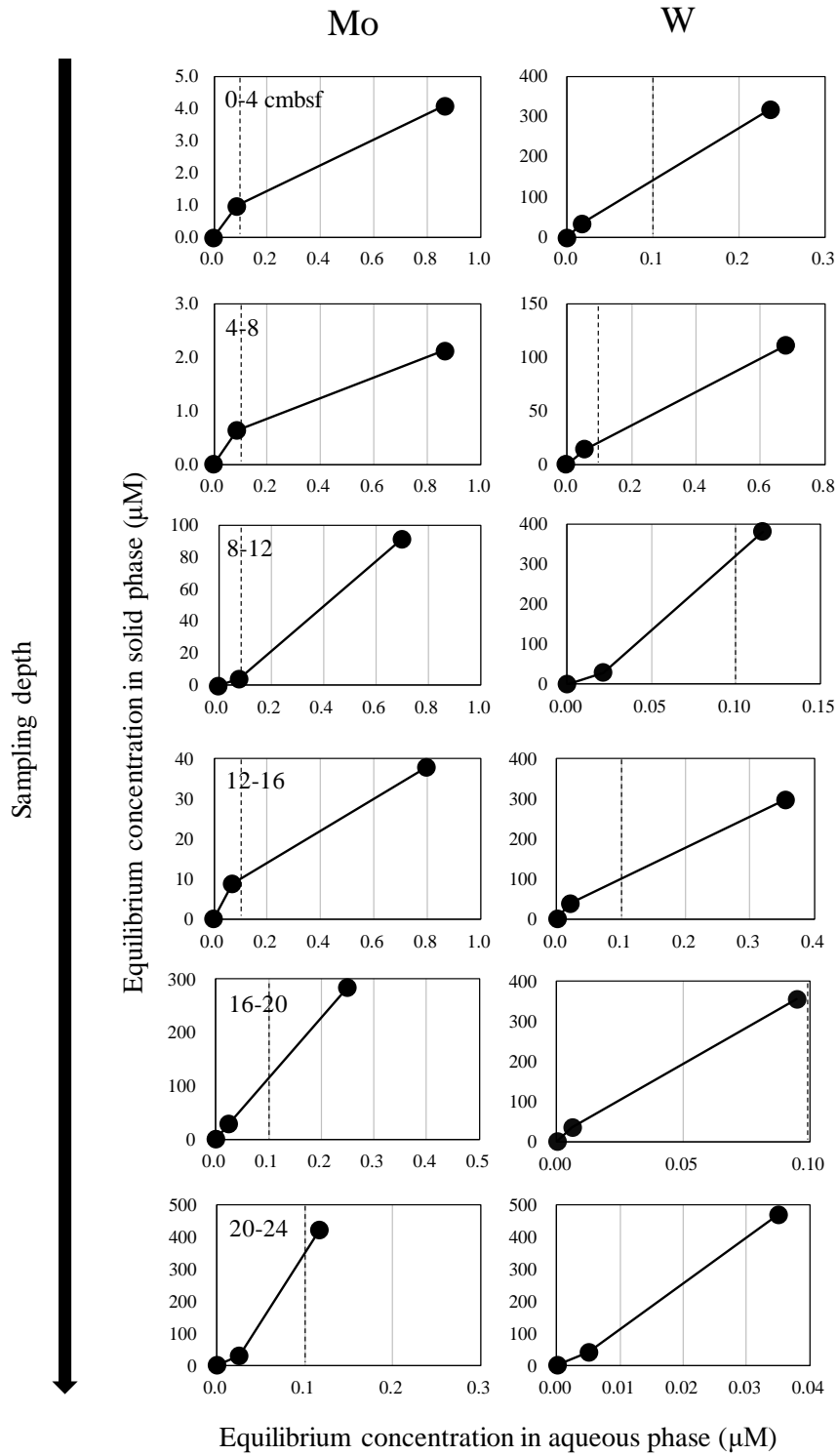
Fig. II-14 Relationship of Mo and W concentrations between sediment and water phases for the sediments at various depths. Dotted lines show the average concentration of Mo in modern seawater (Sohrin et al., 1987).

In this sediment, the formation of thiotungstate was unlikely because the H_2S concentration (~0.020 mM) was not high enough to form WS_4^{2-} from WO_4^{2-} based on their formation constants (Mohajerin et al., 2014). Tungstate is the dominant species in the aqueous phase that controls the partitioning of W in the system. The upper layer containing oxic sediments and larger amount of iron hydroxide demonstrates larger degree of adsorption of W compared with that of Mo, which is because WO_4^{2-} forms an inner-sphere complex when adsorbed to ferrihydrite (Kashiwabara et al., 2013), whereas Mo forms an outer-sphere complex to iron hydroxide (Kashiwabara et al., 2011).

The partitioning of W to sulfide minerals is poorly known. I performed an adsorption experiment with pure pyrite to determine the affinity and chemical form of W when adsorbed onto pyrite (Fig. II-15). The peak energy of W L_3 edge XANES varied with the chemical species and oxidation states of W. When WO_4^{2-} adsorbed to pyrite, W preserved oxygen-coordinated species, such as the WO_4^{2-} solution, on pyrite (Fig. II-15). For W dissolved as WS_4^{2-} in the system, W was adsorbed as sulfur-coordinated species like WS_4^{2-}. In other words, the species adsorbed onto the pyrite is dependent on the dissolved species of W within our experimental conditions. As for the adsorption of WO_4^{2-}, WO_4^{2-} forms an outer-sphere complex to pyrite, because the XANES spectrum suggests that W is present as oxygen-coordinated species. Thus, the high stability of the oxygen-coordinated species of W is responsible for the lower affinity of W for pyrite compared with that of Mo (Holm et al., 2011).
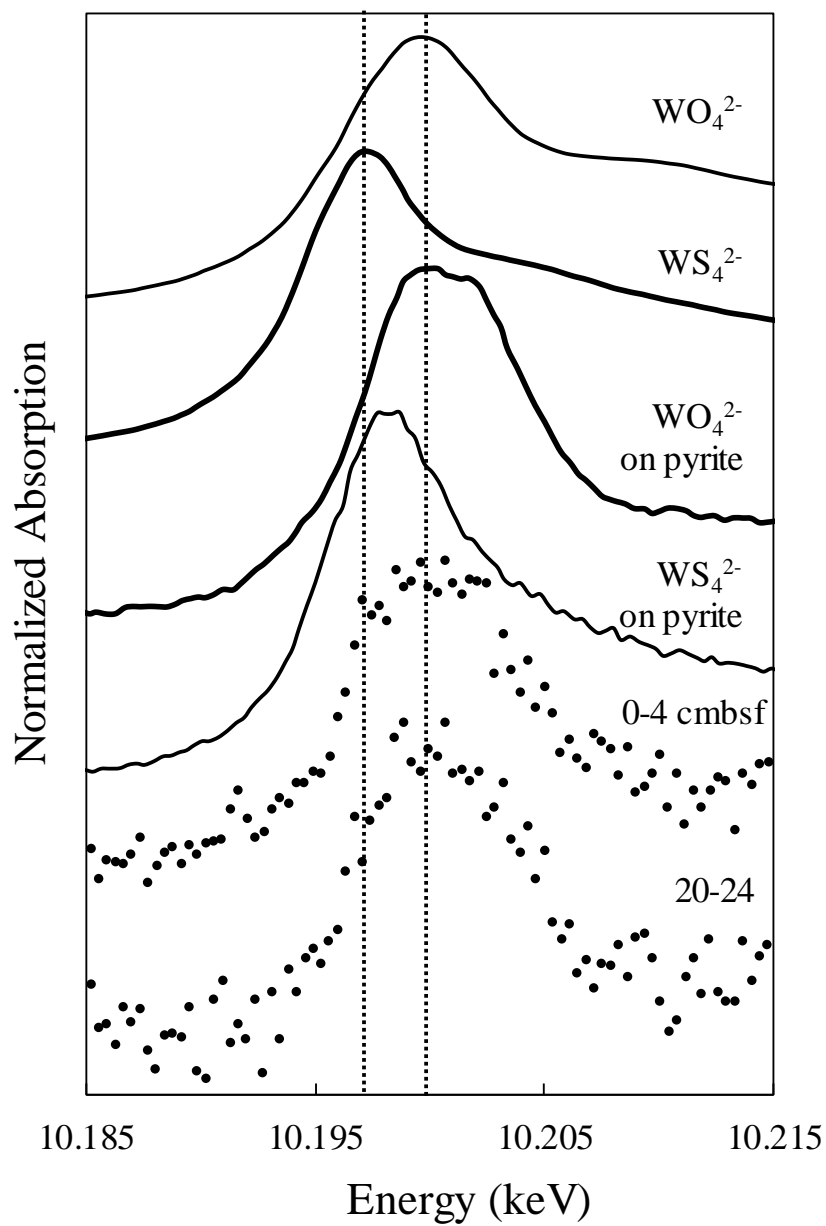
Fig. II-15 Normalized XANES spectra of W L_3 edge for (i) reference materials, (ii) W adsorbed on pyrite, and (iii) W originally contained in sediments at 0-4 and 20-24 cmbsf.

II.3.5. Speciation of W in natural sediments by sensitive WD-XAFS

In this study, I used WD-XAFS method (Kashiwabara et al., 2010; 2013) to determine the chemical species of W in natural samples, including trace amount of W (Fig. II-15). I measured W L_3 edge XANES in two sediment samples (0–4 and 20–24 cmbsf), in which W concentrations were 2.6 and 2.0 μmol/kg, respectively. Without the BCLA, the intense Zn Kα line interfered with the W Lα because of the much greater amount of Zn in the sediment (0–4 cmbsf: 107 mmol/kg; 20–24 cmbsf: 55 mmol/kg) compared with that of W (Fig. II-16a). Consequently, the SDD was saturated by the interference X-ray signals, thus hindering the collection of the W XANES spectra. However, with the BCLA, Zn and other interference signals were attenuated, thereby facilitating the successful extraction of the W signal to measure the W XANES spectra for the samples (Fig. II-16b). The W species originally included in the two sediment samples were oxygen-coordinated species, indicating that W was adsorbed onto sediments as WO_4^{2-} even in the presence of H_2S in the porewater. This chemical behavior was completely different from that of Mo, which was adsorbed onto the sediment as sulfide under sulfidic conditions. In the 20–24 cmbsf, thermodynamic calculation suggests that dissolved species of Mo should be MoS_4^{2-}, whereas W species should be WO_4^{2-}. Our XANES results were consistent with the predicted chemical species of Mo and W based on the formation constants in the sediments and porewater.
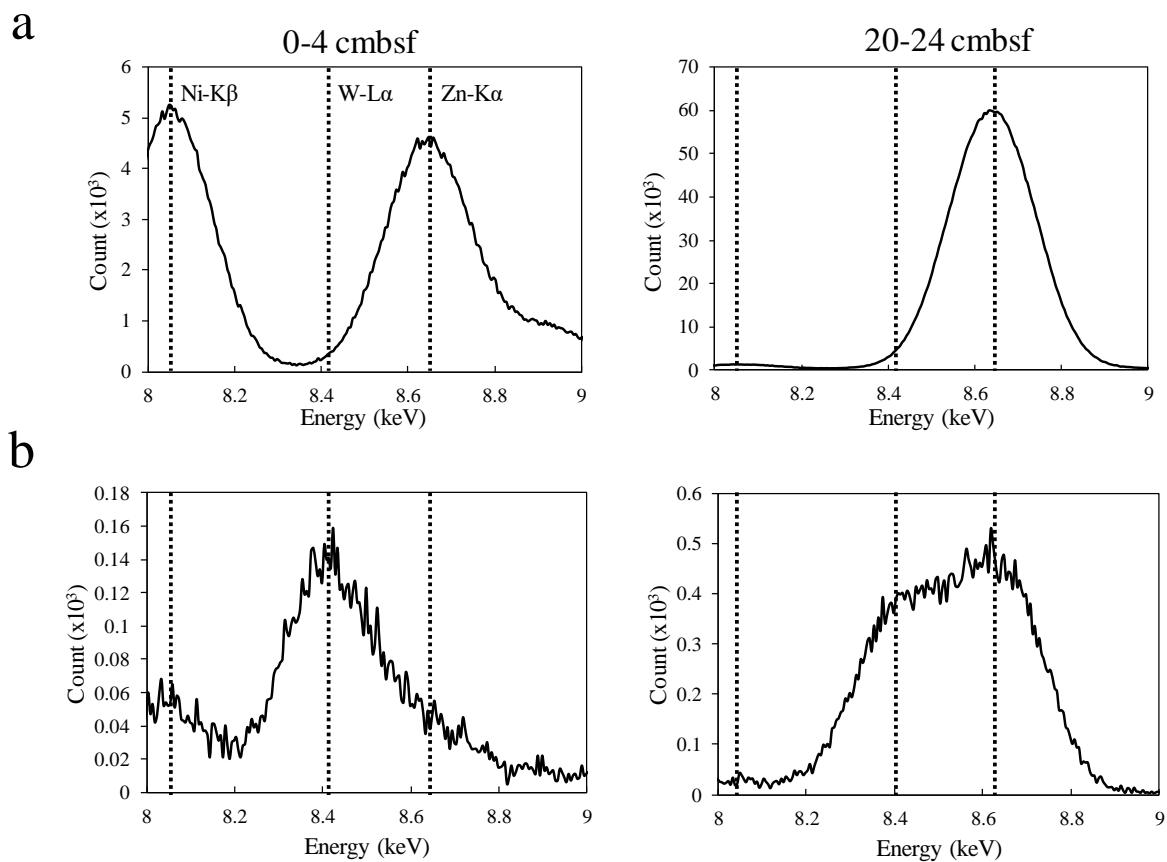
Fig. II-16 X-ray fluorescence spectra of two sediment samples (0-4 cmbsf and 20-24 cmbsf) excited by an energy of 10.208 keV at a range of 8.0-9.0 keV. a) XRF spectra without BCLA. b) XRF spectra with BCLA.

II.3.6. Comparison of Mo and W

The findings in this study suggest that W adsorbs onto the sediments in the upper layer to a greater extent than Mo. The sediments were oxic and are comprised of oxide and sulfate minerals, such as ferrihydrite and barite. This result is consistent with previous adsorption experiments of Mo and W onto ferrihydrite (Kashiwabara et al., 2011; 2013), which showed that Mo forms an outer-sphere complex and weakly adsorbs onto ferrihydrite, whereas W forms an inner-sphere complex with high stability as adsorbed species.

By contrast, sediments in the deeper layer were composed of sulfide minerals, such as pyrite, pyrrhotite, and sphalerite, and the porewater contained 0.01 to 0.02 M of H_2S. Under that condition, the partitioning of Mo to the solid phase became more prominent because of its high affinity for sulfide minerals with larger surface areas, such as pyrite framboids. Therefore, Mo is distributed to the sediment to a much greater extent in the deeper part than in the upper part. However, dissolved W species was kept constant as WO_4^{2-}, which was adsorbed onto the sediment as an oxygen-coordinated species even in the deeper layer.

The difference indicates that the water solubilities of the two elements vary depending on the redox condition in the sediment–porewater system. The K_d for each depth can be severely affected by the difference in particle sizes of the sediments at each layer because surface area of each particle which can adsorb Mo and W from water phase varies with the particle size. Thus, the $K_{d\text{-Mo}}/K_{d\text{-W}}$ ratio was employed to eliminate this effect and to compare the differences in the partition behaviors of Mo and W at various depths (Fig. II-13). This result further proves that Mo is more soluble under oxic conditions, but much less in reducing (or euxinic) environments. Under the redox condition of our study samples ([H_2S] < 0.020 M), the adsorbed species of W was still oxygen-coordinated species, indicating that W, unlike Mo, preferentially

forms oxygen-coordinated species, which was detected by WD-XAFS method used for the first time for W species in a natural system. Consequently, W is distributed to sediments to a greater extent in oxic environments, but further increase in its partition to euxinic sediments was not observed. The water solubilities of the two elements showed contrasting changes depending on the redox condition.

These partition data with speciation analysis are also important in examining the solubilities of Mo and W in their geochemical processes. For hydrothermal mineral deposits, molybdenite as ore sulfur-coordinated Mo species and scheelite ($CaWO_4$)/wolframite $(Fe,Mn)WO_4$ as oxygen-coordinated W species are simultaneously observed in the same deposit possibly because of the difference in their preference to form Mo-S and W-O species, respectively (e.g., Lu et al., 2003). Under our samples' condition, the dominant dissolved W species should be WO_4^{2-} from the formation constant of WS_4^{2-} (Mohajerin et al., 2014). To understand the difference in the partition behaviors of Mo and W under highly sulfidic conditions ($[H_2S] > 100$ μM), the adsorption behavior of WS_4^{2-} in a natural system should be explored in a future study.

To simulate that condition, adsorption of WS_4^{2-} onto pyrite was examined and the partition data obtained were compared with that of Mo. Figure II-17 shows the adsorption isotherms of MoS_4^{2-} and WS_4^{2-} adsorbed on pyrite in the presence of 1.0 mM of H_2S at pH 7.0. Compared with Mo, the partitioning of W to pyrite was very low. The calculated K_d values of Mo and W onto pyrite (log K_d = 2.37 and 0.37 for Mo and W, respectively) showed the opposite trend to the isotherms observed in the ferrihydrite system (log K_d = 3.02 and 4.90 for Mo and W, respectively) calculated based on Kashiwabara et al. (2011, 2013). The lower adsorption of W was observed under various pH and H_2S concentrations in our experiments (Figs. II-12 and II-18). Adsorption of both Mo and W decreased with the increase in pH, which indicates that

surface charge of pyrite and protonation of Mo and W anions affect the dependence of their adsorption on pH (Fig. II-18). Although the difference in K_d values of adsorption onto pyrite between Mo and W was also observed under any H_2S concentration examined, the difference was larger when the H_2S concentration was high in the system (Fig. II-12). Under highly sulfidic condition, both Mo and W are likely form tetrathioanion in the aqueous phase. The larger difference of K_d between Mo and W suggests the adsorption mechanism of WS_4^{2-} onto pyrite is different from MoS_4^{2-} which forms Fe-Mo-S cubane structure (Bostick et al., 2003). However, our EXAFS spectra of W L_3 edge adsorbed on pyrite was not clear to confirm the adsorbed species (Fig. II-19). Although the EXAFS spectra was in relatively poor quality, W species adsorbed on pyrite was not similar with aqueous WS_4^{2-}, which indicates that W forms inner-sphere complex onto pyrite as similarly observed for Mo. Thus, it is not easy to explain the difference of K_d value between Mo and W for the adsorption on pyrite, if the adsorption mechanism of W is similar to that of Mo. However, it is possible that the affinity of W and Mo for O or S in terms of coordination chemistry are an important factor to explain the difference of their partition behaviors (Holm et al., 2011). In other words, Mo which prefers to form bonding with S is more stable in sulfide minerals which is considered to be a main solid phase under sulfidic environment.

The biogeochemistry of various elements is affected by the changes in the chemical composition of seawater caused by the redox conditions (Anbar, 2008). A highly euxinic condition should prevail in a marine system under low atmospheric oxygen conditions (Zerkle et al., 2005). Some studies indicate that euxinic ocean had a considerably different elemental composition that changed the bioavailability of each element (Saito et al., 2003; Williams and da Silva, 2003). The difference in the water solubilities of Mo and W under various redox

conditions shown in our study provides insight into the bioavailabilities of these elements in

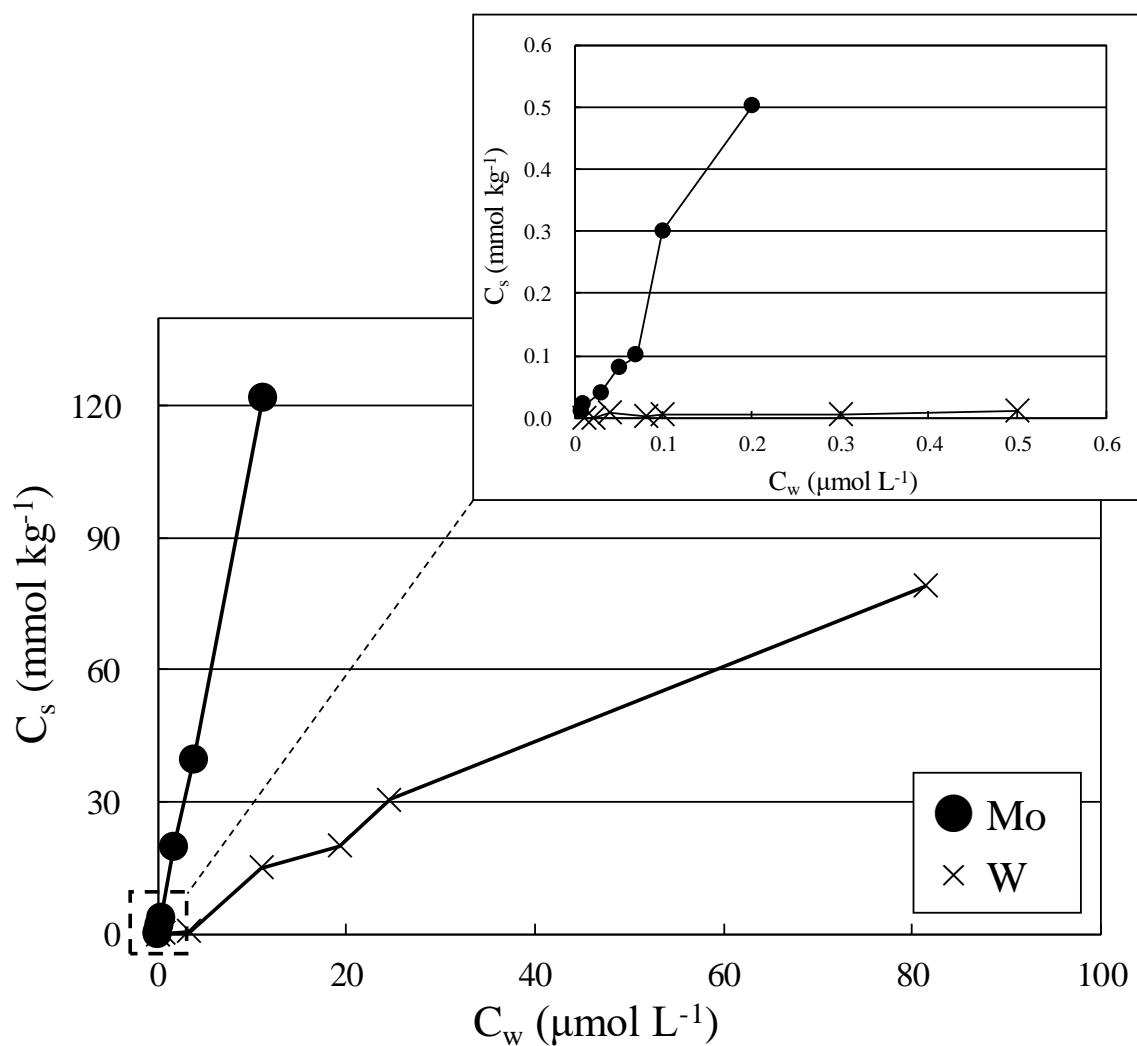the paleocean, which can change as the Earth's environment evolves chemically.

Fig. II-17 Adsorption isotherms for Mo and W on pyrite at pH 7.0 (I = 0.70 M). The inset figure expands the isotherm for the range of equilibrium W concentration below 0.5 nmol L^{-1}.
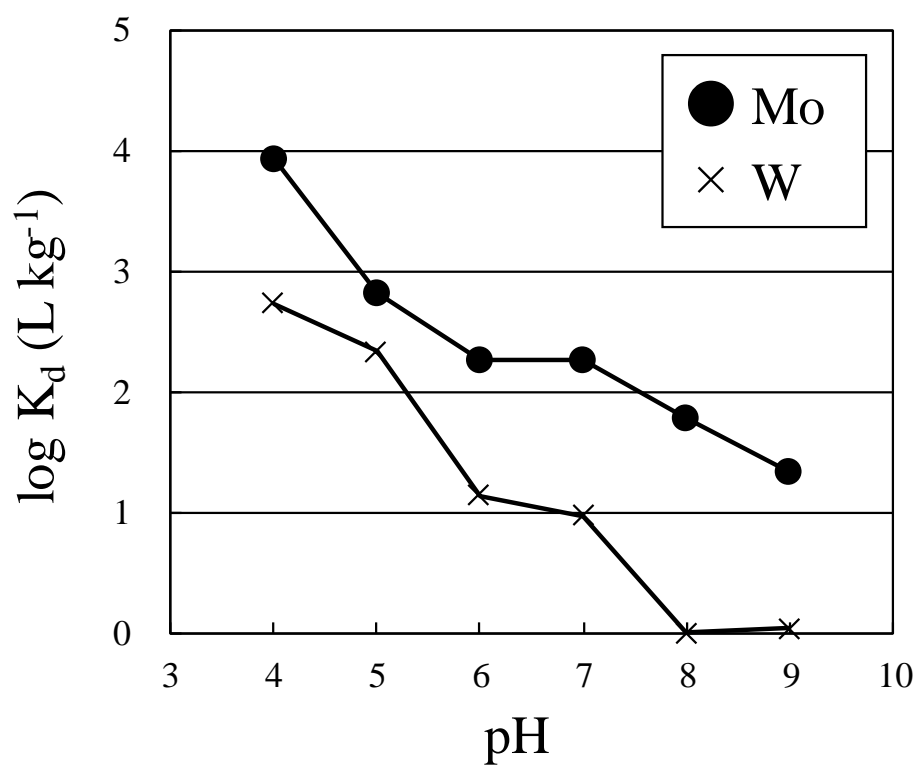
Fig. II-18 Partition coefficient (K_d) of Mo and W at various pH values between pH 4.0 and 9.0.

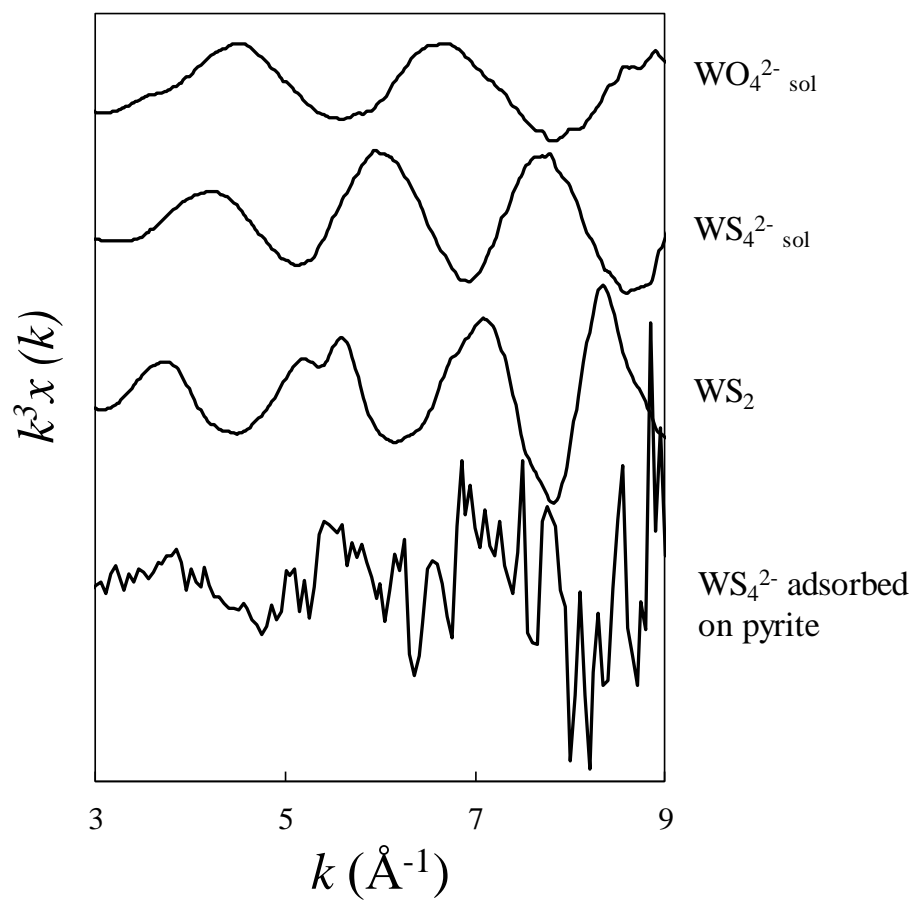Fig. II-19 Tungsten L3 edge k^3-weighted $x(k)$ spectra of adsorbed on pyrite and reference materials (WO_4^{2-}, WS_4^{2-}, and WS_2).

II.4. Conclusions

In this study, chemical composition and speciation analyses were conducted on sediment core and porewater samples collected near the hydrothermal vent in Okinawa, Japan, thus providing natural system with various redox conditions at different depths to examine the sediment–porewater partitions of Mo and W species. The surface sediment (0–4 cmbsf) have more oxide and sulfate minerals compared to other depth. Pyrite was dissolved in the middle layer (4–12 cmbsf) by discharging oxic ambient seawater. Sulfidic conditions were formed in the deeper layer (12–24 cmbsf), wherein sulfide minerals with pyrite framboids were formed and Fe and S were enriched in the sediments.

Our analyses of natural samples indicated that Mo species in the sediment are influenced by the redox condition, the mineralogical composition of the sediment, and the dissolved species of Mo. The apparent partition coefficient (K_d) of Mo between sediment and porewater increased with increase of [H_2S], suggesting that low K_d value in the upper layer is due to the weak adsorption of MoO_4^{2-} to both oxide and sulfide minerals. By contrast, under sulfidic conditions, MoS_4^{2-} is likely to adsorb onto sulfide minerals as indicated by the high K_d value.

In addition, to compare the K_d values of Mo and W, I performed adsorption experiment of aqueous Mo and W onto natural sediments as well as pure ferrihydrite and pyrite. Under oxic conditions, WO_4^{2-} has a higher affinity for sediments because of formation of an inner-sphere complex with ferrihydrite (Kashiwabara et al., 2013). Even in the deeper layer where sulfide minerals were dominant, W is unlikely to form thiotungstate in the examined system (Mohajerin et al., 2014). The adsorption of WO_4^{2-} to sulfide minerals was examined using pure pyrite material, which revealed its weak adsorption for sulfide minerals than oxide minerals. In the speciation analysis using WD-XAFS method, the chemical species of W in the natural sediment

was found to be oxygen-coordinated species even under sulfidic conditions; this finding can explain the difference of partition behaviors of Mo and W under the studied redox conditions. Furthermore, partition data of Mo and W adsorbed on pyrite showed that partition to pyrite of Mo and W were opposite trend to that of ferrihydrite suggesting that the solubilities of these elements would varied with redox condition and H_2S concentration.

This study provides the partition data about systematic dependence of water solubilities of Mo and W on the redox condition. As previously reported, under oxic conditions, the partition of W to the solid phase such as ferromanganese oxide is higher than that of Mo (Kashiwabara et al., 2011; 2013). This result is consistent with a previous quantitative analysis of seawater composition (Sohrin et al., 1987; 1999). Under sulfidic conditions, the apparent partition of W to the solid phase is comparable with that under oxic condition, whereas the sulfidation of Mo enhances the partition of Mo to the solid phase. These results indicate that the concentration of Mo and W in anoxic (euxinic) seawater were different from that in oxic seawater. The simultaneous investigation of the geochemical behaviors of Mo and W in this study contributes to the better understanding of their water solubilities under various redox conditions.

Appendix 1

It has been suggested that $(NH_4)_2MoS_4$ can be subject to alteration during storage (Dahl et al., 2013). Thus, EXAFS analysis was conducted for the $(NH_4)_2MoS_4$ reagent to confirm the purity. In addition, it is possible that reagents that were used for reference materials of Mo K edge XANES analysis were oxidized or reduced during the preservation in laboratory and/or during measurement of XAFS analysis. Thus, EXAFS analysis was performed to make sure that the reagents have kept the chemical species in their initial forms.

Molybdenum K edge EXAFS spectra of standard materials (Na_2MoO_4 $2H_2O$, MoO_2, MoS_3 $2H_2O$, MoS_2) were measured in transmission mode at BL01B1 in SPring-8. EXAFS analysis was performed using REX2000 ver. 2.5 (Rigaku Co.) and FEFF7 (Zabinsky et al., 1995). The x(k) function was extracted from the raw spectrum by a spline smoothing method. E_0 was set at the edge inflection point for all the samples.

A radial structural functions (RSFs) were obtained by Fourier transform of the k^3 -weighted x(k) functions from k space to r space at the range of 3.0–13.0 Å^{-1}. The inversely Fourier filtered $k^3x(k)$ were analyzed with a usual curve-fitting method. The theoretical backscattering amplitudes and phase-shift functions employed in this fitting procedure were calculated using FEFF7. In this calculation, the backscattering amplitudes and phase-shift functions for Mo–O, Mo–S, and Mo–S were extracted from the structure of Na_2MoO_4, $(NH_4)_2MoS_4$, and MoS_2, respectively. The quality of the fit was given by the goodness of fit parameter, R factor, defined as
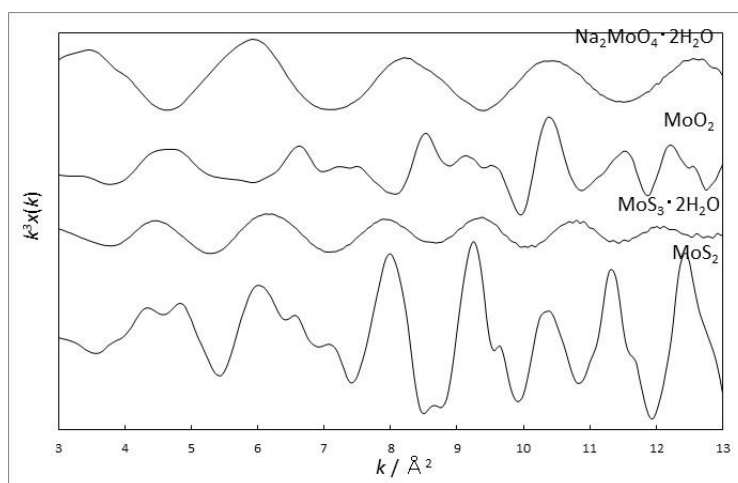

Figure A1 Mo K-edge EXAFS spectra of reference materials. k^3-weighted $x(k)$ spectra.

$$R = \frac{\sum(x_{obs}(E) - x_{cal}(E))^2}{\sum x_{obs}(E)^2}$$

where $x_{obs}(E)$ and $x_{cal}(E)$ are the experimental and calculated absorption coefficients at a given energy (E), respectively.

Figures A1 and A2 show k^3-weighted $x(k)$ spectra and RSFs (phase shift not corrected) of reference materials. In RSFs, each reference material had different shells derived from back scattering by the coordinated atoms. I summarized the fitting results of curve-fitting of the inversely Fourier filtered $k^3x(k)$ in Table A1. In the table, CN means the coordination number which was kept invariable in the refinement. R means the interatomic distance between Mo and each coordinated atom. ΔE_0 and σ^2 mean E_0 shift and Debye–Waller factor, respectively. In the curve fitting, I varied R, E_0, and σ^2 values.   As a result, Na_2MoO_4 $2H_2O$ had only one peak at R + ΔR = 2.5 Å which consists of molybdate tetrahedral (Bramnik and Ehrenberg, 2004). The three peaks observed in MoO_2 at 2.0 Å, 2.5 Å, and 3.7 Å show the octahedral structure of MoO_2
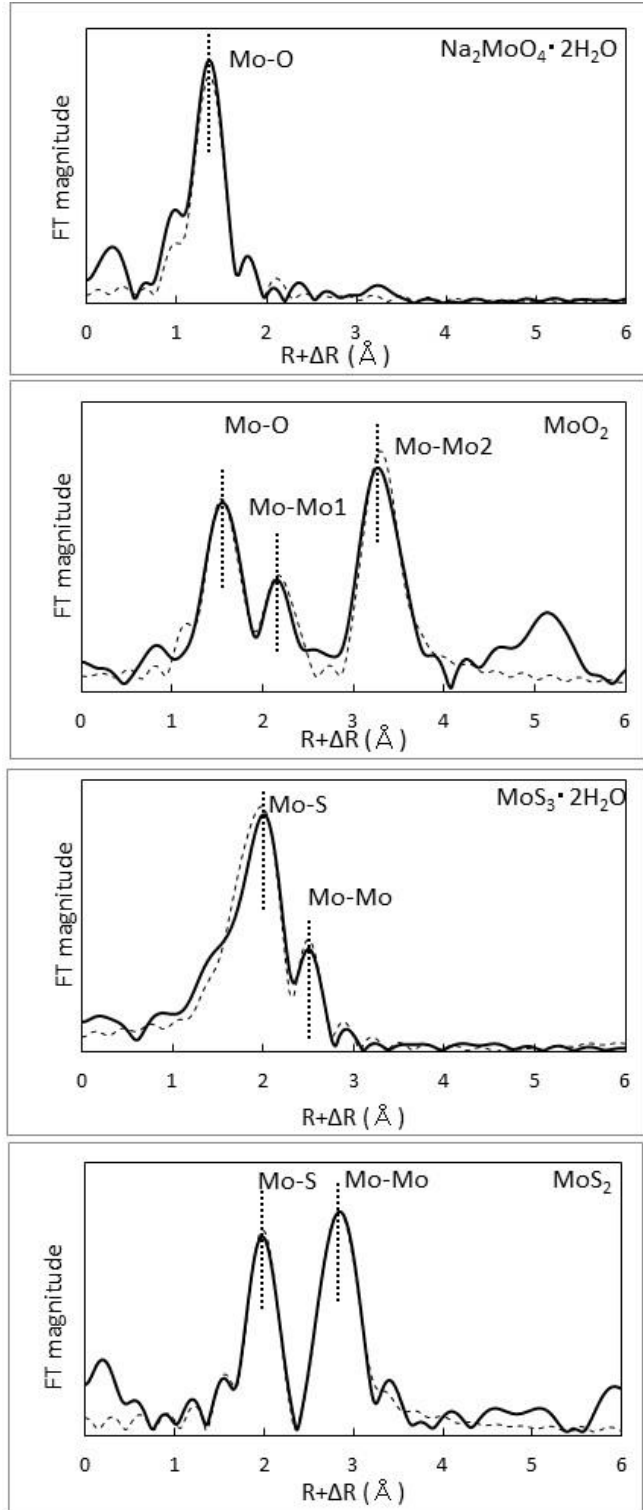

Figure A2 Mo K-edge EXAFS spectra of reference materials. RSF of spectra of . k^3-weighted $x(k)$ spectra (phase shift not corrected).

(Ressler et al., 2001). Sulfide species such as MoS$_3$ 2H$_2$O and MoS$_2$ had first peak at longer distance compared with oxides showing sulfur coordination of these reagents. Our EXAFS data of these sulfide species consist of their coordination structures (Cramer et al., 1983; Lee et al., 2014). In all EXAFS data of reference materials, the other peaks caused by the change of chemical species or contamination cannot be identified. Thus, I concluded that reference materials that I used in this study did not transform to other species and kept their original species.

Table A1 The structual parameters of Mo reference materials

	Shell	CN	R (Å)	ΔE0 (eV)	σ^2 (Å^2)	R (%)
Na$_2$MoO$_4$.2H$_2$O	Mo-O	4	1.78	8.6	0.045	1.24
MoO$_2$	Mo-O	6	2.01	0.7	0.060	5.41
	Mo-Mo$_1$	1	2.53		0.050	
	Mo-Mo$_2$	9	3.68		0.050	
MoS$_3$・2H$_2$O	Mo-S	6	2.43	9.7	0.090	4.92
	Mo-Mo	2	2.93		0.070	
MoS$_2$	Mo-S	6	2.41	4.9	0.060	0.37
	Mo-Mo	6	3.16		0.050	

Chapter III.   SPECIATION OF TUNGSTEN IN EUXINIC SEDIMENTS USING WAVELENGTH DISPERSIVE XAFS FOR THE COMPARISON OF ITS DISTRIBUTION TO SEDIMENT WITH MOLYBDENUM

III.1. Introduction

As indicated in Chapter I, difference of geochemical behaviors of congeners, Mo and W, has been of great interest in various studies (e.g., Williams and Da Silva, 2003; Kishida et al., 2004; Mohajerin et al., 2016). However, actual results of the difference observed in natural samples were mainly found in their abundance data without any speciation results in particularly for W. The reason why there are few studies about W behavior under anoxic and sulfidic condition is the difficulty in speciation analysis of W because of its low abundance of W in the samples. In particular for XAFS analysis, its relatively low abundance compared with coexisting other transition metals including chalcophile elements such as zinc (Zn) and nickel (Ni) which are enriched under sulfidic conditions makes it difficult to obtain W L_3 edge XAFS spectra due to the interferences from Zn and Ni in the XAFS analysis.

Usually, fluorescence mode XAFS (FL-XAFS) method using Ge-SSD is an established method for the speciation of trace level of elements in environmental samples. However, fluorescence X-rays from coexisting metals and scattered X-ray of incident X-ray often saturate the detector in terms of the upper counting limit (= ca. 10^5-10^6 photons/s), which finally prevents measurement of fluorescence X-ray from a target element. In the case of this study, the target element is W, while possible interfering metals are Ni and Zn, which are abundant in

the Cambrian black shales examined in this study. Previous studies attempted to reduce these interferences by applying the WD-XAFS method, which introduces a BCLA in front of the SSD (Takahashi et al., 2006; Kashiwabara et al., 2011). However, W concentrations in anoxic or sulfidic sediments are very low (around 10 mg/kg in this study), whereas those of interfering elements such as Ni and Zn concentrations are very high (3.2 wt.%/kg and 5830 mg/kg, respectively), which are more than 1000 and 200 times higher than that of W. It is difficult to apply bulk XAFS measurement for W in these samples. For this system, even bulk WD-XAFS method described in Chapter II is still not sensitive enough for the detection of W L_3 edge XAFS. Hence, micro scale XAFS (μ-XAFS) measurement is preferable for speciation of trace element in such samples, because we can find the area where the target element is concentrated using μ-XRF observation before the XAFS measurement. Moreover, μ-XRF-XAFS can clarify the host phase of trace element which controls the partition behavior of that element in the system. As a result, we can understand more detailed geochemical processes of the element.

In this study, we applied the WD-μ-XRF-XAFS analysis to the determination of chemical form of W preserved in highly sulfidic black shale. The sample studied here was collected from Niutitang Formation, Yangtze Platform, South China which was deposited in the early Cambrian. (Xu et al., 2013) Our speciation data can show new insights about the different geochemical process of Mo and W under various redox and sulfidic conditions.

III.2. Experimental method

III.2.1. Sample and reference materials

Early Cambrian sedimentary rocks were widely found on the Yangtze Platform of South China which has a Re-Os age of 541 ± 16 Myr (Fig. III-1; Xu et al., 2013; Mao et al., 2002).

The black shale studied here including polymetallic Ni-Mo-platinum group elements (PGE) - Au sulfide ore deposits are hosted in the lower section of black shale of the Niutitang Formation. The sample was collected in Dazhuliushui Ni–Mo–PGE–Au deposit in the western part of the Songlin dome, about 26 km from Zunyi City, Guizhou Province (27º41'N, 106º40'E; Fig. III-2). Neoproterozoic conglomerate of the Nantuo Formation, carbonaceous mudstone and dolomite of the Doushantuo Formation, dolomite of the Dengying Formation, and black shale of the Early Cambrian Niutitang Formation are exposed in the area (Fig. III-3). The sulfide marker bed includes high concentration of Mo (~7 wt%) with Ni and PGE, which was indicative of the enrichment of the trace metals scavenged from seawater (Lehman et al., 2007; Xu et al., 2013).
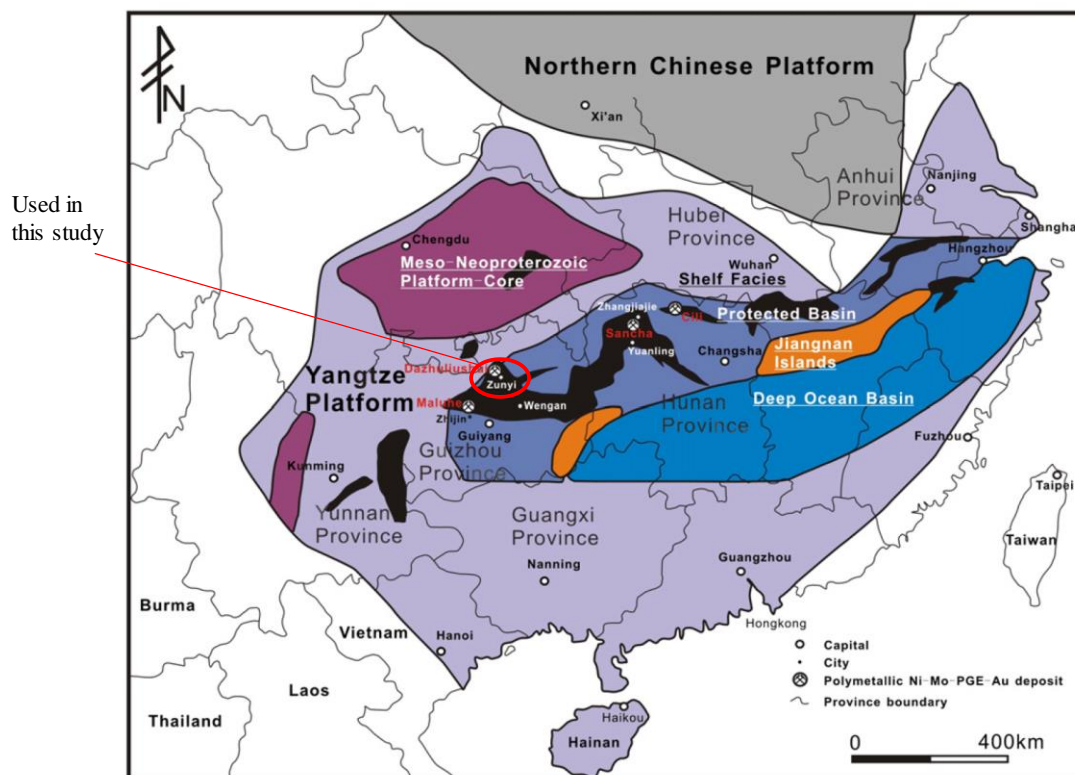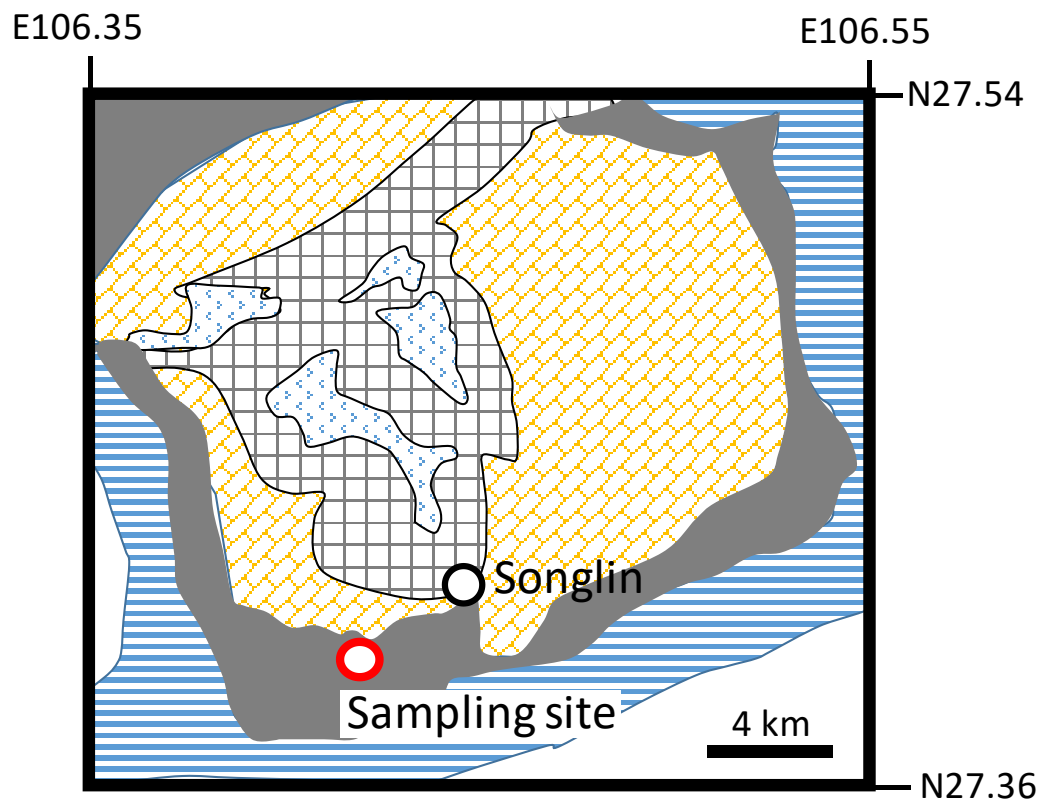
Fig. III-1 Sketch map showing locations of the Dazhuliushui, Muluhe, Sanchaand, and Cili polymetallic Ni–Mo–PGE–Au sulfide ore deposits, and depositional environments during the Neoproterozoic–Cambrian interval (Xu et al., 2013). Black areas indicate the exposed Early Cambrian black shale sequence of the Niutitang Formation (and equivalent strata) in South China. In this study, early Cambrian black shale collected in the Dazhuliushui Mine was examined.

Fig. III-2 Geological sketch map of the study area. Dazhuliushui Mine District near Zunyi, Guizhou Province (modified from Xu et al., 2013).

Fig. III-3 Stratigraphic column showing the Neoproterozoic–Early Cambrian sedimentary sequences of the study area (Xu et al., 2013). Dashed lines indicate stratigraphic localities of samples for dating. Radiometric ages with uncertainties are highlighted in red.
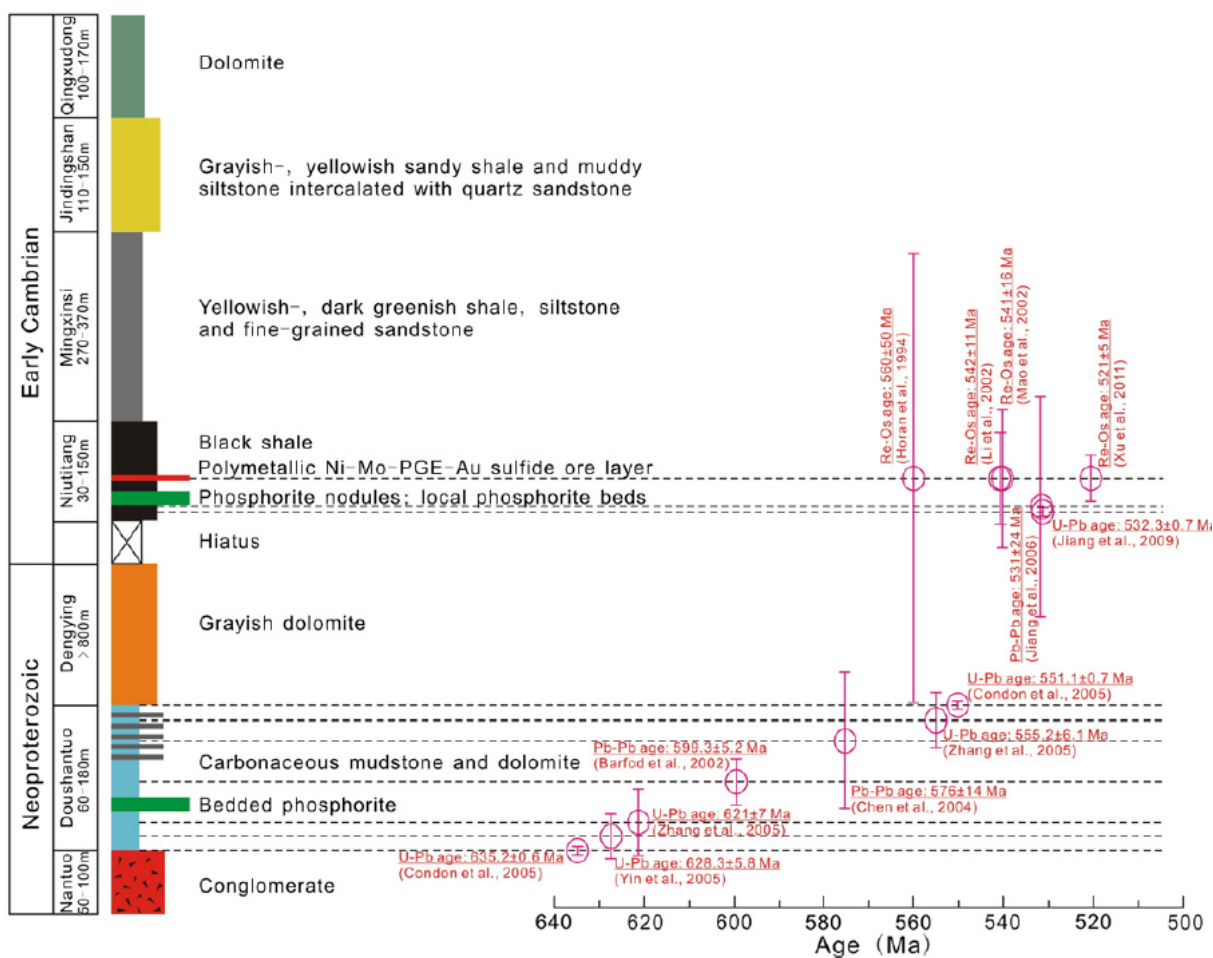
A thin section of the sample was prepared by polishing with silicon carbide abrasives and subsequently with diamond abrasives on a slide grass for the µ-XRF-XAFS analysis. Mineralogical composition of the sedimentary rock was pyrite, sphalerite, and millerite (Kao et al., 2001; Mao et al., 2002; Xu et al., 2013). The sample was observed using an optical microscope to confirm each mineral phase in the thin section (Fig. III-4).

Analyzed area   2 mm

Fig. III-4 Optical micrograph of black shale sample.

Concentrations of Fe, Mo, Ni, Zn, and other trace elements in the black shale were measured by ICP atomic emission spectrometry (AES; SII nanotechnology SPS3500, Japan) and ICP-MS (Agilent Technology 7700x, Tokyo, Japan) after digestion by multiple steps. Bulk sample was crushed, and powdered using an agate mortar. Powdered sample was digested by multiple steps. At first, powdered sample was digested by a mixed solution of concentrated HF and HNO_3 (3:1) for 48 h at 180 ºC on a hot plate. After 48 h, the digested solution was evaporated nearly to dryness, and the residue was redissolved by 6 M HCl, which was heated at 180 °C for 24 h. The solution was evaporated nearly to dryness and diluted with 1 M HCl. After the evaporation of the solution, the residual material was dissolved by 2 wt.% HNO_3 for ICP-MS measurement.

Some chemical compounds of Mo and W were purchased as reference materials of XAFS analysis. For XAFS analysis of Mo, Na_2MoO_4, MoO_3, MoO_2, $(NH_4)_2MoS_4$, and MoS_2 were obtained from Wako Pure Chemicals (Japan). In addition, MoS_3 was obtained from Alfa Aesar (USA.). For W analysis, Na_2WO_4, WO_3, WO_2, and WS_2 were obtained from Wako Pure Chemicals (Japan). In addition, $(NH_4)_2WS_4$ was obtained from Sigma-Aldrich (USA). These compounds were measured as pellet samples which were prepared from a mixture of each compound and powdered boron nitride (BN; Wako Pure Chem.) to adjust the concentrations of Mo or W and thickness of pellet for optimum X-ray absorption in the transmission mode. All the samples were packed into airtight polyethylene bags.

In this study, we also conducted laboratory experiments to examine the partition behavior of Mo and W from aqueous phase to pyrite and calcite, which are considered to control their distribution behaviors under euxinic condition in the absence of Fe and Mn (hydr)oxides.

Adsorption experiment of W onto pyrite was conducted by following procedures described

in Bostick et al. (2003) and Chapter II. Pyrite grains were refined by an agate mortar. The surface was washed by 0.1 M of HCl, 0.01 M of Na_2S, and Milli-Q water to remove oxidized species. Initial concentration of WO_4^{2-} or WS_4^{2-} in the aqueous phase was adjusted to 100 μM. Tungstate ion and WS_4^{2-} were prepared by dissolving $Na_2WO_4 \cdot 2H_2O$ (Wako, Japan) and $(NH_4)_2WS_4$ (Wako, Japan) in Milli-Q water, respectively. The solutions were mixed with the pyrite grains at pH 7.0 in the presence of 1 mM of Na_2S, while ionic strength was adjusted to 0.70. The solid-water ratio was fixed at 2.0 g/L.

Spontaneous precipitation experiment of calcite in the presence of Mo (MoO_4^{2-} or MoS_4^{2-}) and W (WO_4^{2-} or WS_4^{2-}) was conducted to examine coprecipitation of these ions into calcite by following procedures described in Tanaka et al. (2008). Calcite was precipitated by mixing 0.16 M $CaCl_2$ and 0.16 M $NaHCO_3$ solutions at 25 ℃. The pH of the both solutions were adjusted to 8.0 before mixing. The $NaHCO_3$ solution initially contained 50 μM MoO_4^{2-}, MoS_4^{2-}, WO_4^{2-}, or WS_4^{2-}. The concentration was determined to avoid the precipitation of $CaWO_4$. The calcite precipitated in the experiment was analyzed using XRD (Multi Flex, Rigaku, Japan). Adsorption of Mo and W onto calcite was also examined to confirm that the amount of adsorption of Mo or W species was negligible to determine the distribution of Mo or W to calcite by coprecipitation. To examine this factor, calcite sample which was not coprecipitated with Mo or W was prepared for the adsorption experiment.

These pyrite or calcite samples were separated from the aqueous phase by filtration using 0.20 μm membrane filter (cellulose acetate), and collected into airtight polyethylene bags for XAFS analysis. The filtrate was diluted by 2 wt.% HNO_3 for ICP-MS measurement. Tungsten concentration in the aqueous phase was measured to determine partition of W to the solid phase. The degree of partition of Mo or W to calcite was evaluated by the partition coefficient (K_d),

which is defined as

$$K_d = \frac{C_s}{C_w}$$

where C_s and C_w are the molar concentrations of Mo or W in the solid and aqueous phases, respectively.

III.2.2. μ-XRF-XAFS analysis

μ-XRF-XAFS analysis was conducted at BL37XU in SPring-8 (Hyogo, Japan). White X-ray generated from an undulator was monochromatized by a double crystal monochromator with a Si(111) plane. Beam size was 1.9 (horizontal: H) × 0.8 (vertical: V) μm^2 by a Kirkpatrick-Baez (K-B) mirror system (Terada et al., 2010). To obtain map in larger areas, apparent beam size can be enlarged by adjusting the distance between the sample and K-B mirror, by which I sometimes obtained map using a larger X-ray beam of 33 (H) × 24 (V) μm^2. A two-dimensional (2D position) μ-XRF image was obtained by measuring the XRF using 4-element Silicon Drift Detector (SDD) with an X-Y axis stepping motor

Fig. III-5 Experimental set up of μ-XRF-WD-XAFS method in BL37XU at SPring-8

driven stage. The BCLA (DCA-0950, Oxford Danfysik; Takahashi et al., 2006; Kashiwabara et al., 2010) was placed in front of the detector to reduce the interferences of the Ni Kβ (8.265 keV) and Zn Kα (8.632 keV) lines, as well as the scattering X-ray from the incident X-ray on the target X-ray, W Lα line (8.398 keV). The experimental set up in the beamline was shown in

Fig. III-5.

Molybdenum and W images were obtained by collecting Mo Kα (17.446 keV) and W Lα (8.398 keV), respectively. To confirm the distribution of major sulfide mineral compositions, Fe, Zn, and Ni images were also obtained by collecting Fe Kα (6.400 keV), Zn Kα (8.632 keV), and Ni Kα (7.473 keV), respectively.

To obtain W mapping by detection of W Lα line, we performed the difference mapping method. First, the W map were obtained at the pre- and post-edge energies around the W L_3 edge (10.095 and 10.195 keV, respectively). Subsequently, the map plotting the signal (counts/sec) in the W Lα line window obtained at the pre-edge energy was subtracted from that at the post-edge energy to remove the effect of interference X-rays such as Zn Kα and Ni Kβ (8.265 keV).

Micro scale speciation of W and Mo were determined by measuring Mo K edge and W L_3 edge XAFS spectra. The reference materials were measured in transmission mode by monitoring the incident intensity (I_0) and intensity after transmission (I) of the samples in the ionization chamber. The spectra for samples were obtained in fluorescence mode with the 4-element SDD.

Radiation damage and alteration with oxidation by ambient condition were not observed during the data acquisition, because multiple scans provided identical spectra. The XANES was analyzed by using the REX2000 software (Rigaku, Tokyo, Japan). The chemical species of the elements in the samples were simulated by linear combination fitting (LCF) of the XANES spectra to the reference materials. To assess the accuracy of the XANES fitting results, the R factor, which is calculated by the sum of squares of the difference between the observed and fitted data at each point, was defined as follows:

$$R = \frac{\sum (I_s(E) - I_{cal}(E))^2}{\sum I_s(E)^2}$$

where I_s and I_{cal} are the normalized absorption spectra of the solid samples and calculated values, respectively. All fitting results were obtained when the R factor was minimal in the fitting procedure.

In addition, Mo K edge EXAFS spectra were measured at BL01B1 in SPring-8. EXAFS analysis was performed using REX2000 ver. 2.5 (Rigaku Co.) and FEFF7 (Zabinsky et al., 1995). The x(k) function was extracted from the raw spectrum by a spline smoothing method, while E_0 was set at the edge inflection point.

A radial structural functions (RSFs) were obtained by Fourier transforming of the k^3 - weighted x(k) functions from k to r space at the range of 3.0–13.0 Å^{-1}. The inversely Fourier filtered $k^3 x(k)$ were analyzed with a usual curve-fitting method. The theoretical backscattering amplitudes and phase-shift functions employed in this fitting procedure were obtained using FEFF7. In this calculation, the backscattering amplitudes and phase-shift functions for Mo–O, Mo–S, and Mo–S were extracted from the structure of Na_2MoO_4, $(NH_4)_2MoS_4$, and MoS_2, respectively.

III.3. Results and Discussion

III.3.1. WD-µ-XRF analysis

Tungsten L_3 edge (10.200 keV) XAFS spectrum is often measured for the speciation of W, because high photon flux can be obtained at the energy region around 10 keV with a Si(111) plane which is often used for normal XAFS measurement in various synchrotron radiation facilities. For W L_3 edge XAFS measurement with fluorescence XAFS method, it is needed to measure W Lα line (8.398 keV). However, Kα or Kβ lines of some transition metals such as Ni, Cu, and Zn are present in the energy region close to that of W Lα line. Concentrations of these elements are normally much higher than that of W in natural samples, whereas quantum yield is generally larger for K lines compared with L lines. Therefore, these elements often prevent to measure W Lα line using SSD due to the increase of the background signal as also described in Chapter II. Thus, WD-XAFS method can improve the signal/ background (S/B) ratio to measure the spectra so that we can get high quality of XAFS data from natural samples. Average composition of Chinese sulfidic black shale examined here contained high amount of Zn and Ni (5800 mg/kg and 3.2 wt.%, respectively), while the sample contained 30 mg/kg of W (Table III-1). The ratios of W/Zn (=0.005) and W/Ni (=0.0009) for bulk sample were much lower than previous speciation analysis using WD-XAFS technique (e.g. the ratios were 0.034 and 0.014 in Kashiwabara et

Table III-1 Concentrations of major and trace elements in the black shale sample in this study.

Element	value	unit
C_{org}*	12	wt.%
V	980	ppm
Cr	100	ppm
Mn	430	ppm
Fe	12.3	wt.%
Ni	3.2	wt.%
Cu	1800	ppm
Zn	5800	ppm
As	13000	ppm
Mo	6.1	wt.%
Ba	2300	ppm
W	30	ppm
Pb	89	ppm
U	120	ppm

*C_{org}: values reported in Mao et al. (2002) for the horizon identical to this study in the lower Cambrian black shale.

71

al., 2013).

To get high quality XAFS spectra for the speciation analysis, I first performed μ-XRF mapping with employing BCLA, and confirmed the hot spot of W, or the point with high signal of W Lα emission. The sample mainly consists of large size pyrite particles and millerite (Fig. III-6). The black-colored organic carbon cemented the whole rock. In the thin section of the sample, I focused the area representing the sample to study these minerals and organic materials based on the observations by optical microscope and SEM (Fig. III-6). The area highlighted here contained large size pyrite particles (100-200 μm), and Ni-enriched layer (possibly present us millerite), and organic carbon containing Ca, previously reported as Ni-rich MoSC phase, and aluminosilicate particles. Here, MoSC is the amorphous phase reported as an important Mo carrier found as mm-sized ellipsoidal aggregates or fine laminated materials (Kao et al., 2001; Mao et al., 2002) with approximate chemical composition of $(Mo,Fe,Ni)(S,As)_2C_7$ (Kao et al., 2011). Figure III-7 shows the optical image (a) and μ-XRF images of W Lα (b), Fe Kα (c), Ni Kα (d), Zn Kα (e), and difference map of W Lα with WD mode (f) in the analyzed area. The result of Mo mapping was also shown in Fig. III-7(g). In the sample, some mineral phases which are considered to be main components of sulfide minerals in the sample were observed. Various sizes of FeS_2 particles were found by microscopic and μ-XRF observations. Nickel sulfide (NiS) and zinc sulfide (ZnS) particles were also frequently found. Molybdenum and Nienriched gray-colored material was also found, which is considered to be a MoSC phase. The sapropel material consisted of organic matter and fine grained minerals such as carbonate and phosphate which occupied the interlayer of sulfide mineral particles. The organic matter was presumably derived from in-situ sapropelized products of planktonic and benthic organisms, oncolite-like algal/bacterial remnants, and oil-derived migrabitumen, which has a high thermal

maturity corresponding to the semi-anthracite to anthracite stage of coalification (Křibek et al., 2007).

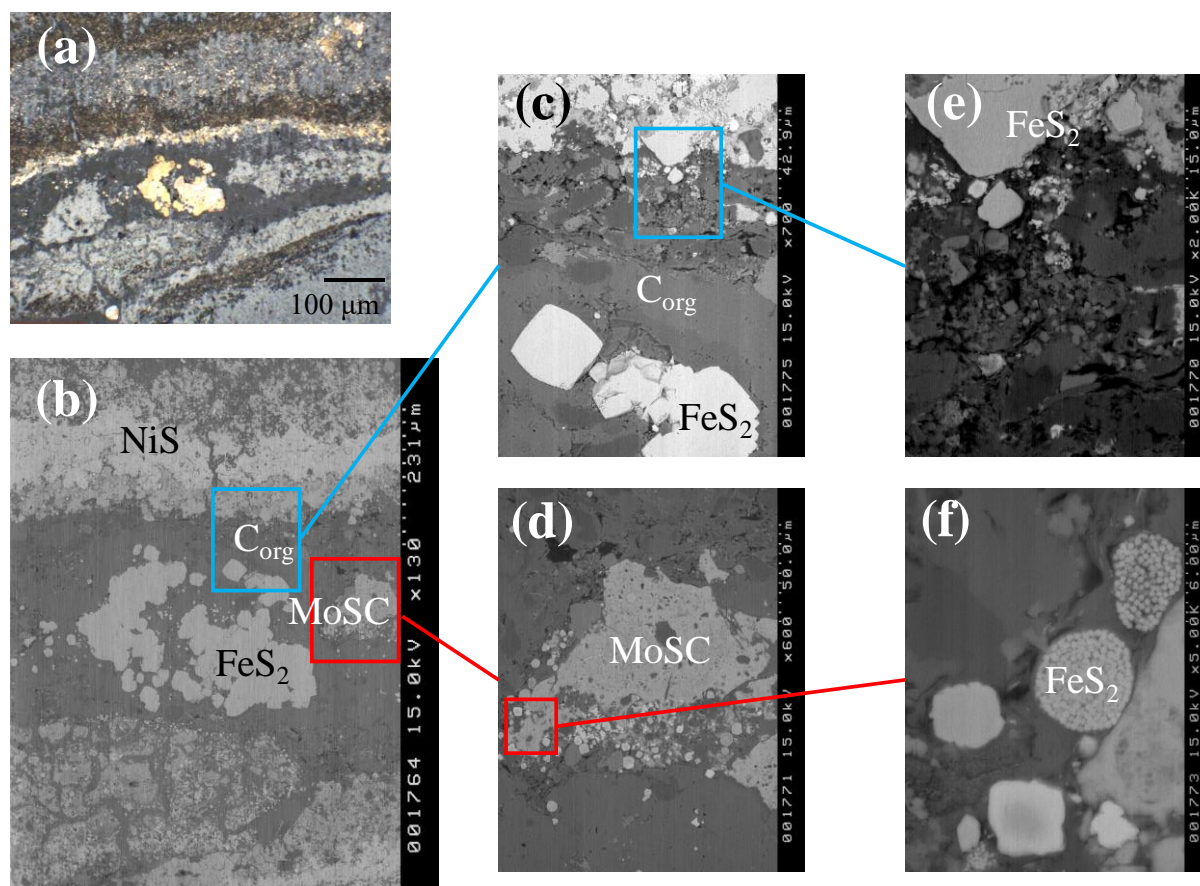Fig. III-6 Optical micrographs and BSE images of natural black shale sample. (a) Optical micrograph; (b)-(f) BSE images; (b) whole area analyzed in this study; (c) local area around pyrite particle and organic carbon and aluminosilicate phase; (d) local area around MoSC phase; (e) enlarged area around organic carbon and aluminosilicate phase; (f) enlarged area of pyrite framboids near the edge of MoSC phase.
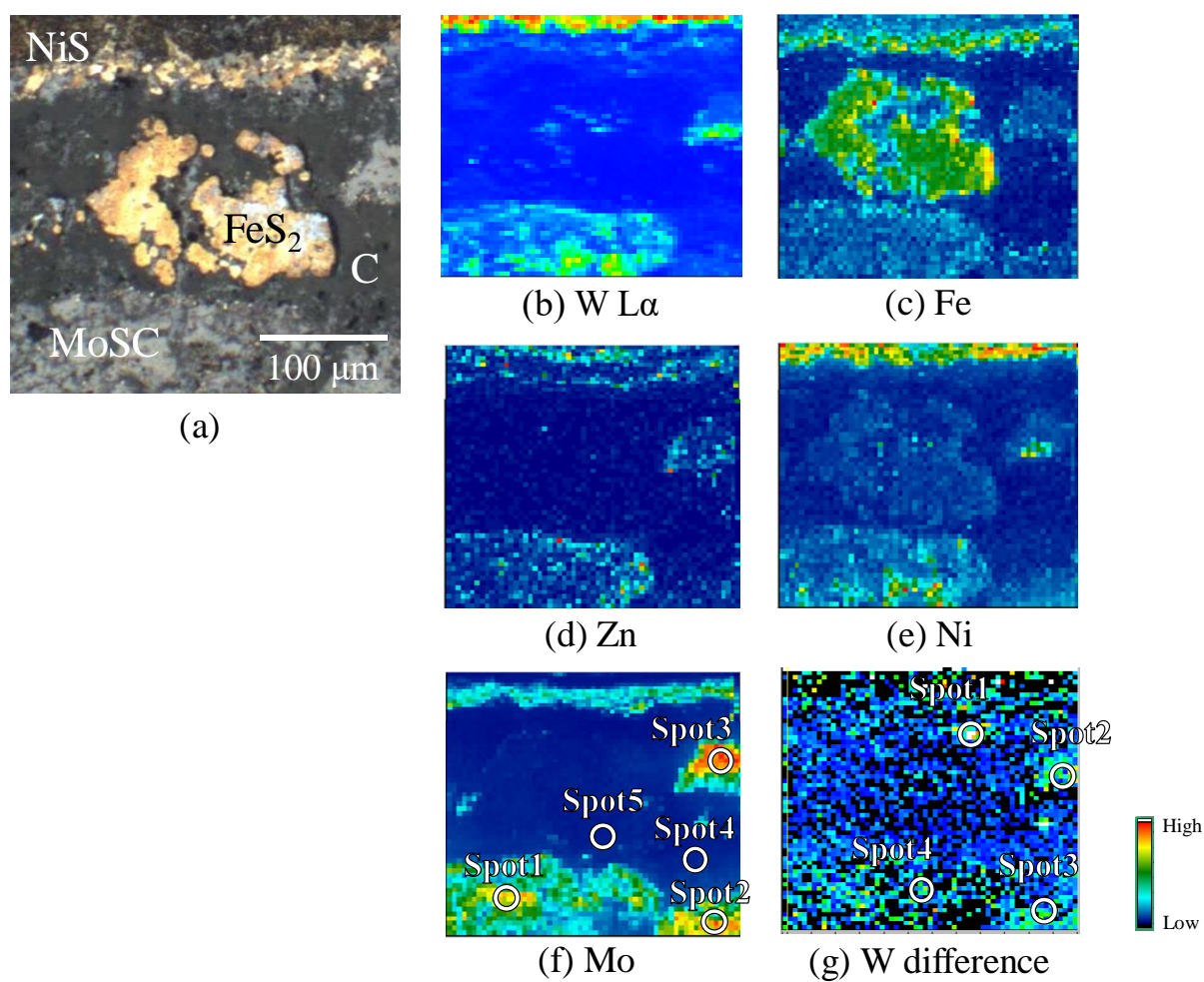
Fig. III-7 Optical micrograph and μ-XRF images of natural black shale. (a) Optical micrograph. (b)-(g): μ-XRF images of (b) W Lα, (c) Fe Kα, (d) Zn Kα, (e) Ni Kα, (f) Mo Kα, and (g) W difference map.

In the mapping data, W distribution is apparently well correlated with Ni. However, it is possible that interference by Ni Kβ apparently affected the W distribution even in using the BCLA which has a range of energy resolution of ca. 100 eV, because of very intense signal derived from Ni compared with that of W. The XRF spectra of the sample obtained at pre-edge (10.095 keV) and post-edge (10.195 keV) of the W L_3 absorption edge of are shown in Fig. III-8. Without the BCLA, the W Lα peak was interfered by the tails of the Ni Kβ and the Zn Kα emissions (Fig. III-8a and b). The interference X-rays were also observed even in using the crystal analyzer, BCLA (Fig. III-8c), which suggests that the obtained W Lα map was still affected by these interferences. However, I could observe increase of the W signal by the excitation of W at 10.195 keV compared with the XRF spectra obtained at pre-edge energy (10.095 keV) of W L_3 edge. Figure III-8d shows the subtracted XRF spectra at the energy of 10.195 keV (post-edge) by that of the energy of 10.095 keV (pre-edge), by which I could extract W signal increased by the excitation at the post-edge. The difference map obtained by the subtracted XRF spectra showed different distribution of W compared with those of Ni or Zn map, suggesting that the difference map shows the true W distribution (Fig. III-7f). Thus, I concluded that the difference map method combined with WD technique can be a powerful tool to determine the distribution of trace element coexisting with other abundant transition metals in natural samples.

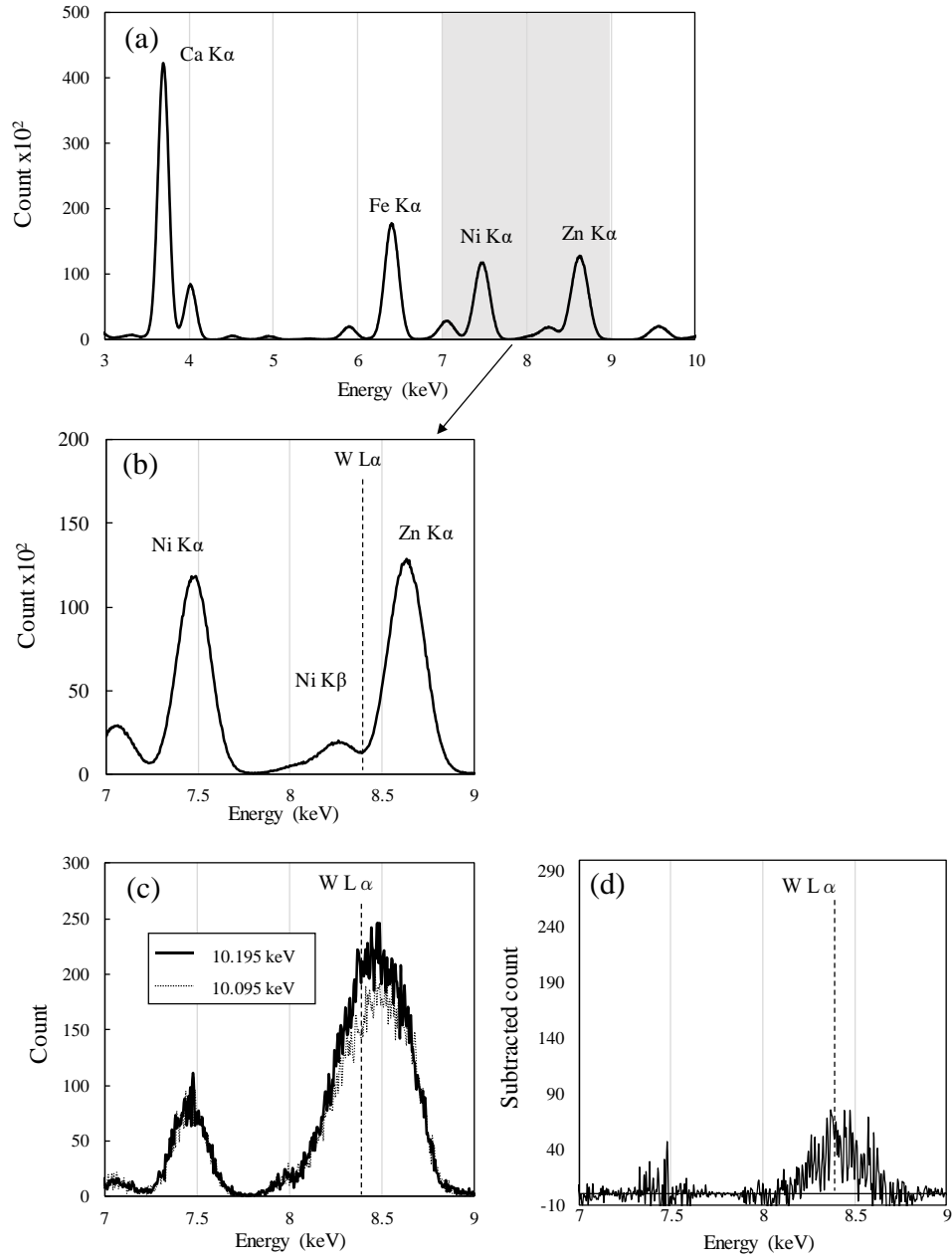Fig. III-8 XRF spectra of natural black shale at the spot 1 shown in Fig. III-7(g). (a): XRF spectra (3.0-10.0 keV) without BCLA. (b): Narrower energy region including Ni Kα, Kβ, W Lα, and Zn Kα without BCLA. (c): Same energy range with (b) with BCLA. Solid line shows obtained spectra by incident X-ray at 10.195 keV, while dotted line shows that at 10.095 keV. (d): Subtracted XRF spectra from 10.195 keV by 10.095 keV with BCLA.

III.3.2. Speciation of W in euxinic sediment

Difference map of W Lα showed that three hot spots of W were found in the sample. We performed WD-μ-XAFS analysis at each point. Figure III-9 showed W L_3 edge XANES spectra at spot 1 without background subtraction. The raw data showed high background noise level in the case of the spectra without BCLA due to the intense interferences of Ni and Zn, which leads to poor quality of the spectrum (Fig. III-9a). In contrast, efficient removal of the background was found by the introduction of BCLA (Fig. III-9b and III-9c) because of the decrease of interferences from Ni and Zn and reduction of total XRF signal entering the detector (Fig. III-8), which enables us to measure high-quality spectrum. Although, the total XRF entering the detector was decreased by the introduction of BCLA, the summation of the improved spectra in terms of high S/B ratio (but lower signal intensity) leads to the high quality spectra to determine the chemical species of W in natural sample (Fig. III-9c: the summation of three scans measured for ca. 90 min for each scan). By the combination of WD method to decrease the background noise level and μ-XRF-XAFS analysis to identify the hot spot of the trace element, it was possible to determine the chemical species of trace level of W in natural sample. Otherwise, it is impossible to obtain the spectrum with conventional XAFS measurement.
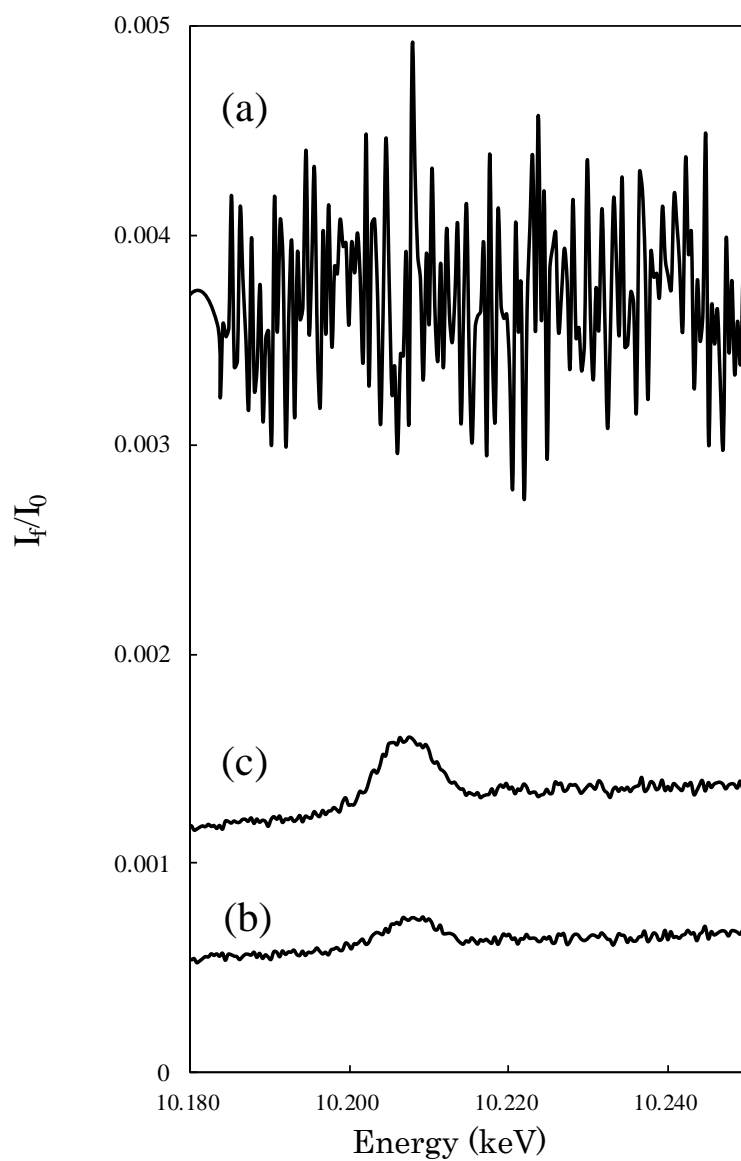
Fig. III-9 Tungsten L_3 edge XANES spectra of W in natural black shale measured at spot 1 in Fig. III-7(g) before background subtraction. (a) without BCLA. (b) with BCLA in single measurement. (c) summation of 3 scans using BCLA.

The normalized W L_3 edge XANES spectra for the sample were shown in Fig. III-10. I applied μ-XAFS analysis for four points in the analyzed area of the mapping, where the W signals were higher than the other areas. Na_2WO_4 and $(NH_4)_2WS_4$ are the reference materials representing the oxygen or sulfur-coordinated species, where the spectrum of $(NH_4)_2WS_4$ has a peak at lower energy than that of Na_2WO_4. Thus, we can identify the coordinated element to W in the sample by comparing the peak position. In the sample, both oxygen and sulfur-coordinated species were found at different analyzed areas. Sulfur-coordinated species were found in the MoSC phase which is considered to enrich some trace metals such as PGE (Xu et al., 2013). On the other hand, oxygen-coordinated species was found in the matrix phase consisting of organic carbon or fine grained minerals without significant correlations with other metals measured in our analysis. The difference of distribution and coordinated element of W suggests that W has several burial pathways for its incorporation into euxinic sediments because of the low adsorption behavior of W to sulfide mineral in contrast to that of Mo under reductive condition as described in Chapter II. Other host phases should be considered for W under the reductive condition in the absence of Fe and Mn (hydr)oxides which are dominant host phases of W in oxic environment.

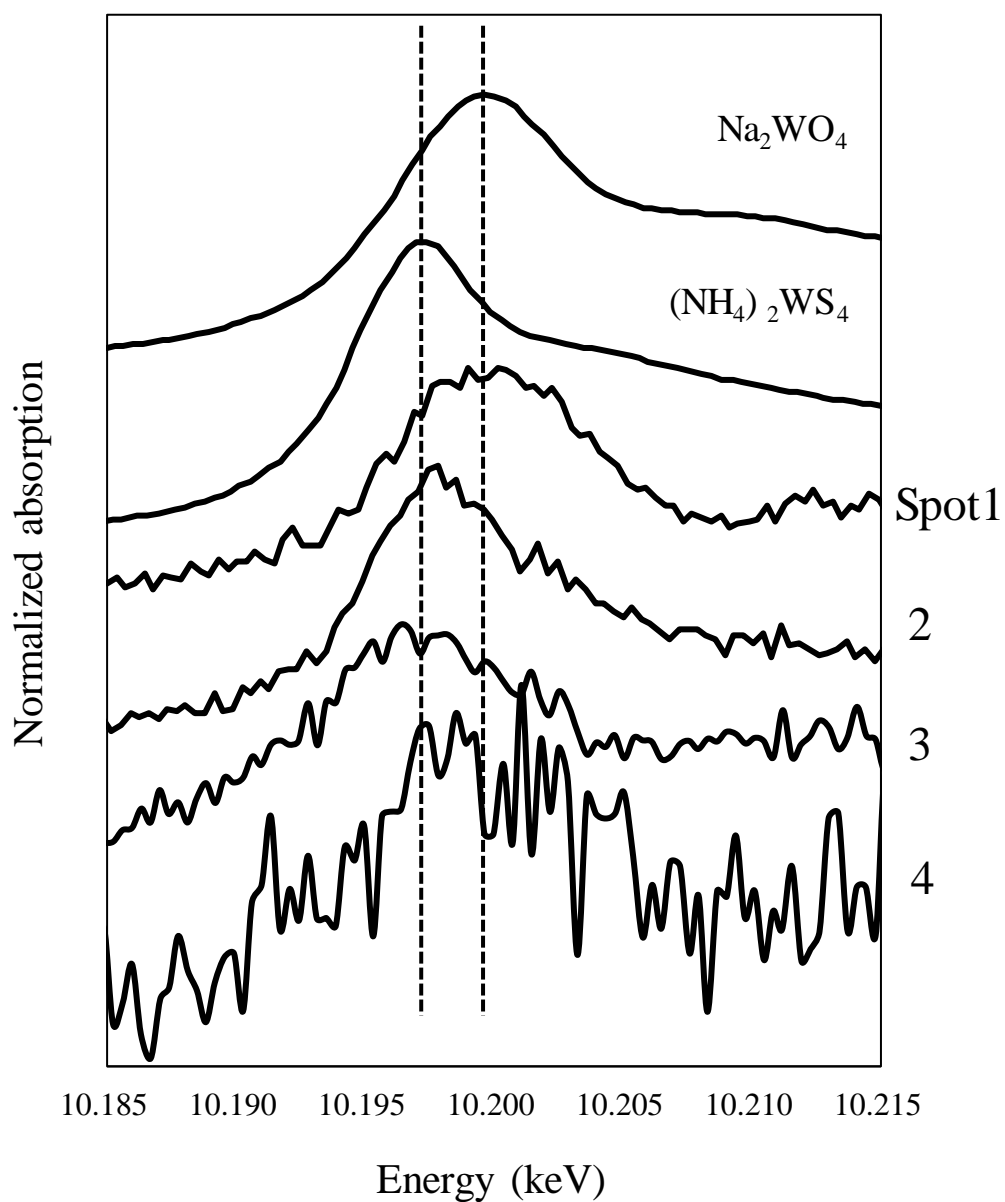Fig. III-10. Normalized W L_3 edge XANES spectra of W in natural black shale sample in this study. The spectra of Na_2WO_4 and $(NH_4)_2WS_4$ were measured by transmission mode. The spectra of W in spots 1-4 were measured by fluorescence mode with BCLA.

The partition of W to sediment in seawater under sulfidic condition is not well understood. The present results in Chapter II and a former study about natural observation of W behavior (Mohajerin et al., 2016) suggested that the distribution coefficient (K_d) of W under sulfidic condition is smaller than that under oxic condition, because of difference of the mineralogical composition of solid phase and the dissolved species of W. To identify the W species and its host phases in black shale deposited under euxinic condition, I experimentally examined two minerals that can host W, while W species in each phase was determined by XANES analysis. Pyrite and calcite were selected as representative host phases of W in the black shale. Tungsten L_3 edge XANES spectra for W adsorbed on the pyrite were shown in Fig. III-11. In the adsorption experiment, both WO_4^{2-} and WS_4^{2-} were assumed as initial dissolved species of W. As a result, it was found that the adsorbed species of W on pyrite depends on its dissolved species. When W was dissolved initially as WO_4^{2-} in the aqueous phase, W was adsorbed as oxygen-coordinated species. However, W was adsorbed as sulfur coordinated species on pyrite when WS_4^{2-} was a starting species in the aqueous phase. The WS_4^{2-} and other thiotungstate species could be formed in sulfidic water when the H_2S was very high (>100 µM; Mohajerin et al., 2014). Therefore, sulfur-coordinated species in solid phase should be observed only under highly sulfidic condition.

On the other hand, different incorporation process was observed when W was distributed to calcite. In the spontaneous precipitation experiments of calcite, I considered that W (and Mo) distribution to calcite is controlled by co-precipitation process rather than adsorption process, because the calcite is precipitated from seawater with incorporating other trace elements, and the composition of trace elements in calcite more or less preserved chemical compositions of seawater at the time of precipitation of calcite. However, it is possible that W spontaneously

form scheelite ($CaWO_4$) when the W concentration in the aqueous phase was above 500 μM in the present experiments. Figure III-12 shows the XRD patterns of the precipitates formed in the experiments with various initial W concentrations. One sample was produced at lower W concentration, which is under saturation in terms of scheelite. In the sample, only calcite was identified in the XRD pattern without any signatures of scheelite and other carbonate minerals. On the other hand, another sample with higher W concentration oversaturated with scheelite contained scheelite and aragonite in our samples. Under that condition, spontaneous scheelite deposition occurred and aragonite partially formed during calcite precipitation by incorporating a large amount of W.

In the crystal structure of calcite, it is expected that W substitutes with CO_3^{2-} as WO_4^{2-}. However, the local chemical environment is not clear for W incorporated in calcite. From the XANES analysis, however, it was clear that oxygen-coordinated species of W was the dominant form in calcite (Fig. III-13). Even when the initial dissolved species of W was WS_4^{2-}, only oxygen coordinated species was observed in calcite, implying that WS_4^{2-} was not stable in the structure of calcite, and ligand exchange occurred during the coprecipitation process.

These experimental results were well consistent with natural sample observation. From these results, our natural sample data suggests that the W was incorporated to the sediment under highly sulfidic condition enough to form WS_4^{2-} species in seawater. However, we also found the oxygen-coordinated species in the sample. The species could be the W incorporated in carbonate minerals such as calcite. Although the host mineral which oxygen-coordinated species was found was uncertain, strong signal of Ca Kα at 4.09 keV in the XRF spectra in that area (Fig. III-8a).
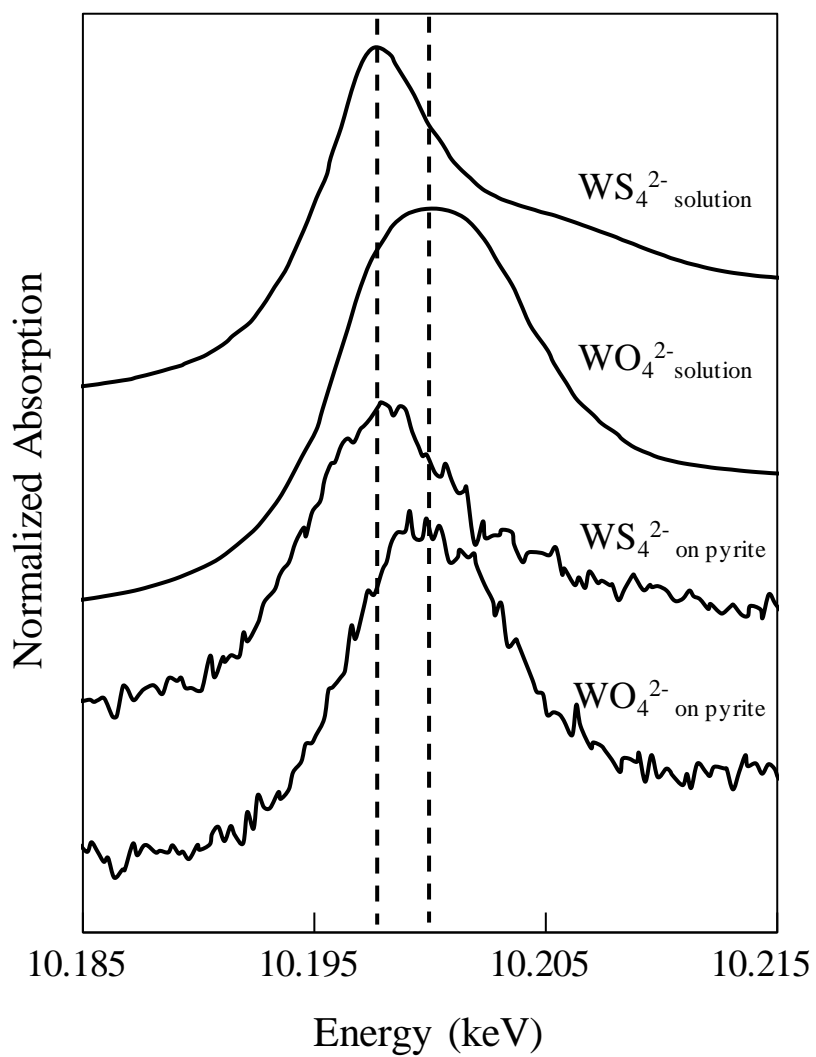
Fig. III-11. Normalized W L_3 edge XANES spectra of W adsorbed on pyrite prepared in laboratory experiments.
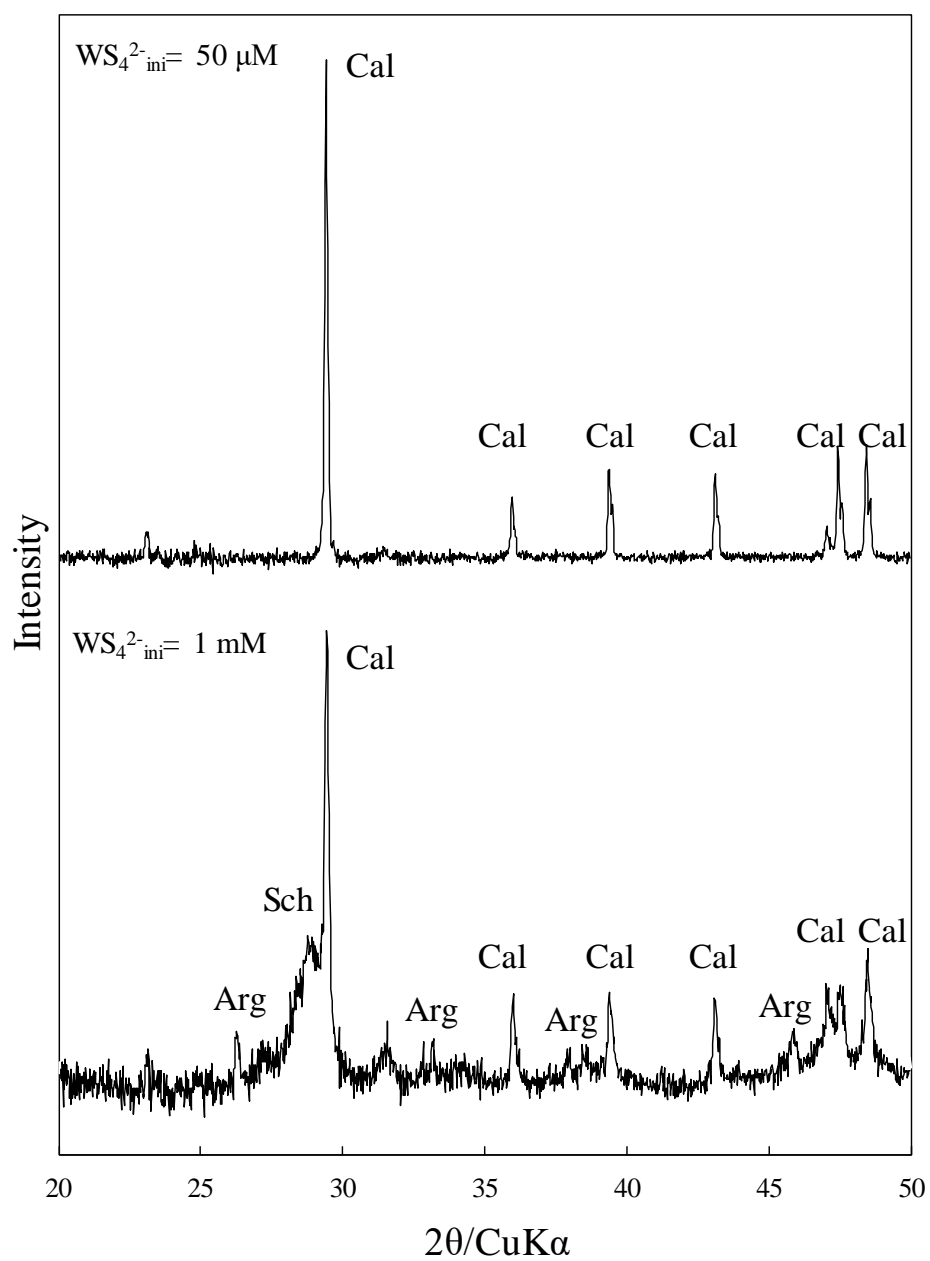
Fig. III-12 X-ray difraction patterns of precipitated calcite to survey presence of other carbonate minerals. Cal: calcite; Arg: aragonite; Sch: scheelite.
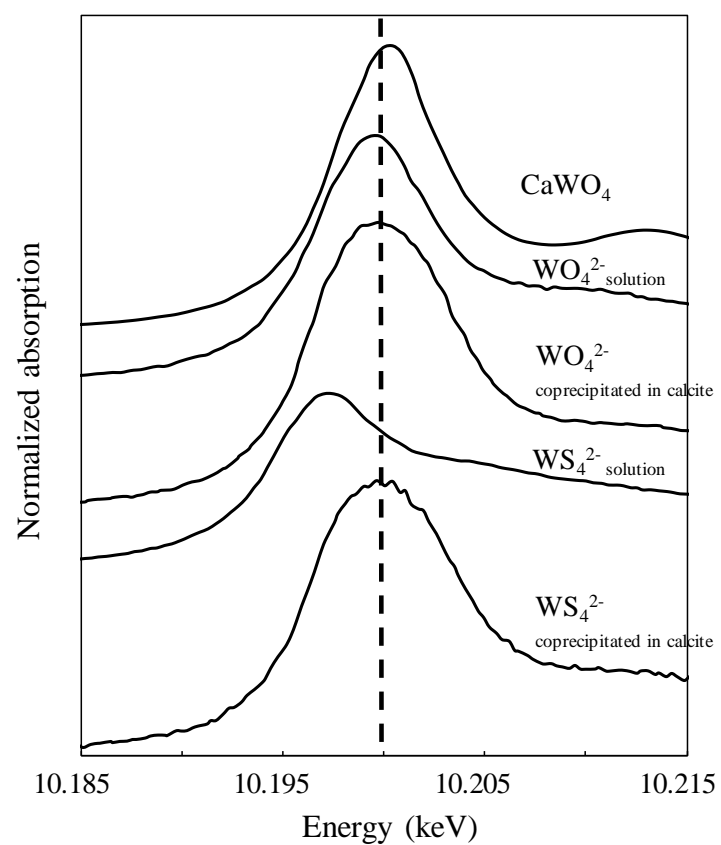
Fig. III-13. Normalized W L_3 edge XANES spectra of W coprecipitated with calcite prepared in laboratory experiments.

III.3.3. Comparison of geochemical behaviors of W and Mo in Early Cambrian black shale

Numerous studies about enrichment of Mo in oxygen-deficient marine sediments were reported, and the enrichment mechanism has been discussed (Bertine and Turekian, 1973; Pilipshuk and Volkov, 1974, Brumsack and Gieskes, 1983; Helz et al., 1996; Erickson and Helz, 2000; Chappaz et al., 2014). Concentration and isotope analyses of Mo in Early Cambrian black shale suggested that H_2S-rich bottom seawater upwelled to surface ocean and Mo removal from seawater occurred globally in Precambrian/Cambrian (Pc/C) boundary (Wille et al., 2008). Under this condition, Mo would form MoS_4^{2-}, which was strongly adsorbed to sulfidic particles or organic matters (Helz et al., 2011). Although the major process of the initial adsorbed species of Mo to the solid phase is not clear, adsorption of Mo(VI)-S species should be the first process, and subsequent formation and preservation of Mo(IV)-S species were suggested by XAFS analysis of modern and ancient sulfidic sediments (Helz et al., 1996; Dahl et al., 2013). In our sample, microscopic and μ-XRF observation indicated that the main Mo phase was organic matter-rich MoSC phase defined by Kao et al. (2001), where many trace metals were enriched as sulfides (Fig. III-7f). Figures III-14, III-15, and III-16 show the μ-XANES, EXAFS spectra, and radial structural functions (RSFs) of Mo K edge EXAFS in the analyzed area. In Table III-2 showing structural parameters obtained by EXAFS analysis, CN means the coordination number which was kept invariable in the refinement of the EXAFS fitting procedure. The R means the interatomic distance between Mo and adjacent atoms. The ΔE_0 and σ^2 mean E_0 shift and Debye–Waller factor, respectively. In the curve fitting, R, E_0, and σ^2 were varied. To compare the chemical form of Mo in each phase, we chose 5 spots in analyzed area (Fig. III-7(f)). Both XANES and EXAFS spectra suggested that Mo species in the spots were almost identical and the chemical species was Mo(IV)-S species very similar to molybdenite (MoS_2).

Although the reduced form of Mo would be formed in diagenetic alteration, the chemical process is not clear. Molybdenite is known as a hydrothermal mineral which was crystalized as a result of thermal reactions of Mo in the presence of H_2S or elemental sulfur (Donald et al., 1995). However, it is considered that the sample in this study enriched Mo from seawater by scavenging and did not experience intense hydrothermal alteration (Donald et al., 1995). In addition, RSF of Mo suggested that the coordination number derived from Mo was smaller than that of molybdenite (Fig. III-16 and Table III-2), which suggests that reduced Mo-S species was formed during other diagenetic reactions without intense hydrothermal alteration. The organic matter-rich MoSC phase include amorphous MoS_2 called jordisite which has smaller coordination number of Mo-Mo distance (Helz et al., 1996). It has been indicated that the formation process of jordisite include reactions with organic matter. Therefore, it is possible that organic matter could reduce Mo(VI) initially adsorbed on the sediment to Mo(IV) under sulfidic condition to form the Mo-enriched part in the black shale.

87

Table III-2. Structural parameters for the Mo species in the natural black shale calculated from EXAFS spectra (Figs. III-15 and III-16).

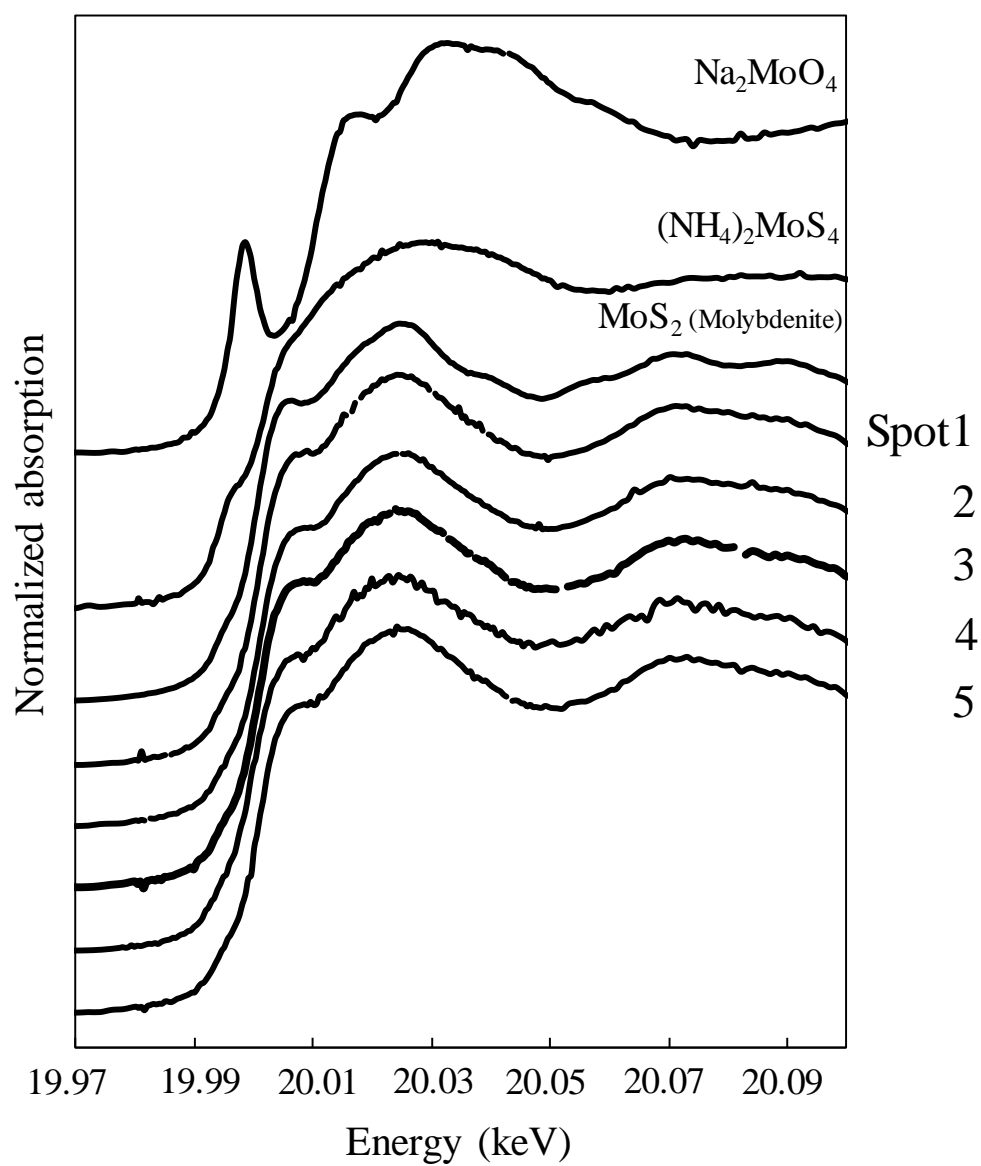| Sample	Shell	CN	R(Å)	ΔE_0 (eV)	σ^2(Å^2)
MoS$_2$ (molybdenite)	Mo-S	5.9	2.41	3.2	0.03
	Mo-Mo	6.0	3.14		
Spot 1	Mo-S	5.8	2.41	4.0	0.05
	Mo-Mo	4.8	3.11		
Spot 2	Mo-S	5.7	2.42	3.7	0.05
	Mo-Mo	4.4	3.13		
Spot 3	Mo-S	5.9	2.40	3.8	0.04
	Mo-Mo	4.6	3.13		
Spot4	Mo-S	5.8	2.41	5.6	0.05
	Mo-Mo	4.8	3.14		
Spot 5	Mo-S	5.6	2.41	4.5	0.06
	Mo-Mo	4.4	3.12		

Fig. III-14. Normalized Mo *K* edge XANES spectra of natural black shale. Position of each point was shown in Fig. III-7(f).

Fig. III-15. Molybdenum K edge EXAFS spectra of k^3-weighted $x(k)$ spectra. Position of each spot was shown in Fig. III-7(f). (a) Na_2MoO_4. (b) $(NH_4)_2MoS_4$. (c) MoS_2. (d)-(h) spots 1-5 in natural black shale.
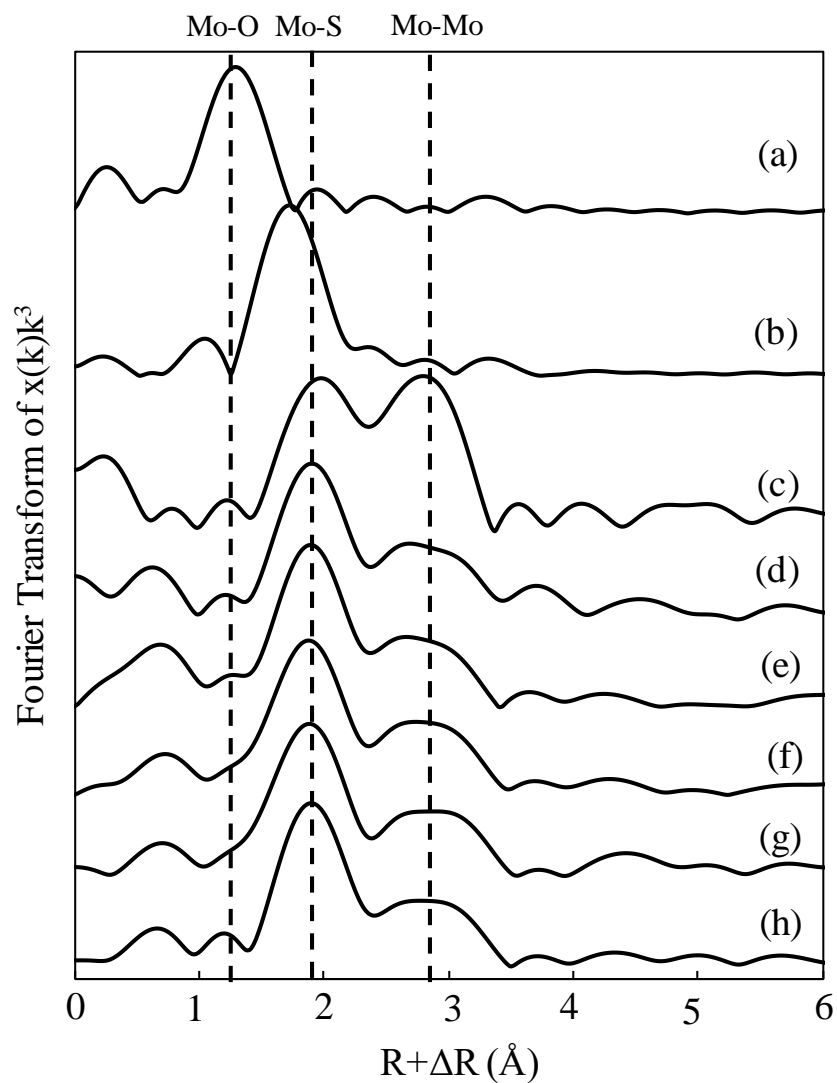
Fig. III-16. Molybdenum *K* edge EXAFS spectra of RSF of Fig. III-15. Position of each spot was shown in Fig. III-7(f). (a) Na_2MoO_4. (b) $(NH_4)_2MoS_4$. (c) MoS_2. (d)-(h) spots 1-5 in natural black shale.

On the other hand, enrichment of W in the sample was not large compared with Mo. This is caused by smaller partition of W to sulfide minerals than Mo, which was also discussed in Chapter II. In the Pc/C boundary, the circulation of Mo was transiently changed by the gradual increase of H_2S concentration globally from bottom seawater to surface seawater (Wille et al., 2008). In the period, dissolved concentration of Mo would be decreased by its incorporation into sulfidic sediment, and the change of ocean circulation led to Early Cambrian animal radiation. However, it is possible that W concentration in seawater would not change compared with Mo due to its much smaller reactivity with H_2S, suggesting that the ratio of Mo/W in seawater was not identical to that in modern seawater. In modern seawater, Mo/W ratio is 1800 as molar ratio (Sohrin et al., 1987). If we could confirm that the Mo/W ratio in sulfidic seawater was much lower than that in modern seawater, Mo/W ratio could be a new redox indicator of redox environment. To examine the Mo/W ratio in seawater at Pc/C boundary, incorporations of Mo and W into carbonate mineral found in the sample were studied. Carbonate such as calcite could preserve the water composition of the element at the time of deposition of the carbonate minerals (Tanaka et al., 2006). In our sample, we found carbonate phases where strong Ca signal was observed (Fig. III-7g, spot 1; III-8a). In the spot, strontium signal in the XRF mapping was also high compared with the adjacent areas, which also suggests that the mineral is carbonate phase. Here, I assumed that the carbonate coprecipitated with Mo and W within the precipitates. The replacement of CO_3^{2-} by WO_4^{2-} in the calcite structure during coprecipitation was confirmed by W L_3 edge EXAFS for the sample obtained by the laboratory experiments (Fig. III-17). Thus, we measured the signal ratio of Mo/W in that phase calculated as intensity ratio of Mo Kα and W Lα emissions in the μ-XRF analysis. However, coprecipitation behavior of Mo and W could be different. Thus, we determined distribution coefficients (K_d) of MoS_4^{2-} and

WS_4^{2-} assuming that these species were coprecipitated with calcite. The experiments were conducted following the method as described above. The K_d was calculated assuming that initial dissolved species of Mo and W were MoS_4^{2-} and WS_4^{2-}, respectively, to confirm actual partitions of Mo and W to calcite under highly sulfidic condition. I showed the results of coprecipitation experiments for these elements in Fig. III-18. The results suggested that the coprecipitated concentrations of Mo and W increased linearly with the increase in their concentrations in the aqueous phase, where K_d values of Mo and W were about 0.5 and 100, respectively. Thus, I applied the K_d values obtained in the experiment to estimation of the Mo and W composition in seawater from natural carbonates. In the calculation, concentrations of Mo and W adsorbed on carbonate surface were negligible, since their adsorbed concentrations were much smaller than those of coprecipitated fraction (Fig. III-18). The calculated Mo/W ratio in Early Cambrian seawater was about 1. By comparing the calculated Mo/W ratio in sulfidic seawater with modern oxic seawater (= 1800), it is suggested that the ratio could be decreased dramatically with development of oxic condition during the evolution of the atmosphere.
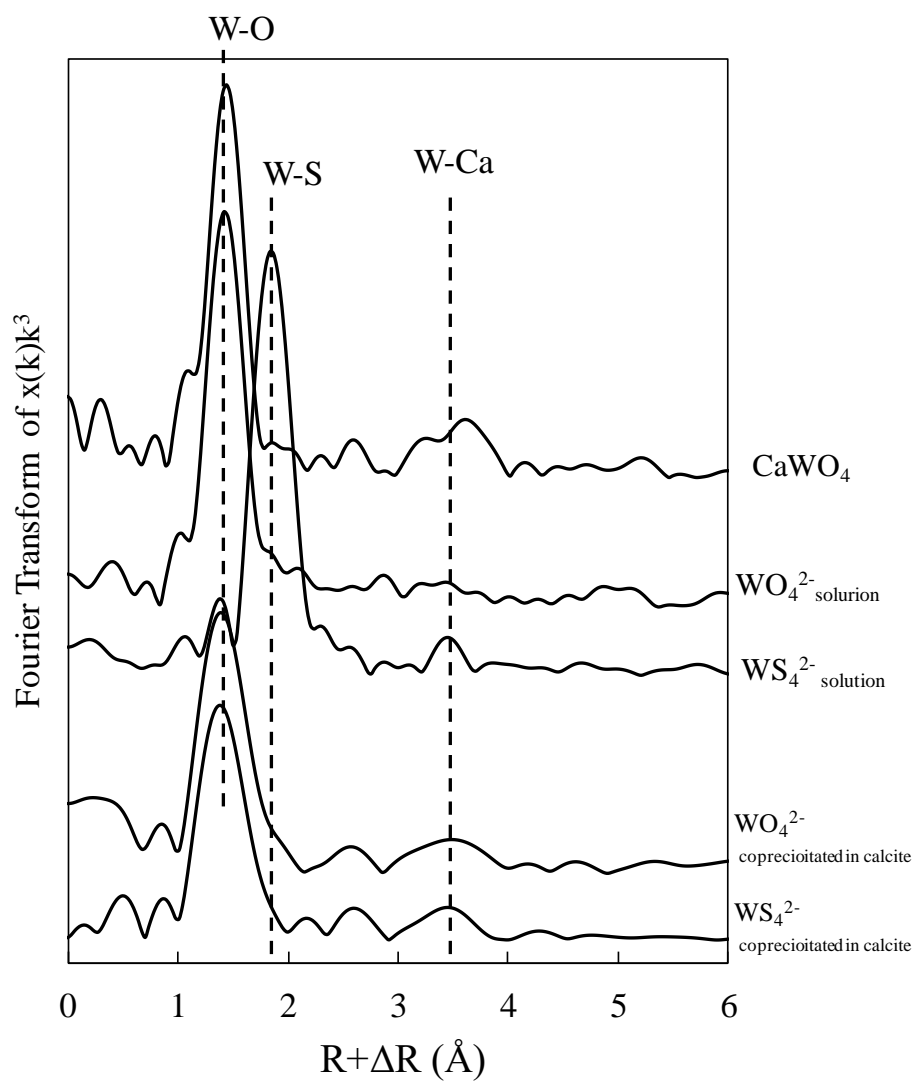
Fig. III-17 Radial structural function (RSF) of tungsten L_3 edge EXAFS coprecipitated in calcite.
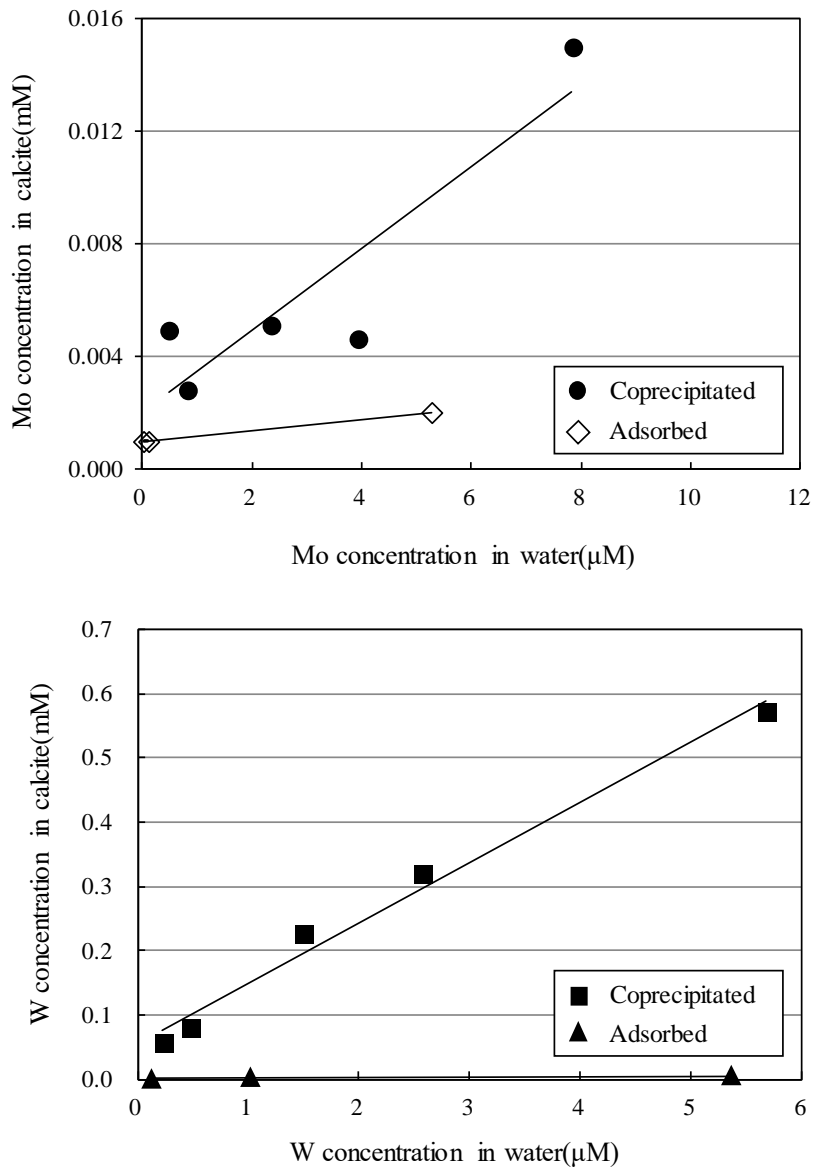
Fig. III-18. Relationship of concentrations of Mo and W coprecipitated into or adsorbed on calcite and their equilibrium concentrations remaining in the aqueous phase.

III.4. Conclusions

In this chapter, I applied WD-μ-XRF-XAFS analysis to determination of the W species in sulfidic sedimentary rocks deposited in Pc/C boundary at the age of ca. 542 Ma. I successfully obtained the micro-scale distribution of trace amount of W in the sample by the combination of WD technique using micro X-ray beam and difference map technique (Fig. III-7g). After the mapping, W L_3 edge XANES spectra were obtained at the area where W was concentrated. Both oxygen and sulfur-coordinated species were found in the sample in which these species seem to have different incorporation processes to the sediments. The sulfur-coordinated species was considered to be formed by the adsorption of WS_4^{2-} species to sulfide minerals, suggesting that the sedimentary environment was under highly sulfidic condition where H_2S concentration would be higher than 100 μM to form WS_4^{2-} in the aqueous phase. On the other hand, oxygen-coordinated species could be formed for W coprecipitated with carbonate even under the reducing condition. These observations were well consistent with the experimental results on the adsorption and coprecipitation of Mo and W to pyrite and calcite. These results implied that incorporation amount of W to sulfidic sediment could be very low compared with Mo.

We also examined Mo distribution and speciation in the same sample to compare the geochemical behaviors of W and Mo. The sample enriched much larger amount of Mo (over 6 wt.%), and Mo formed MoSC phase in the sample due to highly sulfidic condition which accelerated removal of Mo from seawater. Under that condition, W and Mo exhibited different partitions to sulfidic sediment. Subsequently, the difference of partition degrees between W and Mo could affect the concentration of these elements remaining in the seawater. Thus, I estimated the Mo/W ratio in seawater at Pc/C boundary by analyzing the compositions of Mo and W in the carbonate minerals found in the sample. The results showed that W was relatively more

soluble in sulfidic seawater compared with that in oxic seawater.

Our speciation analysis of trace level of W with results from laboratory experiments led to clarification of the geochemical process of W and its difference from Mo in palaeocean. Speciation analysis of W and other trace elements in natural sample in the presence of various elements that can interference with the trace elements can be conducted by XAFS analysis combined with WD technique and micro-XRF-XAFS, which has a great potential to clarify the geochemical behavior of trace elements and to understand the paleo environment based on the speciation information of the trace elements.

Chapter IV. GENERAL DISCUSSION AND CONCLUSIONS

In this Chapter, I first summarize results of this thesis, followed by general discussion and future prospected expected from this thesis.

Summary of this thesis

In this thesis, I obtained following results about geochemical behaviors of Mo and W under sulfidic condition.

In Chapter II, chemical composition and speciation analyses of sediment core and porewater samples collected near the hydrothermal vent in Okinawa Trough showed that redox condition becomes more reducing and sulfidic at deeper depth. In the core samples, we could find the different partition behaviors of Mo and W by XAFS analysis and their adsorption experiments to the sediments.

The speciation analysis showed that adsorbed species of Mo changed depending on the redox condition in the sediments. Under oxic condition in the upper layer, Mo existed as MoO_4^{2-} in porewater and adsorbed as oxygen-coordinated species, while in deeper layer where H_2S was generated in porewater, Mo formed MoS_4^{2-} and the partition to the sediment was larger compared with that in the upper layer. This is the first study observing change of Mo species in the progress of reducing condition by direct speciation method (i.e., XAFS), which was correlated with the increase of its distribution to the sediment.

Although the K_d and chemical species of Mo in the system could be measured by natural sample observation, K_d of W in the system was evaluated by adsorption experiments to the natural sediments in laboratory, which suggested that W formed WO_4^{2-} at all the depths and the

partition of W did not change. The difference of partition of W from Mo showed that the solubility of Mo is much lower than that of W under anoxic and low sulfidic condition, which is the opposite to the case under oxic condition where W is much more strongly fixed to iron and manganese (hydr)oxides relative to Mo.

I also performed μ-XRF-XAFS analysis for highly sulfidic Early Cambrian black shale to examine the natural partition behaviors of Mo and W in Chapter III. For the XAFS analysis of W, BCLA was introduced to decrease the interference X-rays from Ni and Zn which are abundant in the sample. By the WD method, we could confirm the micro scale distribution of W in euxinic sediment and also measure the XANES spectra of W. Under the highly sulfidic condition, W partition to sediment would be very low. Actually, several phases containing W were found in the black shale by the WD-μ-XRF-XAFS analysis. The observed sulfur-coordinated species of W in the sulfide phase indicated that W was dissolved as WS_4^{2-} in the palaeocean when the black shale was deposited, which suggests that high concentration of H_2S was generated in that palaeocean. In the same sample, I found oxygen-coordinated species coprecipitated into carbonate minerals. The ligand exchange reaction of WS_4^{2-} to oxygen-coordinated species was observed experimentally in the coprecipitation experiment of calcite in the presence of WS_4^{2-} in the aqueous phase. The presence of carbonate minerals gives a possibility to estimate the dissolved concentrations of W and Mo at the time of the deposition. In this study, I measured the XRF signal intensity of Mo and W in the carbonate phase to estimate the Mo/W ratio in the palaeocean. The results showed that the Mo/W ratio in sulfidic palaeocean was about 1, which was very different from the molar ratio of Mo/W in modern oxic seawater (=1800). This estimation supports the contrasting partition behaviors of Mo and

W under sulfidic condition: Mo should be strongly removed from sulfidic seawater, while W would not adsorb to sediments greatly compared with Mo.

These speciation and quantitative analyses of two types of sediment samples prove the systematic dependence of water solubilities of Mo and W on the redox, or euxinic condition.

General discussion

In Figs. IV-1 and IV-2, I summarize changes of partition behaviors of Mo and W with the development of redox condition and increase of H_2S concentration in seawater. As previously reported, partition of W to the solid phase such as ferromanganese oxide is larger than that of Mo, because of the difference of their adsorption structures at the oxide-seawater interface under oxic conditions (Kashiwabara et al., 2011; 2013). This result is consistent with previous quantitative analyses Mo and W both in seawater and hydrothermal water (Sohrin et al., 1987; 1999; Kishida et al., 2004). Under sulfidic condition, the apparent partition of W to the solid phase is comparable with that under oxic condition, whereas the sulfidation of Mo enhances the partition of Mo to the solid phase. These results indicate that the concentration of Mo and W in anoxic (euxinic) seawater were different from those in oxic seawater. The simultaneous investigation of the geochemical behaviors of Mo and W in this study contributes to the better understanding of their water solubilities under various redox conditions.

Many studies about removal mechanism of Mo from seawater under sulfidic condition were already reported, but the detailed removal process is not well understood (Chappaz et al., 2014). In the case of W, the studies about environmental behavior of W and formation of WS_4^{2-} are very few due to the lower abundance of W in natural samples leading to the difficulty of quantitative and speciation analyses.

My approach with molecular scale investigation of Mo and W to clarify their partitions to sediments under sulfidic condition could lead to more accurate understanding of the processes. In particular, speciation results of W in natural samples cannot be obtained without using the high sensitive XAFS analysis developed in this study.

The samples studied in Chapter II contained 0.49 and 0.37 mg/kg of W. In the same sample, 7070 and 3660 mg/kg of Zn were contained, respectively. The concentration of Zn was larger than W by more than 10,000 times (by weight) in each sample. These W/Zn ratios are very low compared with previous studies reporting XAFS data for the speciation. In Kashiwabara et al. (2010) employing WD-XAFS for W in ferromanganese nodules, W and Zn abundances were 49.1 mg/kg and 1420 mg/kg, respectively, which yields the W/Zn ratio around 0.035, which is more than 350 times higher than the case of the sulfidic sediments examined in this study. This fact reveals that XAFS analysis of W in the sulfidic sediment is far more difficult.

In this thesis, however, good quality XANES spectra of W to determine the chemical species of W in each sample were successfully obtained, in spite of the very low W/Zn ratio compared with previous studies. The very high sensitivity of the WD-XAFS technique was achieved by the use of focused beam which increased photon flux per unit area. Furthermore, as shown in chapter III, WD-μ-XRF-XAFS technique enabled to measure high spatial resolution mapping and speciation of W in the hot spot of W in natural sample, though the W/Zn ratio is very low as bulk composition. High spatial resolution analysis allowed us to avoid the analyzing point where W signal is low relative to Zn (and Ni) signals. These analytical approach for speciation of trace elements in natural samples will lead to better understanding of geochemical process of trace elements in the environment. In particular, energy range from 4.0 to 11.0 keV includes important Kα and Kβ lines of transition metals that are often involved in natural samples over

100 mg/kg level. Thus, WD-XAFS technique can clarify chemical species of trace metals such as REEs and PGEs that are involved in samples below 10 mg/kg by measuring their L edge XAFS spectra which are subject to serious interferences by Kα and Kβ lines of other transition elements.

Further understanding of geochemical behavior of trace elements can give new insights into evolution of the earth's environment. Concentrations or isotopic compositions of redox sensitive trace elements such as Mo have been investigated as a signature of oxygenation of the environment, which leads to better understanding of chemical composition and their bioavailability in ancient ocean related to the evolution of lives (Anbar, 2008; Scott et al., 2008; Wille et al., 2008). My speciation data of Mo and W combined with partition in sediment-water system can add new information about physico-chemical mechanisms of removal of Mo and W from seawater under sulfidic condition. The physico-chemical mechanisms in turn control chemical and isotopic compositions of elements in ocean (Kashiwabara et al., 2011).

In addition, I examined the difference of partition behaviors of Mo and W under various sulfidic condition in this thesis. For example, chemical species of Mo was changed depending on the redox condition and H_2S concentration. On the other hand, W species did not change within the sediment core sample in Okinawa Trough irrespectively of variation of redox condition and H_2S concentration in the pore water. There results suggest that the understanding of difference of geochemical behaviors of Mo and W can give some constrains on the estimation of the redox condition in natural environment.

Future prospects

Although our speciation data showed the difference of partition behavior of Mo to W, local structure of Mo and W adsorbed on pyrite surface is still unclear. Previous studies suggested that Mo is adsorbed as inner-sphere complex by the formation of Fe-Mo-S cubane structure on the sulfide surface (Bostick et al., 2003). However, in my analyses, I could not observe the cubane structure. It is important to obtain XANES and EXAFS spectra of pure Fe-Mo-S phase as a reference material to confirm the adsorbed structure of Mo on sediments. In addition, the present analysis for W experimentally adsorbed on pyrite implied that W also forms inner-sphere complex on the pyrite surface, indicating that the difference of geochemical behaviors of Mo and W under sulfidic condition is not caused by the difference of their adsorption structures. It is possible that the difference is originated from the preference of their coordinations to S or O as their chemical properties. Further molecular scale investigation such as using quantum chemical calculation is needed to understand their affinities for S or O.

On the other hand, carbonate mineral such as calcite has a potential to clarify the concentration of Mo and W under various redox conditions and H_2S concentrations. Further fundamental study about incorporation process of Mo and W to calcite is very important to estimate compositions of Mo, W and other trace elements in paleocean under various redox conditions.
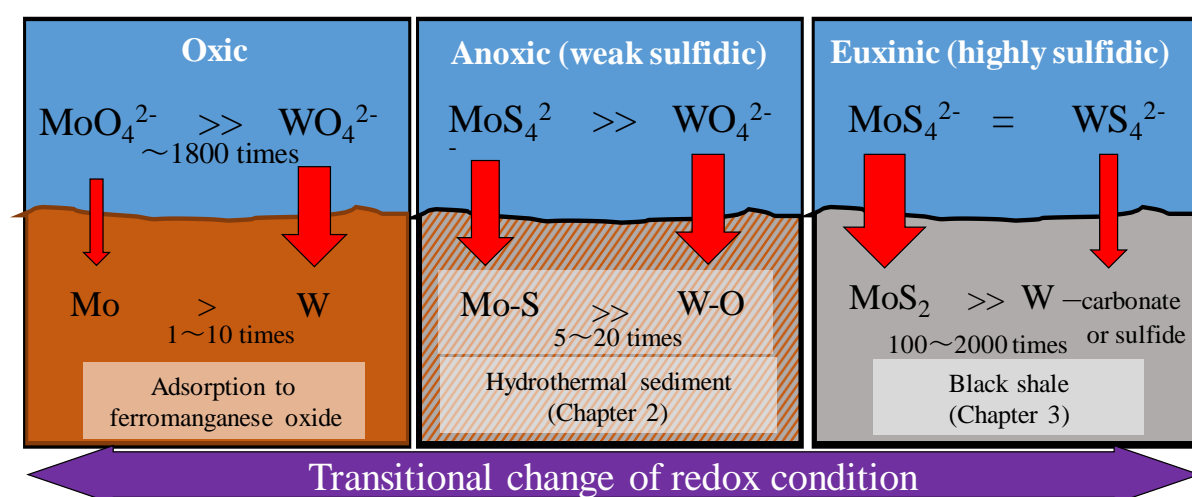
Fig. IV-1 Overview of partition behaviors of Mo and W through the change of redox condition
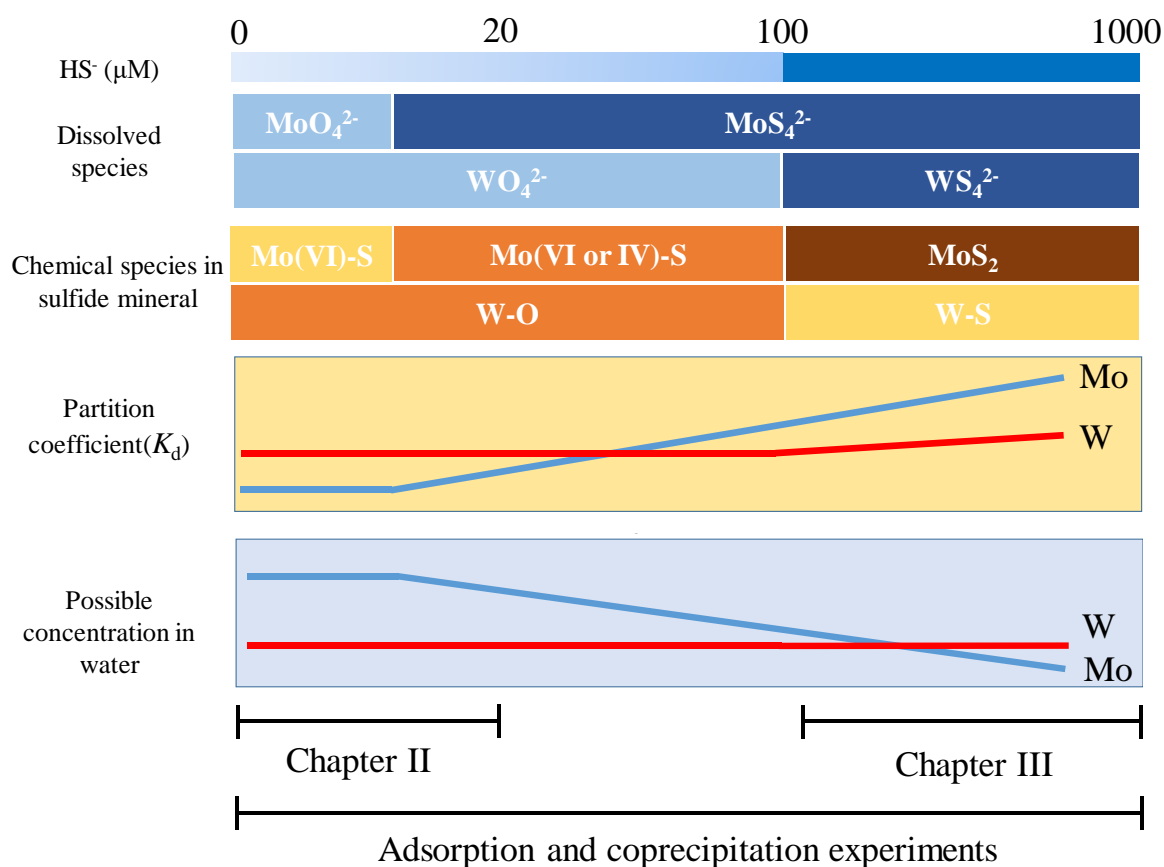

Fig. IV-2 Summary of the change of geochemical behaviors of Mo and W under various sulfidic conditions.

ACKNOWLEDGMENTS

REFERENCES

Anbar, A. D. 2008. Elements and evolution. Science 322, 1481-1483.

Adelson, J. M., Helz, G. R., Miller, C. V. 2001. Reconstructing the rise of recent coastal anoxia; molybdenum in Chesapeake Bay sediments. Geochim. Cosmochim. Acta 65, 237-252.

Abraitis, P. K. Pattrick, R. A. D. Kelsall, G. H., 2004. Acid leaching and dissolution of major sulphide ore minerals: processes and galvanic effects in complex systems. Mineralogical Magazine 68, 343-351

Beauchemin, S., Hesterberg, D., Beauchemin, M. 2002. Principal component analysis approach for modeling sulfur K-XANES spectra of humic acids. Soil Sci. Soc. 66, 83-91

Bertine K. K. and Turekian K. K. 1973. Molybdenum in marine deposits. Geochim. Cosmochim. Acta 37, 1415-1434.

Bostick, C., Fendorf, S., Helz, G. R., 2003. Differential adsorption of molybdate and tetrathiomolybdate on pyrite (FeS_2). Environ. Sci. Tech. 37, 285-291.

Brookins, D. G. 1987. Eh-pH diagrams for geochemistry. Springer-Verlag 16-17.

Brucker, R. L. P., McManus, J., Severmann, S., Berelson, W. M., 2009. Molybdenum behavior during early diagenesis: Insights from Mo isotopes. Geochem. Geophys. Geosyst. 10, Q06010.

Brumsack H. J. and Gieskes J. M. 1983. Interstitial water tracemetal chemistrv of laminated sediments from the Gulf of California, Mexico. Mar. Chem. 14, 89-106.

Chappaz, A., Lyons, T. W., Gregory, D. D., Reinhard, C. T., Gill, B. C., Li, C., Large, R. R. 2014. Does pyrite act as an important host for molybdenum in modern and ancient euxinic sediments? Geochim. Cosmochim. Acta 126, 112-122.

Christou, G., Garner, C. D., Mabbs, F. E., Manchester, M., King, J. 1978. Crystal Structure of Tris(tetra-n-butylammonium) Tri-p-benzenethiolato-bis{tri-p-sulphido-[p,-sulphido -tris(benzenethiolatoiron)] molybdenum} [Bun4N],[{(PhSFe),MoS4},(SPh),]; an Fe$_3$MoS$_4$ Cubic Cluster Dimer. J. Chem. Soc. Chem. Comm., 740-741.

Cline, J. 1969. Spectrophotometric determination of hydrogen sulfide in natural waters. Limnology and Oceanography, 454-458.

Condie, K. C. 1993. Chemical composition and evolution of the upper continental crust: Contrasting results from surface samples and shales. Chem. Geol. 104, 1-37.

Cramer, S. T., Liang, K. S., Jacobson, A. J., Chang, C. H., Chianelli, R. R., 1984. EXAFS studies of amorphous molybdenum and tungsten trisulfides and triselenides. Inorg.Chem. 23, 1215-1221.

Dahl, T. W., Chappaz, A., Fitts, J. P., Lyons, T. W. 2013. Molybdenum reduction in a sulfidic lake: Evidence from X-ray absorption fine-structure spectroscopy and implications for the Mo paleoproxy. Geochim. Cosmochim. Acta 103, 213-231.

Donald, W. M., Leonard V. I., and Mansuktto K. 1995. Metathetical Precursor Route to Molybdenum Disulfide. Inorganic Syntheses. 30, 33–37.

Drever, J. I. 1997. The Geochemistry of Natural Waters: Surface and Groundwater Environments (3rd Edition). Prentice Hall pp436.

Erickson, B. E., Helz, G. R. 2000. Molybdenum (VI) speciation in sulfidic waters : Stability and lability of thiomolybdates. Geochim. Cosmochim. Acta 64, 1149-1158.

Gamo, T., Sakai, H., Kim, E. S., Shitashima, K., Ishibashi, J. 1991. High alkalinity due to sulfate reduction in the CLAM hydrothermal field, Okinawa Trough. Earth and Planetary Science Letters 107, 328-338.

Helz, G. R., Bura-Nakić, E., Mikac, N., Ciglenečki I. 2011. New model for molybdenum behavior in euxinic waters. Chem. Geol. 284, 323–332.

Helz, G. R., Miller, C. V., Charnock, J. M., Mosselmans, J. F. W., Pattrick, R. A. D., Garner, C. D., Vaughan, D. J. 1996. Mechanism of molybdenum removal from the sea and its concentration in black shales: EXAFS evidence. Geochim. Cosmochim. Acta 60, 3631-3642.

Holland, H. D. 2006. The oxygenation of the atmosphere and oceans. Phil. Trans. Roy. Soc. B. 361, 903-915.

Holm, R. H., Solomon, E. I., Majumdar, A., Tenderholt, A. 2011. Comparative molecular chemistry of molybdenum and tungsten and its relation to hydroxylase and oxotransferase enzymes. Coord. Chem. Rev. 255, 993-1015.

Kamitsubo, H., 2007. Historical overview of the synchrotron radiation research in Japan ― from the view point of creative works in the development of light sources and related technology― . The Jpn. Soc. Synchrotron Radiation Research 20, 3-17.

Kao, L.S., Peacor, D.R., Coveney, R.M., Zhao, G.M., Dungey, K.E., Curtis, M.D., Penner-Hahn,J.E. 2001. A C/MoS2 mixed-layer phase (MoSC) occurring inmetalliferous black shales from southern China, and new data on jordisite. Am. Mineral. 86, 852–861.

Kashiwabara, T., Takahashi, Y., Marcus, M., Uruga, T., Tanida, H., Terada, Y., Usui, A. 2013. Tungsten species in natural ferromanganese oxides related to its different behavior from molybdenum in oxic ocean. Geochim. Cosmochim. Acta 106, 364-378.

Kashiwabara, T., Takahashi, Y., Tanimizu, M., Usui, A. 2011. Molecular-scale mechanisms of distribution and isotopic fractionation of molybdenum between seawater and ferromanganese oxides. Geochim. Cosmochim. Acta 75, 5762-5784.

Kashiwabara, T., Takahashi, Y., Uruga, T., Tanida, H., Terada, Y., Niwa, Y., Nomura, M. 2010. Speciation of tungsten in natural ferromanganese oxides using wavelength dispersive XAFS. Chem. Lett. 39, 870-871.

Kawagucci, S., Chiba, H., Ishibashi, J., Yamanaka, T., Toki, T., Muramatsu, Y., Ueno, Y., Makabe, A., Inoue, K., Yshida, N., Nakagawa, S., Nunoura, T., Takai, K., Takahata, N., Sano. Y., Narita, T., Teranishi, G., Obata, H., Gamo, T. 2011, Hydrothermal fluid geochemistry at the Iheya North field in the mid-Okinawa Trough: Implication for origin of methane in subseafloor fluid circulation systems. Geochem. J. 45, 109-124.

Kawano, Y. 2010. Quantitative Analyses of silicate rocks and sediments using X-ray fluorescence spectrometer ZSX Primus II. Bulletin of geo-environmental science 12, 85-97.

Kishida, K., Sohrin, Y., Okamura, K., and Ishibachi, J. 2004. Tungsten enriched in submarine hydrothermal fluids. Earth Planet. Sci. Lett., 222, 819-827.

Kletzin, A., Adams, M. W. W. 1996. Tungsten in biological systems. FEMS Microbiology Reviews 18, 5-63.

Kříbek, B., Sýkorová, I., Pašava, J.,Machovič, V., 2007. Organic geochemistry and petrology of barren and Mo–Ni–PGE mineralized marine black shales of the Lower Cambrian Niutitang Formation (South China). Int. J. Coal Geol. 72, 240–256.

Kropf, A. J., Finch, R. J., Fortner, J. A., Aase, S., Karanfil, C., Segre, C. U., Terry, J., Bunker, G., and Chapman L. D. 2003. Bent silicon crystal in the Laue geometry to resolve x-ray fluorescence for x-ray absorption spectroscopy. Rev. Sci. Instrum. 74, 4696-4702.

Lee, C., Hong, J., Lee, W. R., Kim, D. Y., and Shim, J. H., 2014, Density functional theory investigation of the electronic structure and thermoelectric properties of layered MoS_2, $MoSe_2$ and their mixed-layer compound. J. Solid State Chem. 211, 113–119.

Lehmann, B., Nägler, T.F., Holland, H.D., Wille, M., Mao, J.W., Pan, J.Y., Ma, D.S., Dulski, P., 2007. Highly metalliferous carbonaceous shale and Early Cambrian seawater. Geology 35, 403–406.

Lu, H. Z., Liu, Y. M., Wang, C. L., Xu, Y. Z., Li, H. Q. 2003. Mineralization and fluid inclusion study of the Shizhuyuan W-Sn-Bi-Mo-F skarn deposit, Hunan province, China. Economic Geol. Bull. Soc. Economic Geol. 98, 955-974.

Mao, J., Lehman, B., Du, A., Zhang, G., Ma, D., Wang, Y., Zeng, M., Kerrich R. 2002. Re-Os Dating of Polymetallic Ni-Mo-PGE-Au Mineralization in Lower Cambrian Black Shales of South China and Its Geologic Significance. Eco. Geol. 97, 1051-1061.

Manceau, A., Marcus, M.A., and Tamura, N., 2002. Quantitative speciation of heavy metals in soils and sediments by synchrotron X-ray techniques. Rev. Miner. Geochem. 49, 341–428.

Miyoshi, Y., Ishibashi, J., Shimada, K., Shimada, O., Uehara, S., Yoshizumi, R., Watanabe, S., Urabe, T. 2015. Occurrence of hydrothermal alteration minerals at the Jade hydrothermal field, in the Izena hole, Mid-Okinawa trough. Subseafloor Biosphere Linked to Hydrothermal Systems: TAIGA Concept 567-583.

Mohajerin, T. J., Helz, G. R., Johannesson, K. H. 2016. Tungsten-molybdenum fractionation in estuarine environments. Geochim. Cosmochim. Acta 177, 105-119.

Mohajerin, T. J., Helz, G. R., White, C. D., Johannesson, K. H. 2014. Tungsten speciation in sulfidic waters: Determination of thiotungstate formation constants and modeling their distribution in natural waters. Geochim. Cosmochim. Acta 144, 157-172.

Mukund, S., Adams, M W. W. 1991. The Novel Tungsten-Iron-Sulfur Protein of the Hyperthermophilic Archaebacterium, Pyrococcus furiosus, Is an Aldehyde Ferredoxin Oxidoreductase. J. Bio. Chem. 266, 14208-14216.

Nakaseama, M., Ishibashi, J., Ogawa, K., Hamasaki, H., Fujino, K., Yamanaka, T. 2008. Fluid –sediment interaction in a marine shallow-water hydrothermal system in the Wakamiko Submarine Crater, South Kyushu, Japan. Resource Geol. 58, 289-300.

Ohta, T. 2016. Retrospect and Prospect of the XAFS Spectroscopy. J. Vac. Soc. Jpn. 59, 319-326.

Pasava, J., Svojtka, M., Veselovský, F., Ďurišová, J., Ackerman, L., Pour, O., Drábek, M., Halodová, P., Haluzová, E. 2016. Laser ablation ICPMS study of trace element chemistry in molybdenite coupled with scanning electron microscopy (SEM) - An important tool for identification of different types of mineralization. 72, 874-895.

Pilipchuk M. F. and Volkov I. I. 1974. Behavior of molybdenum in processes of sediment formation and diagenesis in Black Sea. In The Black Sea: Geology, Chemistry and Biology AAPG Mem. 20, pp. 542-553

Ressler, T., Wienold, J., Jentoft, R. E., 2001. Formation of bronzes during temperature-programmed reduction of MoO_3 with hydrogen—an in situ XRD and XAFS study. Solid State Ionics 141–142, 243–251.

Rosing, M. T. 1999. C-13-depleted carbon microparticles in > 3700-Ma sea-floor sedimentary rocks from west Greenland. Science 283, 674-676.

Rudnick, R. L. and Gao, S. 2004. Composition of the Continental Crust. In: Treatise on Geochemistry. Holland, H.D. and Turekian, K.K. (Editors), Elsevier, Amsterdam 3, 1-64.

Ryzhenko, B. N. 2010. Technology of groundwater quality prediction: 1. Eh–pH diagram and detention coefficient of molybdenum and tungsten in aqueous solutions. Geochemistry International 48, 407–414.

Saito, M., Sigman, D. M., Morel, F. M. M. 2003. The bioinorganic chemistry of the ancient ocean: the co-evolution of cyanobacterial metal requirements and biogeochemical cycles at the Archean–Proterozoic boundary? Inorgan. Chim. Acta 356, 308-318.

Schopf, J. W. 1993. Microfossils of the Early Archean Apex chert: new evidence of the antiquity of life. Science 260, 640-646.

Scott, C., Lyons, T. W., Bekker, A., Shen, Y., Poulton, S. W., Chu, X., and Anbar. A. D. 2008. Tracing the stepwise oxygenation of the Proterozoic ocean. Nature. 452, 456-459.

Schroeder, S. L. M. 1996. Towards a 'Universal Curve' for total electron-yield XAS. Solid State Comm. 98, 405-409.

Selby, D., Nesbitt, B. E., Muehlenbachs, K., Prochaska, W. 2000. Hydrothermal alteration and fluid chemistry of the Endako porphyry molybdenum deposit, British Columbia. Economic Geology 95, 183-201.

Shirakami, H., 1993. A handbook of Quaternary research, vol.2. The Univ. of Tokyo press 119-124.

Sohrin, Y., Fujishima, Y., Ueda, K., Akiyama, S., Mori, K., Hasegawa, H., Matsui, M. 1998. Dissolved niobium and tantalum in the North Pacific. Geophysical Research Letters 25, 999-1002.

Sohrin, Y., Isshiki, K., Kuwamoto, T., Nakayama, E., 1987. Tungsten in north Pacific waters. Marine Chemistry 22, 95-103.

Solórzano, L. 1968. Determination of ammonia in natural water by the phenol hypochlorite method. Limol Oceanogr 14, 799-801.

Takahashi, S., Yamasaki, S., Ogawa, Y., Kimura, K., Kaiho, K., Yoshida, T., Tsuchiya, N. 2014. Bioessential element-depleted ocean following the euxinic maximum of the end-Permian mass extinction. Earth and Planetary Science Letters 393, 94-104.

Takahashi, Y., Uruga, T., Tanida, H., Terada, Y., Shimizu, H. 2006. Application of X-ray absorption near-edge structure (XANES) using bent crystal analyzer to speciation of trace Os in iron meteorites. Anal. Chim. Acta 558, 332-336.

Takahashi, Y., Miyoshi, T., Higashi, M., Kamioka, H., Kanai, Y., 2009. Neutralization of calcite in mineral aerosols by acidic sulfur species collected in China and Japan studied by Ca K-edge X-ray absorption near-edge structure. Environ. Sci. Technol. 43, 6535-6540.

Tanaka K., and Kawabe I. 2006. REE abundance in ancient seawater inferred from marine limestone and experimental REE partition coefficients between calcite and aqueous solution. Geochem. J. 40, 425-435

Tanaka K., Takahashi., Y. and Shimizu H. 2008. Local structure of Y and Ho in calcite and its relevance to T fractionation from Ho in partitioning between calcite and aqueous solution. Chem. Geol. 248, 104-113.

Terada, Y., Homma, T. S., Takeuchi, A., Suzuki, Y. 2010. High-energy X-ray microprobe system with submicron resolution for X-ray fluorescence analysis of uranium in biological specimens. X-Ray Optics and Instrumentation 2010, 1-5.

Turner, D. R., Whitfield, M., Dickson, A. G. 1981. The equilibrium speciation of dissolved components in freshwater and sea water at 25°C and 1 atm pressure. Geochim. Cosmochim. Acta 45, 855-881.

Turner, D.R. Problems in trace metal speciation modeling. In: D.R. Turner and A. Tessier, (editors), Metal Speciation and Bioavailability in Aquatic Systems, John Wiley and Sons, New York, pp. 1995, 150-203.

Wilkin, R. T., Barnes, H. L. 1996. Pyrite formation by reactions of iron monosulfides with dissolved inorganic and organic sulfur species. Geochim. Cosmochim. Acta 60, 4167-4179.

Wilkin, R. T., Barnes, H. L., Brantley, S. L. 1996. The size distribution of framboidal pyrite in modern sediments: An indicator of redox conditions. Geochim. Cosmochim. Acta 60, 3897-3912.

Wille, M., Na¨gler, T. F., Lehmann B., Schro¨der, S., Kramers, J. D. 2008. Hydrogen sulphide release to surface waters at the Precambrian/Cambrian boundary. Nature 453, 767-769.

Williams, R. J. P., Da Silva, J. J. R. F. 2003. Evolution was Chemically Constrained. Journal of Theoretical Biology 220, 323-343.

Xu, L., Lehman, B., and Mao, J. 2013. Seawater contribution to polymetallic Ni–Mo–PGE–Au mineralization in Early Cambrian black shales of South China: Evidence from Mo isotope, PGE, trace element, and REE geochemistry. Ore Geol. Rev. 52, 66–84.

Yamamoto, Y., Takahashi, Y., Kanai, Y., Watanabe, Y., Uruga, T., Tanida, H., Terada, Y., and Shimizu, H. 2008. High-sensitive measurement of uranium LIII-edge X-ray absorption near-edge structure (XANES) for the determination of the oxidation states of uranium in crustal materials Appl. Geochem. 23, 2452-2461.

Yokoyama, Y., Takahashi, Y., Miyoshi, Y., Ishibasshi, J., Kawagucci, S. 2015. Sediment–porewater system associated with native sulfur formation at Jade hydrothermal field in Okinawa trough. Subseafloor Biosphere Linked to Hydrothermal Systems: TAIGA Concept 405-419.

Yoshizumi, R., Miyoshi, Y., Ishibashi, J. 2015. The characteristics of the seafloor massive sulfide deposits at the Hakurei site in the Izena hole, the Middle Okinawa trough. Subseafloor Biosphere Linked to Hydrothermal Systems: TAIGA Concept 561-565.

Zabinsky S. I., Rehr J. J., Ankudinov A., Albers R. C. and Eller M. J., 1995. Multiple-scattering calculations of X-ray-absorption spectra. Phys. Rev. B 52, 2995–3009.

Zerkle, A. L., House, C. H., Brantley, S. L. 2005. Biogeochemical signatures through time as inferred from whole microbial genomes. American J. Sci. 305, 467-502.